1990

Study of O/Ni(100) with LEED and AES: from chemisorption to oxidation

Wen-Di Wang
Iowa State University

Order Number 9110581

Study of O/Ni(100) with LEED and AES: From chemisorption to oxidation

Wang, Wen-Di, Ph.D.

Iowa State University, 1990

U·M·I
300 N. Zeeb Rd.
Ann Arbor, MI 48106

Study of O/Ni(100) with LEED and AES: From chemisorption to oxidation

by

Wen-Di Wang

A Dissertation Submitted to the
Graduate Faculty in Partial Fulfillment of the
Requirements for the Degree of
DOCTOR OF PHILOSOPHY

Department: Chemistry
Major: Physical Chemistry

Approved:

Signature was redacted for privacy.

In Charge of Major Work

Signature was redacted for privacy.

For the Major Department

Signature was redacted for privacy.

For the Graduate College

Iowa State University
Ames, Iowa
1990

TABLE OF CONTENTS

DEDICATION

To my parents,

Yun-Fang Lan and Zheng-Bian Wang

GENERAL INTRODUCTION

Importance of Studies of Metal Oxidation

The interaction of gases with solid surfaces has been a subject of a wide range of studies. If the solid has single crystal structure and terminates at the surface with long-range, 2-dimensional periodicity, the interaction between adsorbate and substrate can result in ordered adlayer and/or sublayer structures, which can be studied with the fast developing techniques of surface science. This dissertation is aimed at studying the conditions necessary for formation of the ordered surface and subsurface structures when the surface is exposed to gas particles. The system oxygen/Ni(100) is chosen for the investigation of the formation and change of surface and subsurface structures when oxygen exposure and substrate temperature are varied, or when adsorbed surfaces are annealed to higher temperatures. Two well-known surface science techniques, AES (Auger electron spectroscopy) and LEED (low-energy electron diffraction), are employed in this study. AES is used to check the surface cleanliness before each measurement, to correlate the oxidation onset with the observations from LEED, and to help identify differences between the electronic states and binding energies of different oxide epitaxies. LEED is used to quantitatively monitor changes in ordered structures, during adsorption and annealing, by following the changes in the integrated spot intensities or spot profiles.

Metal oxidation is a reaction between a solid and a gas. It involves the combination of oxygen with metals, and it has the greatest commercial impact in the presence of moisture, as in corrosion. The importance in studying the metal oxidation has been realized for a long time. For example, Cabrera and Mott have studied the formation of oxide films in the surface region on many metals, including Ni, in 1949 [1]. The metal nickel is often used as an electroplate or as a component in alloys to improve the corrosion resistance of other metals. Nickel is also widely used in catalysis, mainly in hydrogenation reactions. Its catalytic property can be influenced by the presence of oxygen. Some poisoning [2] or promoting [3] effects in catalytic reactions have been observed when O_2 traces are present in the gaseous reaction mixture. Moreover, recent results have shown that the presence of partially oxidized metallic phases modifies the adsorptive properties of nickel catalysts [4,5]. Nickel oxide is also an important component of a number of oxidation catalysts [6]. Consequently, studies of the nickel-oxygen system may give useful information. In order to gain a detailed atomic- and molecular-scale knowledge of the phenomenon, it is obviously desirable to carry out experiments on well-defined nickel surfaces (single crystals).

Previous Studies of O/Ni(100)

Surface studies of the adsorption of oxygen on the nickel surface can be traced back to the time of the historical discovery of electron

diffraction by Davisson and Germer in 1925 [7]. That accidental exposure of O_2 to Ni surface established the theoretical base for the future invention of modern LEED technique, although it did not lay much ground for the study of nickel oxidation. The modern surface studies of O/Ni(100) system started at about the same time as surface science started to quickly develop. It is one of the most thoroughly studied systems in surface science. As a result, many facts are reasonably well-established. The first of O/Ni(100) was done by MacRae [8], who studied all three low-index faces -(100), (111) and (110)- with LEED. In that work he identified the chemisorption structures of O/Ni(100), denoted p(2x2)-O and c(2x2)-O. The two structures have ideal coverages of 0.25 and 0.50 monolayers, respectively. (One monolayer, $\theta = 1$, is here defined as one adsorbed particle per metal atom in the Ni(100) surface.) It is generally agreed now that in each structure, oxygen atoms reside in or near the four-fold hollow sites, and the oxygen-surface distance is 0.8 to 0.9 Å [9-18], although the most recent work by Chubb et al. reduces this value to 0.75 Å with a full-potential, spin-polarized, total-energy calculation on the Ni(100)-c(2x2)-O system [19]. The formation of p(2x2) structure is accompanied by a +2% expansion between the top two Ni layers, and the c(2x2) is accompanied by a larger relaxation of +5% [10,11], which has been increased to +5.7% by the most recent study [19]. (These relaxations are quoted as percentages of the spacing between (100) and (200) planes in bulk Ni.) The phase diagram of the chemisorption structures, p(2x2) and c(2x2), has been partially mapped out by Taylor and Park [20]. The adsorption kinetics are very temperature-dependent, and

can not be reconciled with a simple second-order Langmuir isotherm [9,21, 22]. Brundle and coworkers have suggested that the kinetics at room temperature are dominated by an adsorption-site-ensemble requirement, and the kinetics at low temperatures (ca. 150 K or below) are dominated by a mobile (molecular) precursor [9,21,22].

Nickel oxidizes quite readily, and so exposure to oxygen eventually causes oxidation of the near-surface region. The classic study of this phenomenon is that by Holloway and Hudson. They studied the oxide structures that form at coverages beyond that of the c(2x2), using LEED, AES and work function measurements [23]. Since that report, many others have contributed to the pool of available information.
As far as the thickness of the nickel oxide is concerned, there is usually agreement that the oxide which forms between 80 and 400 K is two or three layers deep, whereas the oxide is deeper when formed at or above about 500 K [9,23-27]. However, report of other depth also exists, Evans et al. reported that a 18 Å deep (about 9 ML) oxide layer forms at 300- 370 K [28]. The onset of oxidation occurs at a coverage reported by most authors as 0.35 to 0.45 monolayers [9,23-26,29], i.e., well before the ideal coverage of the c(2x2) layer, 0.50 monolayers, is reached. The onset of oxidation usually follows a plateau in the coverage-exposure relationship (effectively, an induction period), whose length varies directly with temperature [9,23-26,29].

The oxide which forms is generally thought to be NiO, although there are also reports of Ni_2O_3 [28,30] and Ni_3O [31], which have not been discussed seriously in the literature. However, the epitaxial

orientation of NiO on Ni(100) has been a topic of disagreement. Wagner and Moylan observed only NiO(100) [32]. On the other hand, Holloway and Hudson in their classic study [23], as well as Mitchell et al. [24], reported that the (100) and (111) orientations develop together. Later studies confirmed the existence of these two epitaxies of NiO on Ni(100) [26,27,33]. One common feature of almost all these studies is that the structures are obtained by oxidation at room temperature [23,24,32,33], although there have been some work also at higher temperatures [23,34]. The problem of these studies, at one temperature or a narrow range, is that they did not see the whole picture of this system.

Some authors have also tried to draw a mechanism about this process, from chemisorption to oxidation [10,23]. It was suggested that the process is divided into three stages: chemisorption, slow induction (presumably nucleation) period and fast oxidation (lateral growth of nucleation sites until they coalesce and form a saturated, homogeneous nickel oxide layer). However, this mechanism is only phenomenological. It did not give any insight of the energetic factors that govern the competition and formation of different oxide structures during the oxidation stage.

Finally, quite recently, there has been a report of a (7x7) structure, interpreted as a strained form of NiO(100) [33].

Overview of Thesis Work

In the first chapter, the temperature- and exposure-dependence of surface structures which form prior to, and during, oxidation of Ni(100) is described. As in many other studies, Auger electron spectroscopy is used as a measure of relative coverage, and as an independent measure of the point at which oxidation begins during adsorption. In the second chapter, discussions on the (7x7) structure are further extended. More data on the peculiar behavior of the (7x7) are presented. Three possible models are discussed in order to find one that could explain as much experimental observation as possible. In Chapter 3, results from AES measurements are presented. In the AES measurements, surfaces with different adsorbed structures or different annealing histories are compared to elucidate that the similarities and differences visible with AES might reflect the similarities and differences in the structures of the three oxide structures. In Chapter 4, Debye-Waller factors are measured on NiO(111) and NiO(100). The surface Debye temperature of NiO is presented. The linearity of the Debye-Waller effect is found to hold down to temperatures 1/2 the surface Debye temperature. This supports the suggestion that the condition for the Debye-Waller relation to be true can be relaxed [35]. In Chapter 5, some brief results about the pressure effect are presented. They suggest that the oxide epitaxy on Ni(100) has no dependency on the oxygen pressure in the range 10^{-9} to 10^{-7} torr.

This dissertation has accomplished the study on O/Ni(100) in the

following aspects. First, we quantitatively measure diffraction spot intensities and profiles during adsorption and annealing. This reveals whether and how changes in surface structures are correlated. The approach is similar to the recent study of oxygen on Pd(100) conducted in the same laboratory [36,37]. [Previous investigators have used qualitative, visual examination of LEED or RHEED patterns to draw such conclusions for O/Ni(100) [e.g., 16, 17]. This work shows that such an approach can be misleading.] Second, adsorption is carried out at temperatures of 80 to 400 K. The majority of previous work has concentrated on temperatures of 300 and 400 K. Studying the entire range from 80 to 400 K allows us to make definitive statements about the effect of temperature on the surface orientation of the oxide, and on the conditions under which this oxide forms. This leads us to suggest two reasons why the published literature contains disagreement over oxide orientation. Third, a new oxide, (7x7), that has been overlooked for many years, is observed and studied to the great extent. Effort has been put in interpretting the real space structure of this pattern. Fourth, Debye-Waller factor, and therefore surface Debye temperatures are estimated for NiO in this dissertation. Fifth, the pressure effect on the growth of oxide epitaxy is studied. The results do not support the belief that the epitaxy of oxide growing on Ni(100) has dependency on the pressure of oxygen. Finally, this study lends significant new insight into energetic factors which influence oxide epitaxy on Ni surfaces.

CHAPTER 1: STRUCTURAL STEPS TO OXIDATION OF Ni(100)

Equipment and Experimental Procedures

The experimental apparatus consists of a stainless-steel, ultrahigh-vacuum chamber with a commercial, single-pass, cylindrical mirror analyzer (CMA) and coaxial electron gun, optics for low-energy electron diffraction, an ion bombardment gun, and a mass spectrometer, refer to Figure 1. A high resolution (Silicon Intensified Target) video camera is interfaced with a PDP-11 PC to quantitatively record the digitized LEED image. This video-LEED system can give information of integrated spot intensities and spot profiles during a continuous adsorption or annealing process. Figure 2 schematically shows how the data are obtained. Detailed description can be found elsewhere [38]. This conventional LEED is believed to have a transfer width of about 160 Å [39]. The pressure in the chamber is 7×10^{-11} Torr or less prior to each experiment. The oxygen used for adsorption is 99.998% purity contained in glass bowl. The 99.6% purity extra dry oxygen in lecture bottle is used for rough cleaning of the surface between experiments. The sample is mounted on a manipulator which can provide motion in x, y, z direction and rotation of 360°. Detailed description can be found elsewhere [40]. Temperature is controlled through a feedback circuit designed by Herz et al. [41]. Intensities and profiles of diffraction features, measured in this work, are all corrected for background as described in Chapter 2 and Ref. 38.

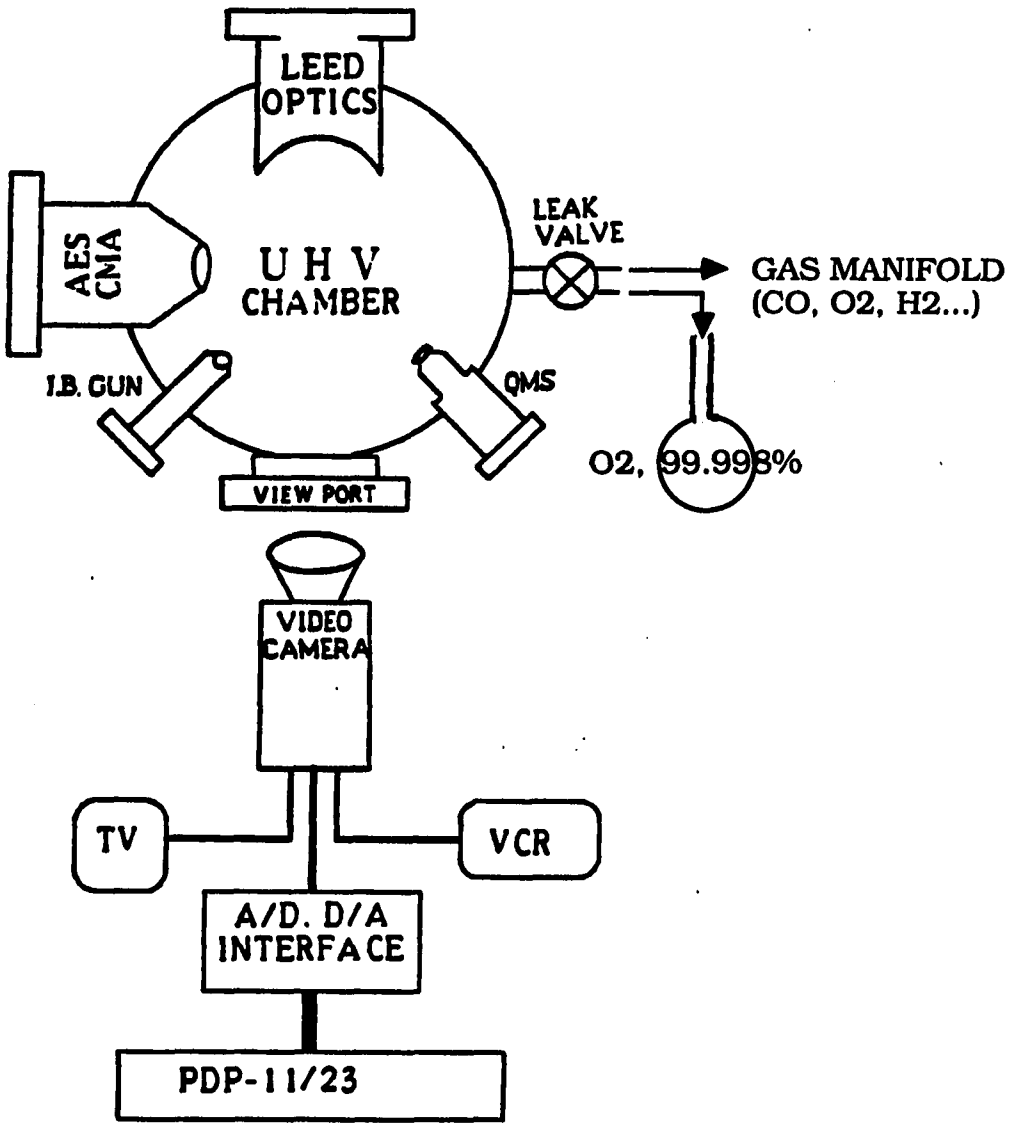

Figure 1. Schematics of ultrahigh vacuum system and computer-interfaced video-LEED used in this study.

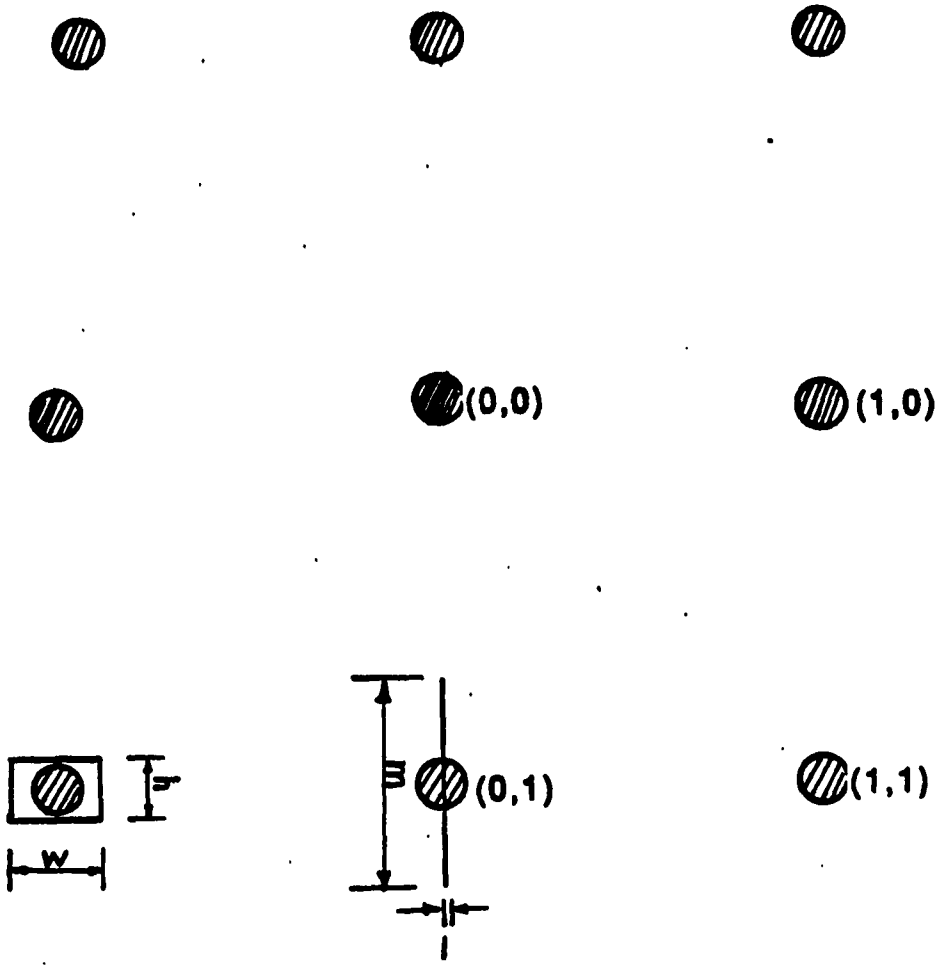

Figure 2. By setting an integration window w x h (rectangular or square shape) around the LEED spot, or a 1 x m window (slice) across the spot, the changes in spot intensity or spot shape and location vs. time, sample temperature or exposure can be monitored continuously

The parameters used in Auger electron spectroscopy (AES) are these: 2 kV incident beam energy, 1 V peak-to-peak modulation amplitude, unless otherwise specified, and 0.2 μA beam current. The nickel single crystal is disk-shaped, 1 mm thick and 9 mm in diameter, grown at the Materials Preparation Center of the Ames Laboratory. It is cut and polished to within 0.5° of the (100) orientation on both sides.

In vacuum, the sample is initially cleaned by successive cycles of annealing and ion-bombardment, with the annealing carried out in 50 K increments to a maximum temperature of 1150 K. The major contaminants depleted by this procedure are S and Cl. The carbon is then removed by repeatedly dosing the sample with oxygen and annealing to 1000 K, with occasional ion bombardment to remove a sporadic oxide.

Between experiments such as those described in this chapter, oxygen or oxide on Ni(100) is removed by ion bombardment at 550-600 eV, with 1.8 μA beam current, for 40 to 60 minutes, followed by annealing at 850 K for three minutes. Finally, residual carbon, as checked by AES after ion bombardment, is oxidized with small oxygen exposures (0.2 to 0.3 L) at 310 K, followed by heating in vacuum to 950-1000 K. Small oxygen exposures are used to avoid formation of oxide on the surface during cleaning. After the sample is free of carbon, oxygen, and other contaminants, as determined with AES, it is finally annealed at 1050 K in vacuum for a total of one hour. This gives a sharp LEED pattern with low background intensity. The halfwidth of the integral-order spots is 0.009 to 0.014 $Å^{-1}$. The LEED beam current is 0.5 to 0.7 μA.

Other authors report that conditions necessary for oxidation of

Ni(100) can depend on sample history, especially upon previous oxidations [9,24,42]. Some of them hypothesize that this is because the density of surface and bulk defects, as well as the amount of oxygen dissolved in the bulk, are functions of the sample's history [9,42]. (The concentration of dissolved oxygen must be small, however, since it is undetectable with AES in nominally-clean samples.) This thesis describes results only for one Ni(100) sample, cleaned as described above. The data are reproducible over the duration of the experiments, about twelve months. The crystal is not subjected to extensive oxidation at temperatures above 400 K, nor at oxygen pressures above 10^{-7} Torr, after its initial cleaning. We have not checked the extent to which our results may be sample-specific, or may be altered by a history of more vigorous oxidation.

Results

Oxygen adsorption at fixed temperatures

Figure 3 shows the relative intensities of O (503-507 eV) and Ni (848 eV) Auger transitions as a function of oxygen exposure, at seven different adsorption temperatures. At substrate temperatures of 400 K, 350 K, 300 K, 225 K, and 180 K, it can be seen that the curves exhibit a common distinctive shape. There is an initial sharp increase in the Auger ratio, followed by a plateau at intermediate coverages, then a second increase in oxygen uptake, and finally a last plateau. The value

Figure 3. Ratio of oxygen-to-nickel Auger signals as a function of oxygen exposure, at seven different sample temperatures. The Auger ratio uses the oxygen KLL line at 503-507 eV, and the nickel LMM line at 848 eV. The oxygen pressure is 5×10^{-9} Torr (at lowest exposures) to 1×10^{-7} Torr (at highest exposures) during oxygen dosing. Each arrow indicates the point where the right-hand edge of the plateau deviates from linearity. We define this as the oxidation threshold measured with AES.

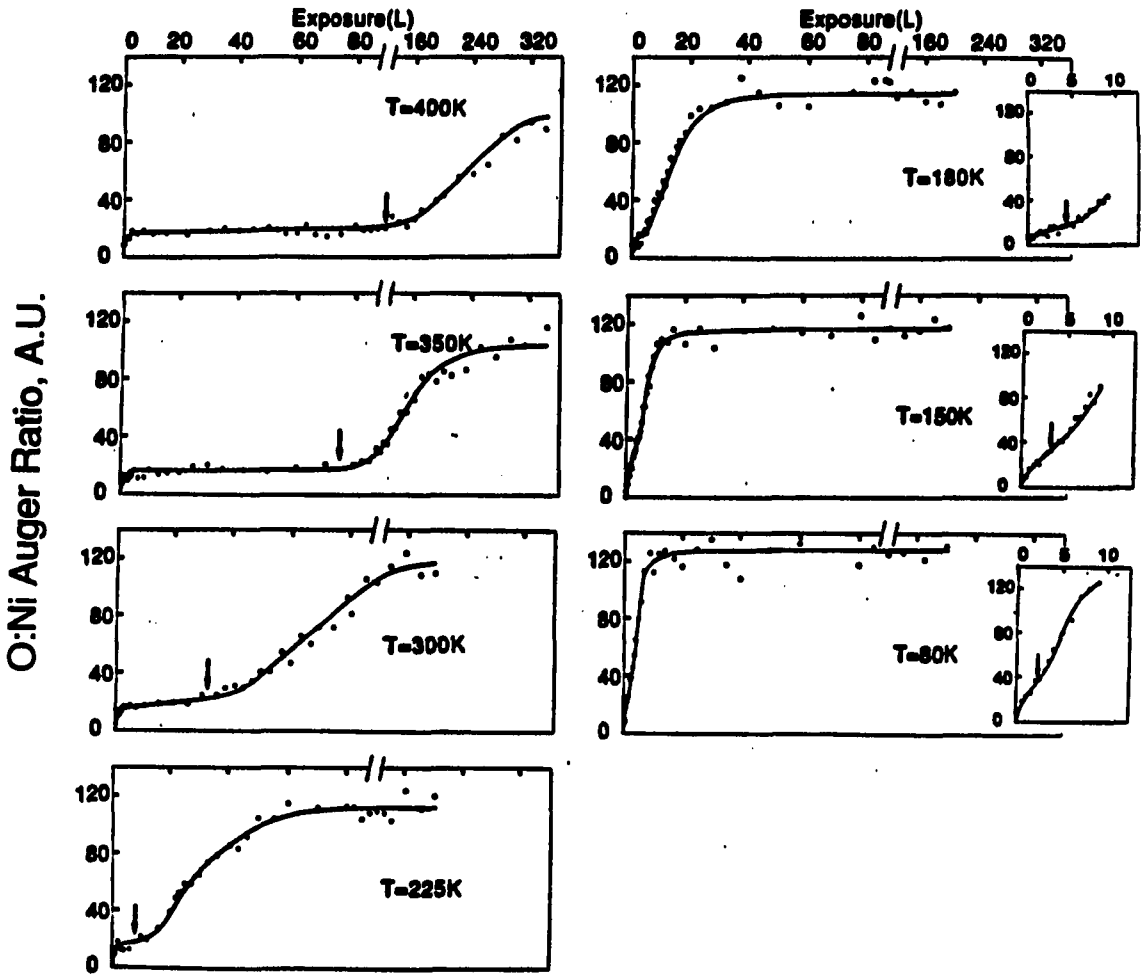
O:Ni Auger Ratio, A.U.
Exposure(L)
0 20 40 60 80 160 240 320
T=400K
T=350K
T=300K
T=225K
T=180K
T=150K
T=80K
0 40 80 120
0 5 10

of the Auger ratio at the first plateau is constant at 15 to 20, and the value at the last plateau falls in another narrow range, 100 to 110. Curves with similar shapes have been observed by many authors during oxidation of Ni surfaces [9 and references therein]. It is generally agreed that the end of the first plateau signals the onset of oxidation, and that growth of the oxide nuclei, and/or continuing formation of new nuclei, accounts for the second stage of rapid oxygen uptake [9]. It is also generally agreed that the onset of oxidation on Ni(100) occurs at a coverage below 0.50 monolayers, with values in the range 0.35 to 0.45 most often reported [9-12,23-26], while the second plateau corresponds to two or three layers of oxide [9,23-26]. The length of the first plateau decreases as temperature falls until, at the lowest two temperatures in Fig. 3, 150 and 80 K, only a trace remains. A decrease in the exposure spanned by the first plateau has also been observed by other authors, from temperatures of 400 to 300 K, and the absence of a plateau at 150 K or below has been reported too [9,23,25,26,29].

The oxidation threshold is determined from data such as those shown in Fig. 3, by defining it as the point where the right-hand edge of the plateau first deviates from linearity. It is shown in each panel of Fig. 3 by an arrow. Note that the linear plateau is horizontal only at $T \geq 300$; as temperature falls, it tilts increasingly upward. This may indicate that some oxidation begins even before the end of the "plateau", in fact the rising plateau almost seems to indicate that there are two superposed kinetic processes, one which leads to a plateau and one which leads to a constant rise in the extent of oxidation. The oxidation

kinetics associated with the plateau dominate at high temperatures, whereas the kinetics associated with the more constant rate of oxidation dominate at lower temperature.

In Fig. 4, we show photographs of the LEED patterns which develop during oxidation of Ni(100). A typical sequence of patterns during adsorption starts with the clean (1x1), then progresses to the p(2x2) (not shown), and continues with the c(2x2). The c(2x2) is subsequently destroyed as oxidation progresses. At that point, a NiO(111) surface, or a (7x7) pattern, can form, depending on the adsorption temperature. A NiO(100) surface can also be formed with a high oxygen exposure, followed by heating to T > 550 K. Figure 4A displays the LEED pattern of the clean Ni surface, while Fig. 4B displays a c(2x2) pattern. Figure 4C is a photograph of the pattern of NiO(111), which consists of 12 first-order spots arranged in a ring around the (0,0) spot (the "ring" pattern). This is actually a superposition of patterns from two degenerate NiO(111) domains, rotated by 30° [27,34]. Figure 4D shows the (7x7), coexistent with ring and c(2x2) patterns, and Figure 4E shows the (7x7) alone. Figure 4F presents the pattern associated with NiO(100), coexistent with the p(1x1) and c(2x2). In this work, some of the LEED patterns of Fig. 4 begin to be apparent at about 130 K; nothing appears at lower temperature. This is in agreement with other authors, who state that no patterns are visible upon adsorption at 80 K [29], and that the patterns are "barely detectable" (visually) upon adsorption at ca. 150 K [23].

All of these patterns, and the associated real-space structures, have been observed and discussed many times by others [e.g., 9 and

Figure 4. Photographs of LEED patterns. In each photo, the upward arrow indicates the (1,0) spot, and the downward arrow shows the $(\bar{1},0)$ spot. The dark shadow in the center is the sample and manipulator.

(A) p(1x1) of the clean Ni(100) substrate, at 87 eV beam energy.

(B) c(2x2) following 39 L oxygen exposure at 300 K, at 70 eV beam energy.

(C) NiO(111) "ring" pattern, observed after 200 L oxygen exposure at 225 K. Beam energy is 60 eV.

(D) (7x7) pattern plus c(2x2) and NiO(111) "ring", obtained after 200 L exposure at 300 K, at 45 eV beam energy.

(E) (7x7) pattern, observed when the sample is exposed to 570 L O_2 at 350 K, then cooled to 80 K. Beam energy is 50 eV.

(F) NiO(100) pattern (very diffuse spots), plus p(1x1) and c(2x2), observed after 175 L exposure at 225 K, followed by heating to 605 K and cooling to room temperature. Beam energy is 88 eV.

(A)

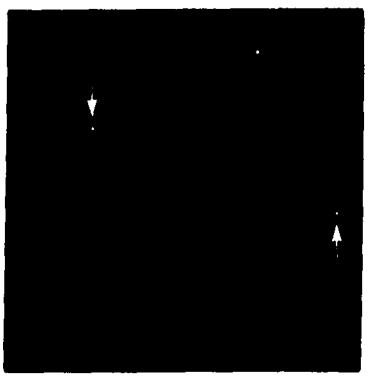

(D)

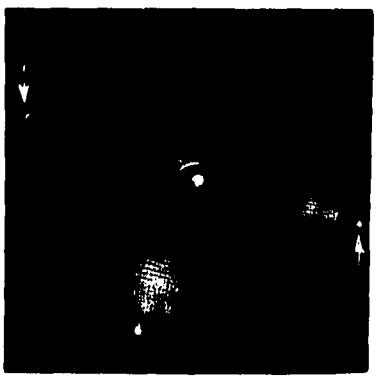

(B)

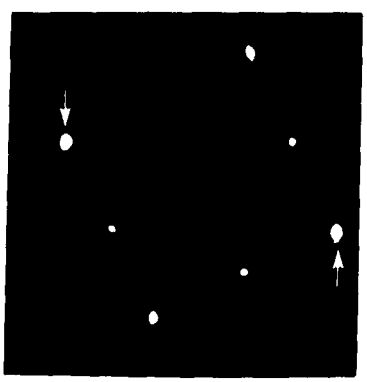

(E)

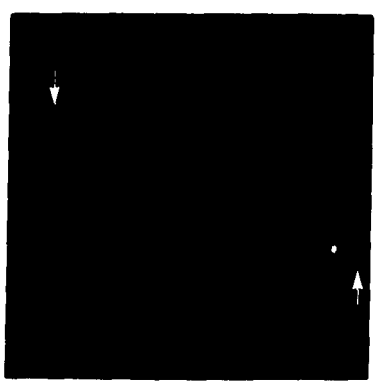

(C)

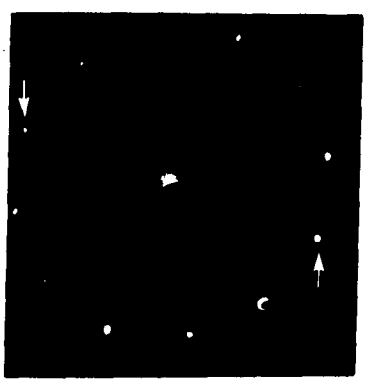

(F)

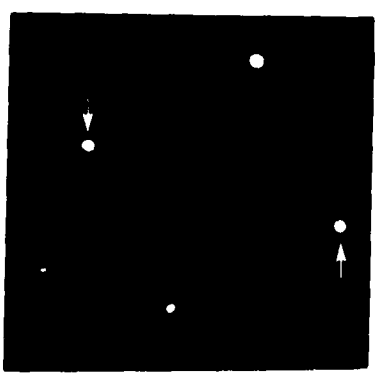

referred references therein], with the exception of the (7x7). The (7x7) is always faint, and associated with a high local background (as seen in Fig. 4D and E). Only the spots close to the integral-order spots are ever visible. This may account for the fact that it has been reported for the first time very recently, by Saiki et al. [33]. It can be speculated that the high local background may have been mistaken by other authors for the diffuse spots of the NiO(100) pattern. In the experiments, there appear to be two distinct types of (7x7), distinguished by the relative intensities of various seventh-order spots. In particular, the relative intensities of the (0,5/7) and (0,6/7) features are reversed in the two seventh-order patterns, a trait which can be noticed in some of the data presented here. In this chapter, both of these structures are refered to as (7x7), or (7x7)-like; a detailed discussion of their possible origins can be found in the next chapter. Another point of note is that the diffraction features usually do not quite appear at seventh-order positions, as Saiki et al. have also noted [33]. For simplicity, however, they are refered to as (a/7,b/7) spots, where a and b are integers with values from zero to six.

Figure 5 shows variations in LEED spot intensities as functions of increasing oxygen exposure, at substrate temperatures of 400 to 150 K. Figure 5A illustrates the general trends. At T = 400 K, the intensity of the (0,1/2) spot (curve a) first increases, reaching a maximum at 1.8 ± 0.5 L, then decreases as oxygen continues to adsorb. This signals the growth and subsequent destruction of the p(2x2) lattice as oxygen coverage increases. Meanwhile, the (1/2,1/2) spot (curve b)--which

Figure 5. Variations in integrated LEED spot intensities as a function of oxygen exposure, at six different sample temperatures. Note that the exposure range of Fig. 5F (T = 150 K) is four times smaller than that of the other five panels, A-E. The beam energy is 70 eV, and the oxygen pressure is 5 to 6 x 10^{-9} Torr.

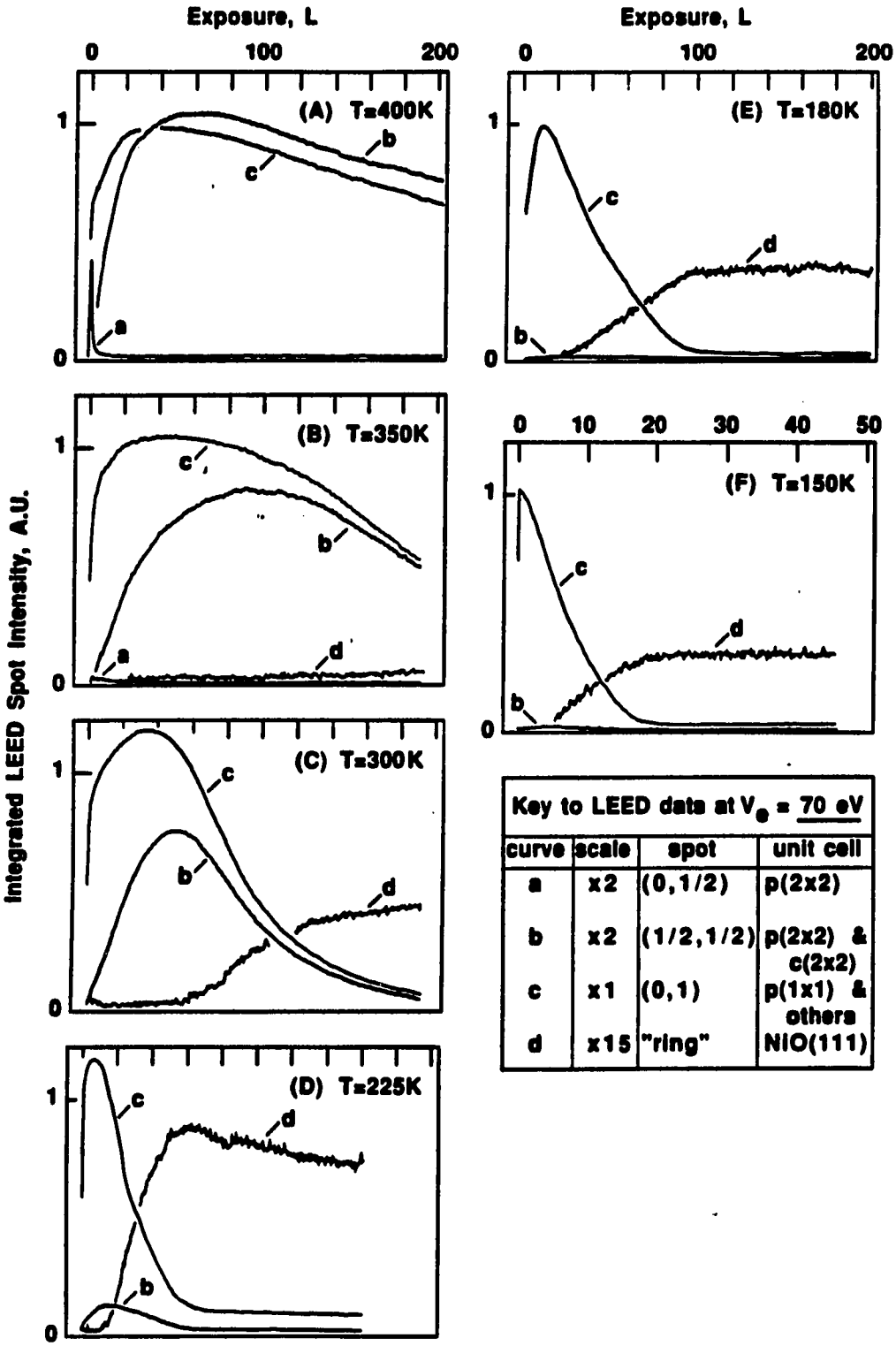

Key to LEED data at V_e = 70 eV			
curve	scale	spot	unit cell
a	x2	(0,1/2)	p(2x2)
b	x2	(1/2,1/2)	p(2x2) & c(2x2)
c	x1	(0,1)	p(1x1) & others
d	x15	"ring"	NiO(111)

represents only the c(2x2) lattice at exposures above 10 L-- intensifies, reaching a broad maximum at an exposure of ca. 60 L. The (1,0) spot intensity (curve c) varies in a way which mimics that of the (1/2,1/2), except that it consistently passes through a maximum at lower exposure than does the (1/2,1/2) spot. For instance, in Fig. 5A the (1,0) maximum is at 40 L, 20 L below that of the (1/2,1/2) spot. Figures 5B-F show analogous results for adsorption temperatures of 350, 300, 225, 180, and 150 K, respectively. The quality of the p(2x2) degrades markedly as substrate temperature falls, based on the lower intensity maximum for the (0,1/2) spot (curve a), in going from Fig. 5A to 5B. In fact, at $T < 400$ K, the p(2x2) is no longer visible on the scale of Fig. 5. However, the exposure at which the p(2x2) reaches maximum intensity, 1.8 ± 0.5 L, is independent of temperature, within the temperature range where it is measurable at all(225 to 400 K). The maximum intensity of the c(2x2) (curve b) also falls as temperature decreases, particularly below room temperature. At temperatures of 300 K or below, however, the ring pattern of the NiO(111) structure becomes visible, as evidenced by curve d in Fig. 5B-F. Indeed, the ring pattern reproducibly achieves its maximum brightness when oxidation is carried out at 225 K.

Inspection of Fig. 5 reveals that several surface events are correlated. First, at $T \leq 350$ K, the exposure at which the c(2x2) pattern (curve c) reaches maximum brightness always corresponds, within about 10%, to the threshold for emergence of the NiO(111) pattern (curve d). Furthermore, this "threshold exposure" increases markedly with substrate temperature, as illustrated by Fig. 6. The threshold exposure

Figure 6. The "threshold exposure", i.e., the exposure at which the ring pattern, or the (7x7) pattern, first appears, as a function of sample temperature. These exposures are taken from LEED data such as curves d and e in Figs. 5 and 7, and are shown without error bars in Fig. 6. The exposure at the end of the first plateau in O:Ni Auger intensity (arrows in Fig. 3) is also shown as a function of temperature, by circular symbols. Error bars shown for the latter data indicate the subjective uncertainty in exposure for each individual measurement, rather than a statistical uncertainty. The solid line is drawn to guide the eye.

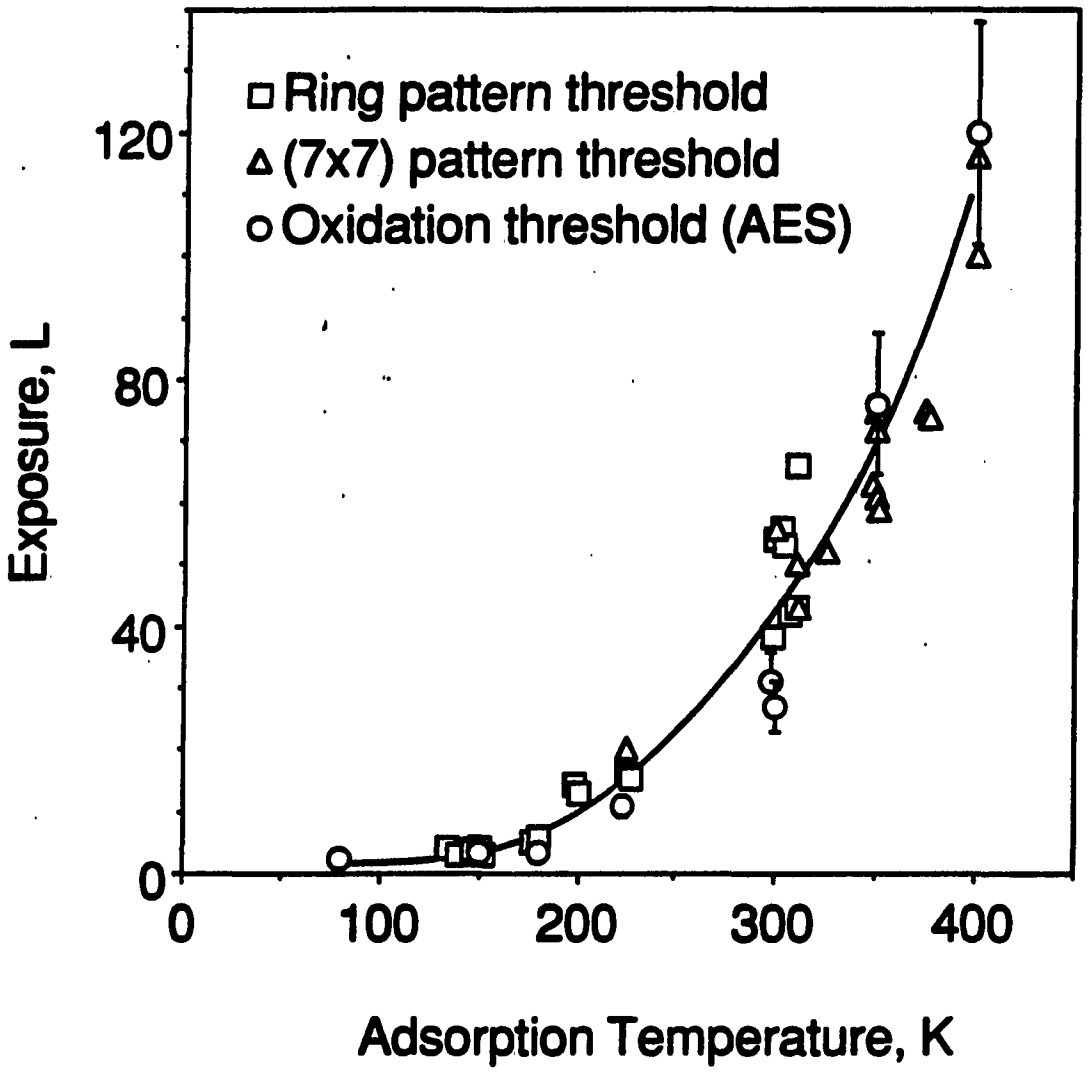
Ring pattern threshold
(7x7) pattern threshold
Oxidation threshold (AES)
Exposure, L
120
80
40
0
0
100
200
300
400
Adsorption Temperature, K

increases by more than a factor of ten (from 4 L to 40-60 L), as substrate temperature increases from 150 to 300 K. Figure 6 offers a comparison of the exposure at which the NiO(111) pattern first appears in LEED (square symbols), with the exposure at the end of the first plateau in the AES intensity of Fig. 3 (circular symbols). It can be seen that there is no significant difference between the two sets of data at any temperature.

Figure 7 represents results from the LEED experiments when conditions of beam energy and sample temperature are chosen to optimize the (7x7) pattern. Note first that many of the trends of Fig. 5 are reproduced, including the fact that the (1,0) spot (curve c) and the (1/2,1/2) spot (curve b) pass through successive maxima. Also, the maximum brightness of the NiO(111) ring pattern (curve d) increases as substrate temperature falls from 400 to 300 K, an effect visible also in the data of Fig. 5. However, the new information contained in Fig. 7 regards the formation of the (7x7) LEED pattern, represented by curve e.

The (7x7) pattern consistently emerges at about the same exposure where the c(2x2) intensity starts to decline. This exposure, shown by the triangles in Fig. 6, increases with increasing temperature, and correlates fairly well with the end of the first plateau in Auger intensity (circles in Fig. 6). In this sense, the (7x7) mimics the behavior of the NiO(111) ring pattern observed in a lower temperature range (squares in Fig. 6.) This is evidence that the (7x7) pattern represents an oxide, as does the ring pattern. This point will be further discussed in Chapter 3. Furthermore, the (7x7) reaches maximum

Figure 7. Variations in integrated LEED spot intensities as functions of oxygen exposure, at five different sample temperatures. The beam energy, 46 eV, is chosen to optimize the intensity of the (7x7) pattern. The oxygen pressure is 5 to 8 x 10^{-8} Torr. Note that curve e in frames (D) and (E) is displaced vertically for clarity.

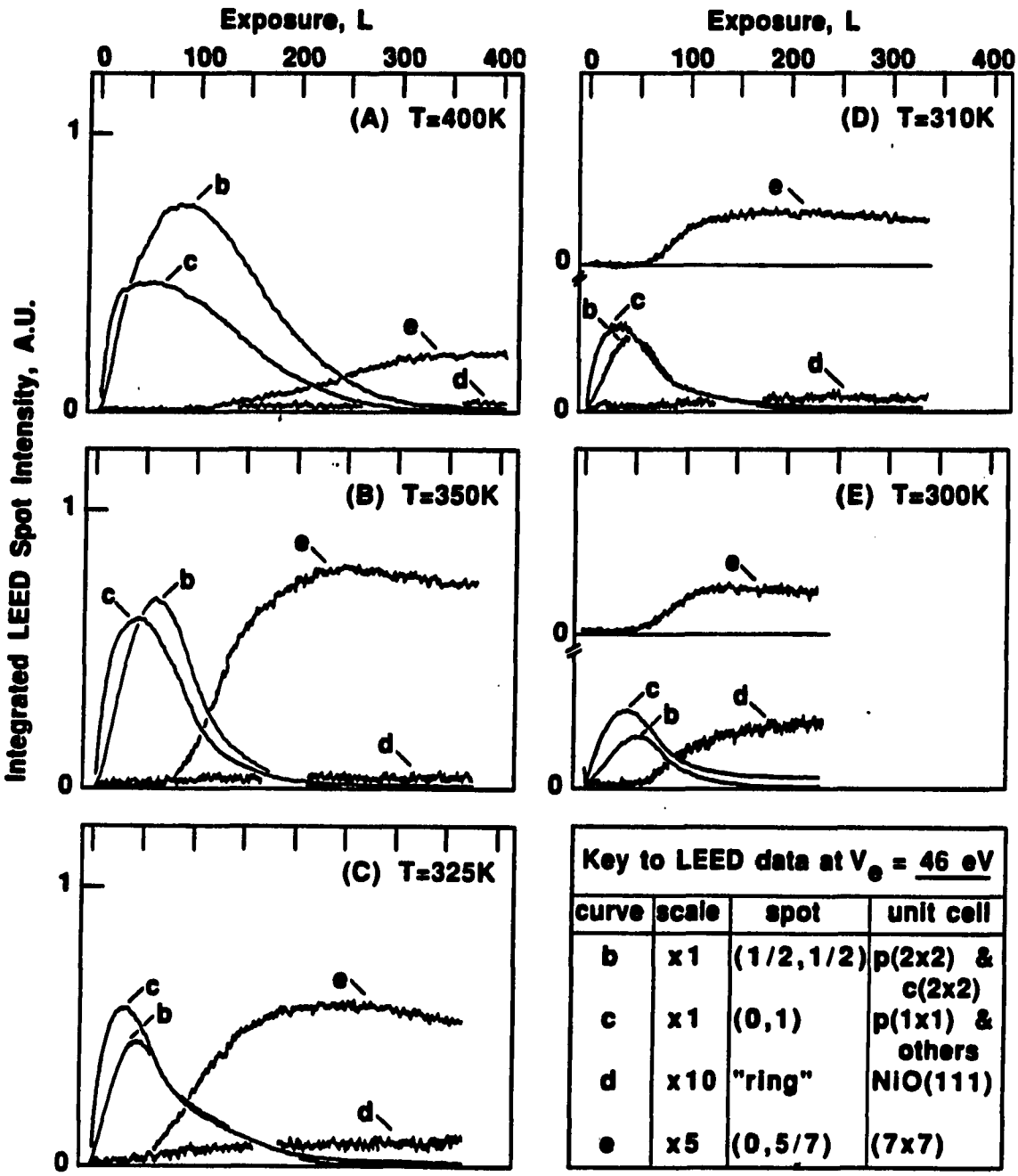

Key to LEED data at V_e = 46 eV			
curve	scale	spot	unit cell
b	x1	(1/2,1/2)	p(2x2) & c(2x2)
c	x1	(0,1)	p(1x1) & others
d	x10	"ring"	NiO(111)
e	x5	(0,5/7)	(7x7)

intensity at an adsorption temperature of 350 K; at higher or lower temperatures, the pattern is fainter. A remnant of the (7x7) is visible at 225 K, but not below.

As shown by Fig. 4D-E, and as noted previously, the (7x7) pattern is superposed on a high background intensity. Therefore, it is necessary to check whether the intensities given by curve e throughout Fig. 7 might be due to some artifact of this background intensity, and of our background subtraction procedure, rather than distinct (7x7) spots. Therefore, profiles of the (7x7) spots are measured. For instance, the profiles which correspond to the experiment of Fig. 7B are shown in Fig. 8. In Fig. 7B, the intensity of the (7x7) pattern rises above zero at about 70 L; in Fig. 8, the (7x7) spots begin to appear also at about 70 L. Based upon this and other comparisons of the data, the intensities given by curve e in Fig. 7 are not artifacts of the diffuse background intensity.

Figure 9 summarizes the maximum intensities of some diffraction features associated with nickel oxide, as a function of the substrate temperature during oxidation. It can be seen from this representation, as well as from the data of Figs. 5 and 7, that the ring structure of the NiO(111) pattern becomes brightest <u>below</u> room temperature (between 200 and 300 K). Correspondingly, the (7x7) reaches maximum intensity <u>above</u> room temperature, between 300 and 400 K. The temperature of 300 K is a "crossover point" between the ring structure and the (7x7) structure. This may account for some of the discrepancy between other laboratories' results, since a great deal of the previous work has been done at or near 300 K--the crossover point [<u>23</u>,<u>24</u>,<u>32</u>].

Figure 8. LEED spot profiles taken during increasing oxygen exposure at T = 350 K, as in Fig. 7B. Some curves are labelled with values of oxygen exposure in Langmuir. Each profile has been corrected by substraction of a constant background, as described in Chapter 2. This procedure does not change the positions of peaks along the x-axis measurably. Each profile passes through the (-1/7, 6/7), (0, 6/7), and (+1/7, 6/7) spots.

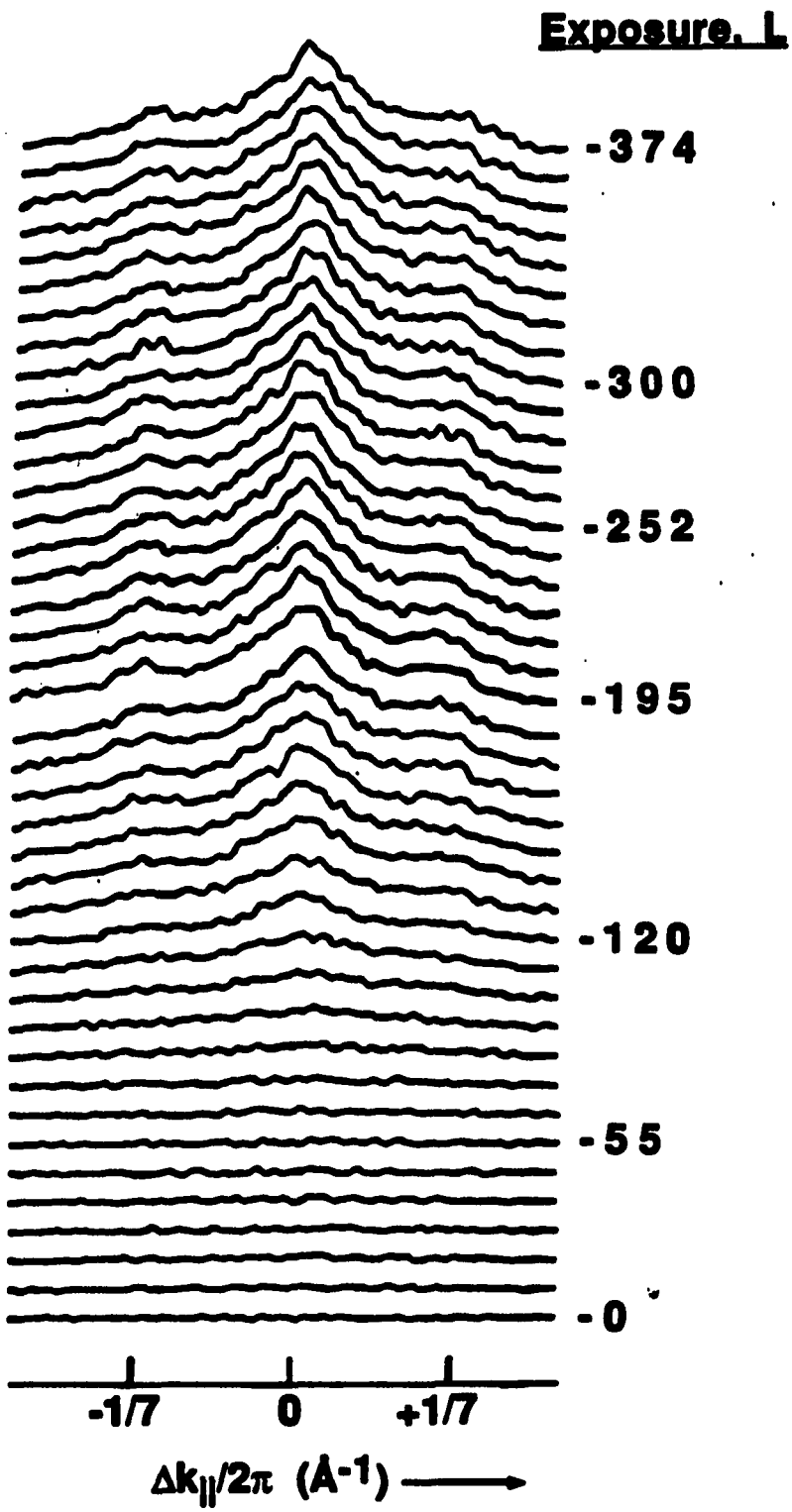
Exposure, L
-374
-300
-252
-195
-120
-55
-0
-1/7
0
+1/7
Δk∥/2π (Å-1)

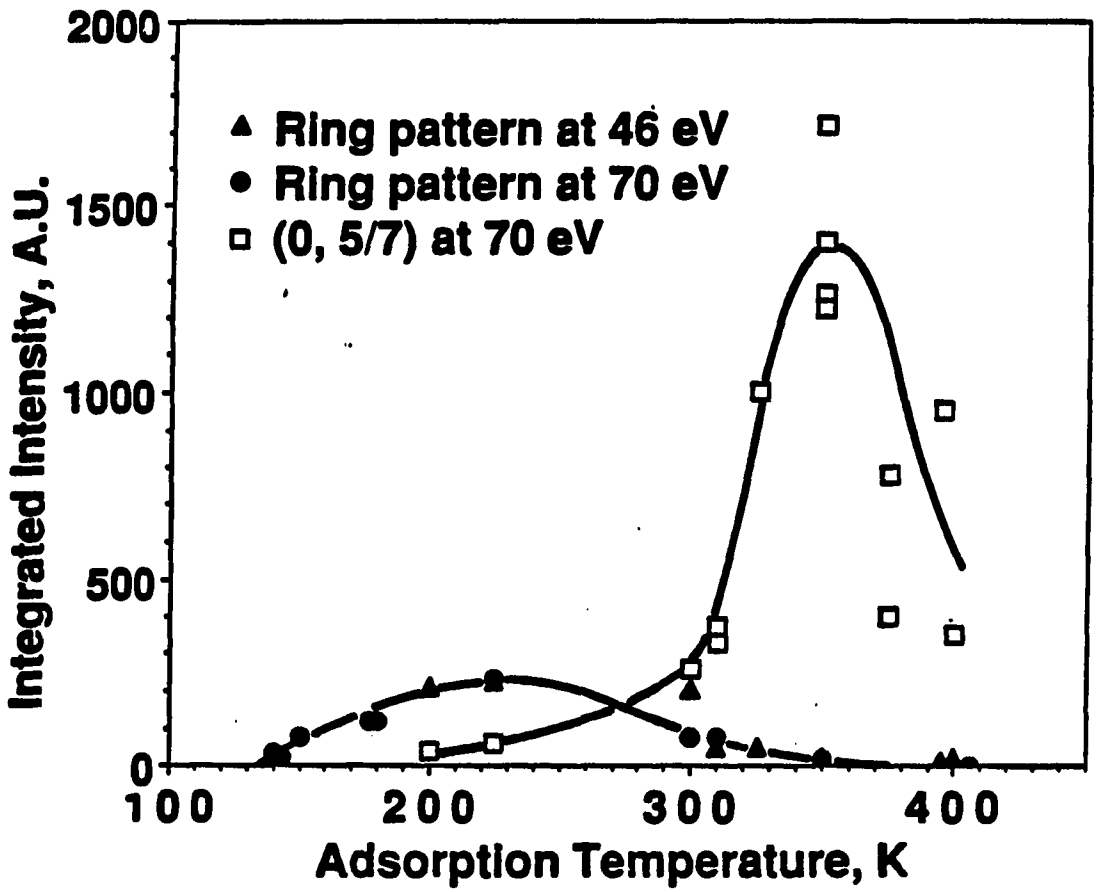

Figure 9. Maximum absolute intensity of ring and (0, 5/7) spots as a function of sample temperature during oxidation, taken from data such as those shown in Figs. 5 and 7. The intensities are measured at two different beam energies: 70 and 46 eV. The intensities at 70 eV are normalized to those at 46 eV, using the 225 K data for the ring pattern. The oxygen pressure ranges from 5 to 8 x 10^{-9} Torr for the 46 eV data, and 5 to 15 x 10^{-9} Torr for the 70 eV data.

Thermally-induced changes after adsorption

The evolution of LEED patterns have been examined when an oxidized sample is heated in vacuum, using samples prepared with a variety of total exposures, oxygen pressures, and adsorption temperatures. This discussion focuses on two particular experiments which are representative of many others.

First, consider the case of a sample oxidized at adsorption temperatures of 180 to 225 K, where the oxide grows with the (111) surface orientation. Specifically, consider a sample which is first exposed to 80 L O_2 ($P = 8 \times 10^{-8}$ Torr) at T = 200 K. Figure 5D and E demonstrate that these adsorption conditions are sufficient to complete the ring structure, and annihilate both the (1x1) and c(2x2) patterns. Note also from Fig. 9 that 200 K is close to the optimal adsorption temperature for NiO(111) formation. When this sample is heated, then cooled, in vacuum, the data of Fig. 10 result.

The variation of temperature with time is displayed in Fig. 10A, and selected temperatures are noted. Figure 10B-E displays integrated spot intensities as a function of time during this temperature program. As the sample is first heated, both the (0,1) spot and the (1/2,1/2) spot reappear and intensify, starting at 535 K. These two spots brighten rapidly between 535 and 610 K, then brighten more slowly between 610 and 660 K. The latter temperature marks the point where heating stops and cooling begins. Meanwhile, the ring pattern fades continuously and gradually until 550 K, then drops rapidly to zero between 550 and 610 K.

Figure 10. Temperature and LEED intensities as functions of time, starting from a NiO(111)-covered surface. The surface is prepared from Ni(100) by oxidation at 200 K, in 8 x 10^{-8} Torr oxygen, and with 80 L total exposure. The LEED intensities are measured at 70 eV.

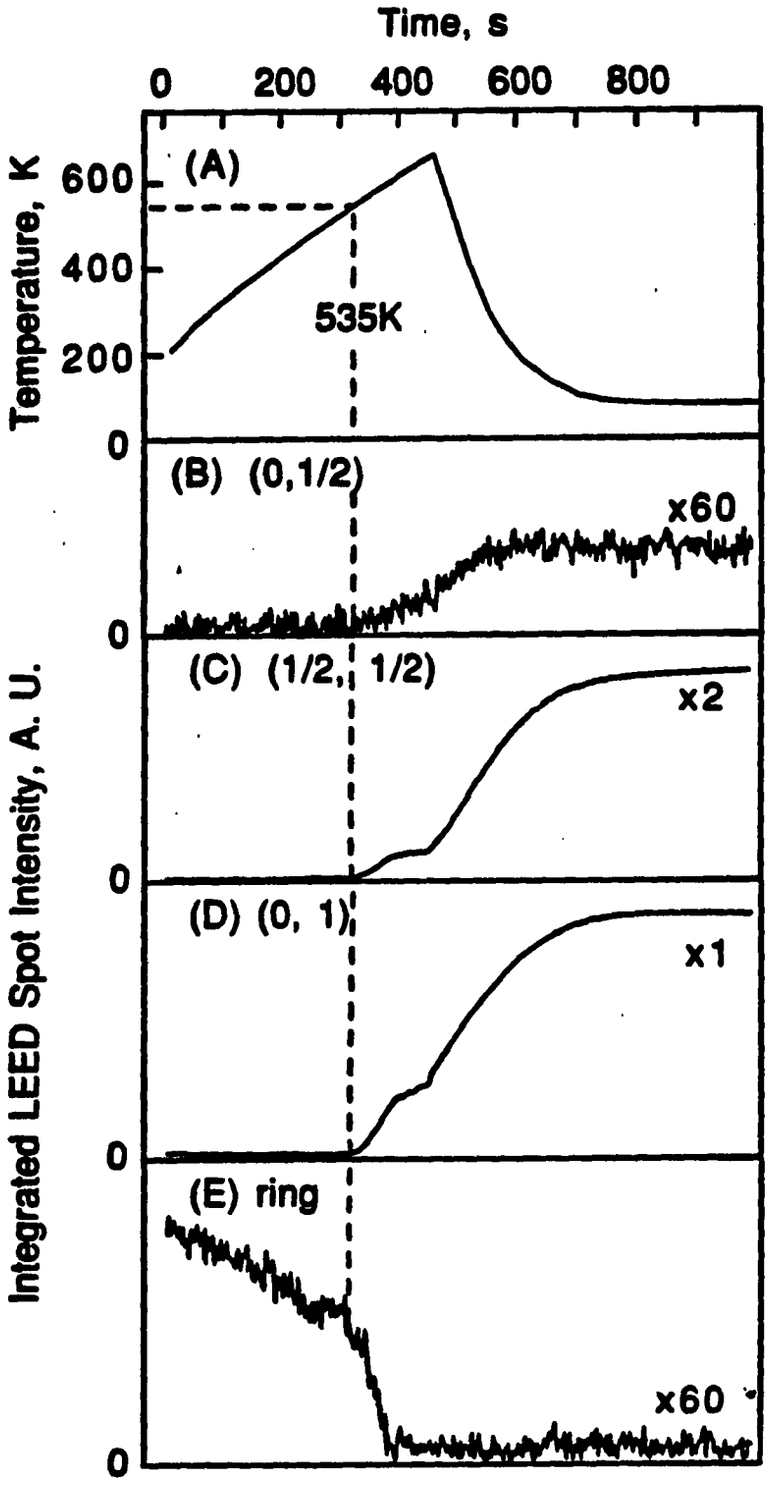
Time, s
0
200
400
600
800
Temperature, K
600
400
200
0
(A)
535K
(B) (0,1/2)
x60
(C) (1/2, 1/2)
x2
(D) (0, 1)
x1
(E) ring
x60
Integrated LEED Spot Intensity, A. U.
0
0
0
0

Other experiments show that the intensity decrease of the ring pattern between 200 and 500 K is reversible, and is thus due to Debye-Waller attenuation. Clearly, the emergence of the c(2x2) and (1x1) patterns is linked to the disappearance of the ring pattern, although the former two events begin about 15 K lower in temperature than does the latter, in this experiment. The average temperature at which the c(2x2) reappears is 540 ± 20 K, and the average temperature at which the ring pattern disappears is 560 ± 20 K. These values are based upon four similar experiments with samples oxidized at temperatures of 200 to 225 K. Furthermore, all three events are irreversible, as shown by the intensity variations during the cooling part of the cycle in Fig. 10. Spot profiles indicate that disappearance of the NiO(111) pattern coincides in temperature with the emergence of the NiO(100) pattern. This is shown by Fig. 11, where the NiO(111) spot diminishes between the 130th and 150th profile, T = 500-552 K, and the intensity of the NiO(100) spot starts to increase slightly below 500 K. When the sample cools down after heating up to 575 K, the ring spot does not reappear in the profiles.

The first conclusion from these data is that irreversible changes in surface structure occur above 500 K. These changes mimic those which take place during adsorption (Fig. 5D and E), but in reverse sequence: the c(2x2) and (1x1) patterns re-appear, and the ring structure disappears. In short, the sample behaves as if oxygen coverage drops and a metallic Ni(100) surface is restored (at least partially). This point will be further discussed in Chapter 3. These events coincide with emergence of the NiO(100) pattern. Thus, NiO(100) and metallic Ni(100)

Figure 11. Showing the correlation of the two structures, NiO(111) and NiO(100), and the irreversibility of phase transition. It is obtained from annealing the oxygen covered surface after adsorption at 130 K with pressure 1.2×10^{-8} torr for 6 L, measured at 64 eV.

(A) The temperature variation curve of the annealing process.

(B) Marks the positions of the spots (blackened) that are monitored during annealing.

(C) Intengrated spot intensity of NiO(100).

(D) Profiles of NiO(111) spot during annealing.

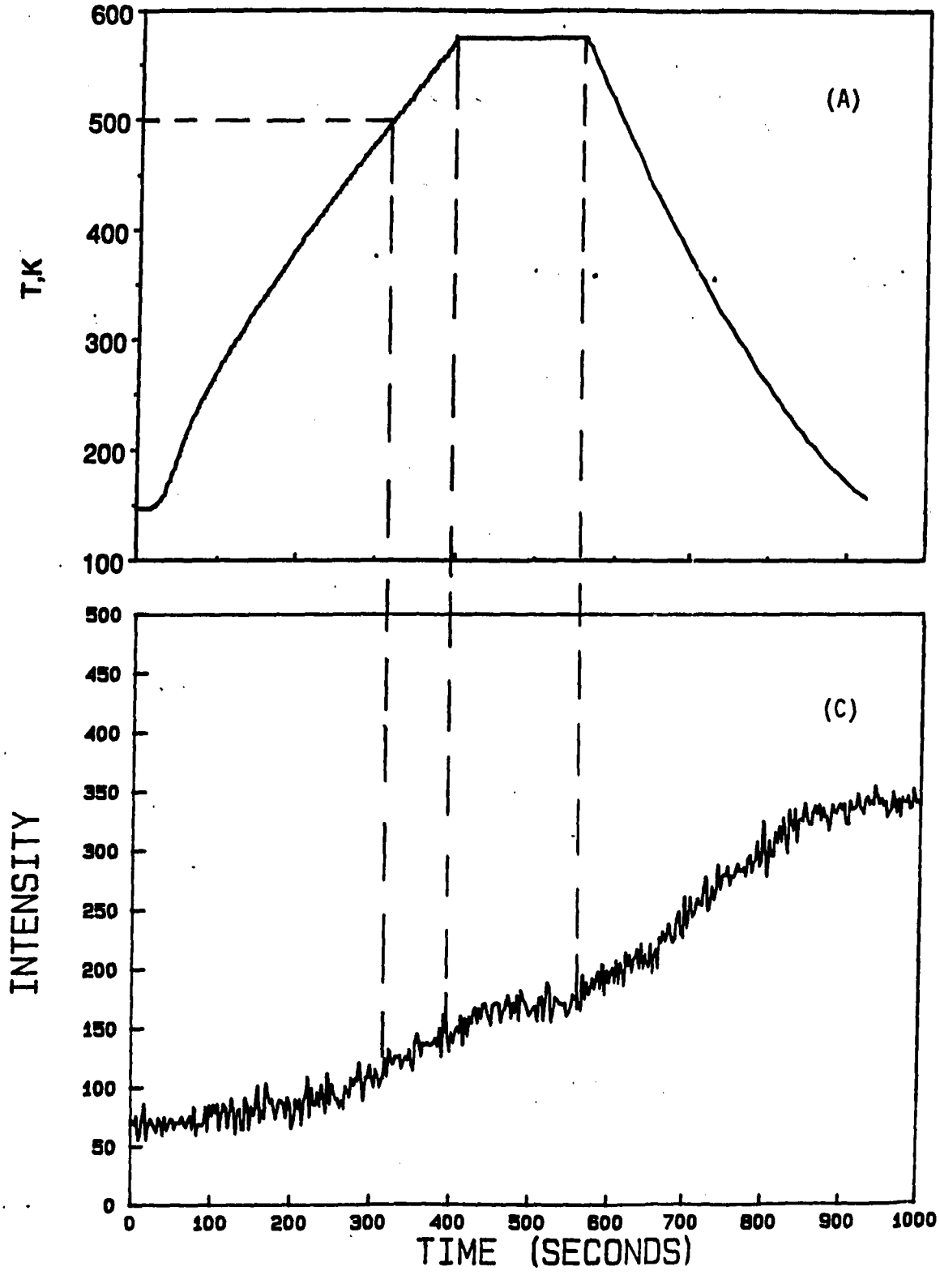
600
500
400
300
200
100
T,K
(A)
500
450
400
350
300
250
200
150
100
50
0
INTENSITY
(C)
0
100
200
300
400
500
600
700
800
900
1000
TIME (SECONDS)

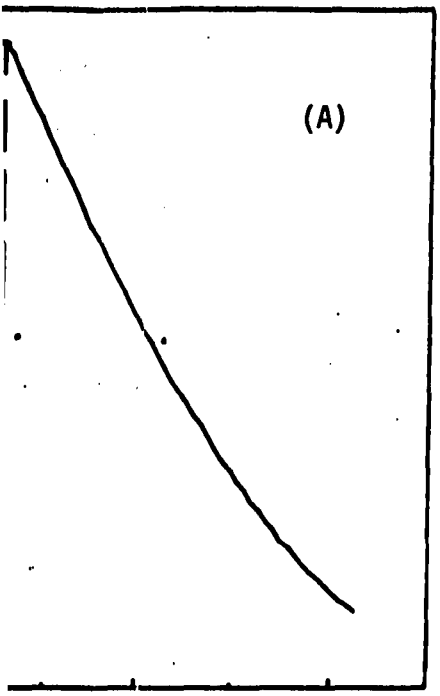
(A)

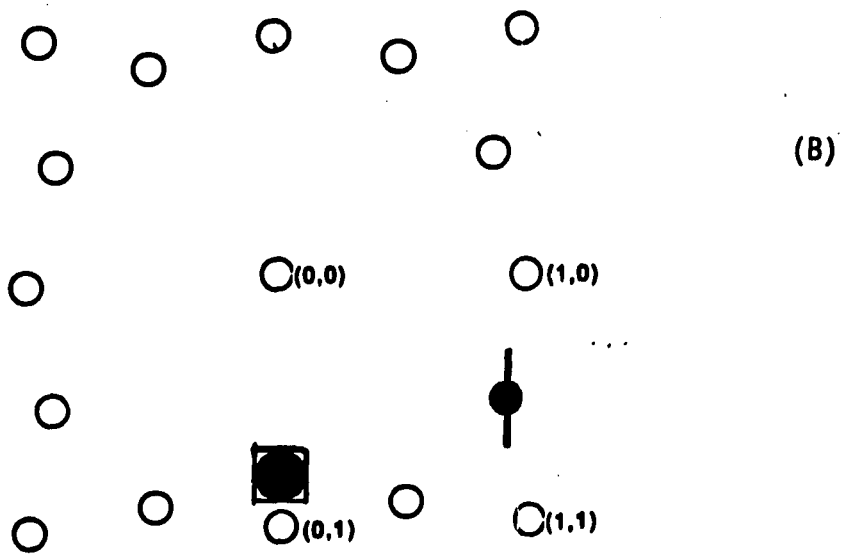
(B)
(0,0)
(1,0)
(0,1)
(1,1)

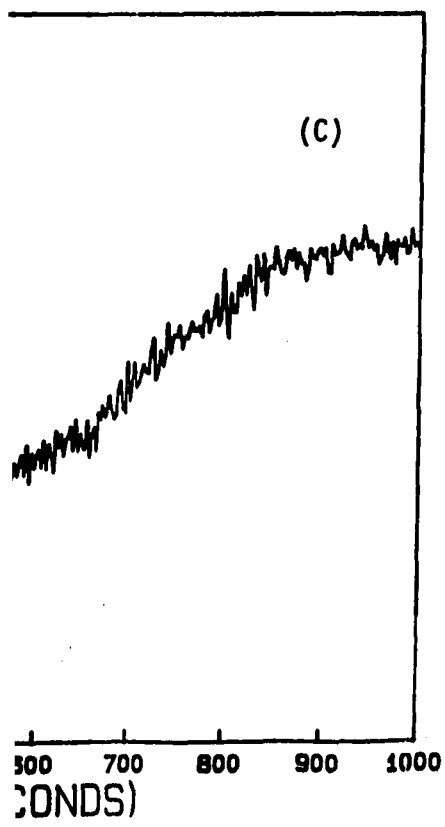
(C)
500
700
800
900
1000
CONDS)

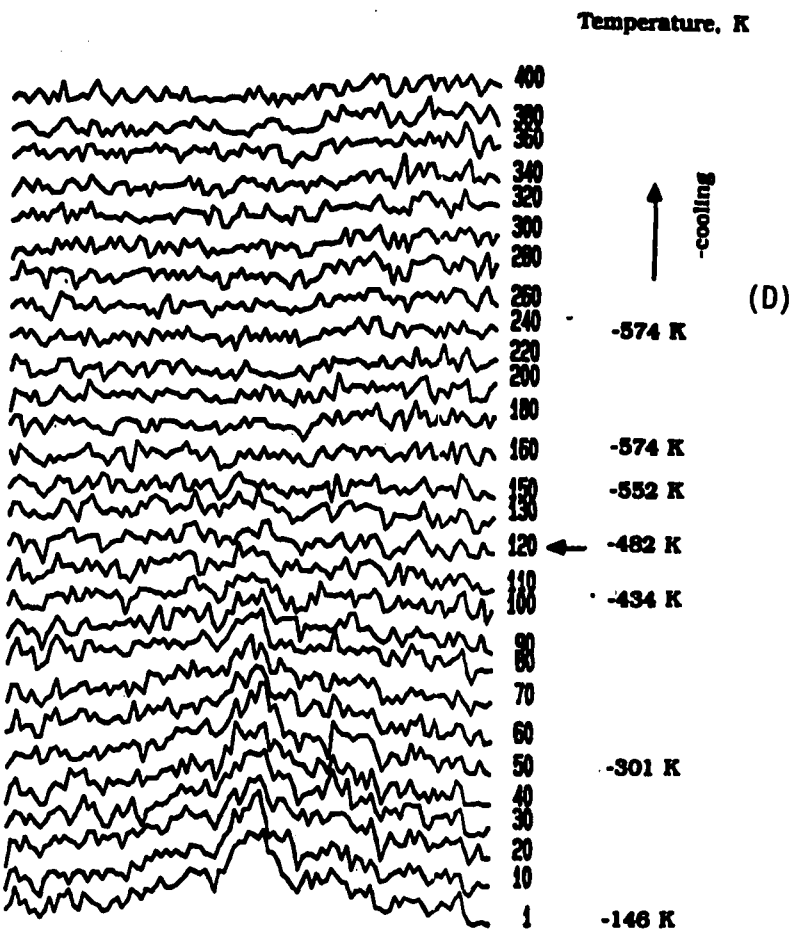
Temperature, K
-cooling
(D)
-574 K
-574 K
-552 K
-482 K
-434 K
-301 K
-146 K

form at the expense of NiO(111).

The second conclusion from these data is that the ring pattern, once formed, is stable up to 500 K. Its intensity attenuates by approximately 20% between 200 and 500 K, due to the Debye-Waller effect, but the pattern is clearly visible nonetheless even up to 500 K. This is important for understanding why the ring pattern is not visible during adsorption at T > 300 K, as shown by Figs. 5, 7, and 9. Clearly, its absence under those conditions must reflect the fact that the NiO(111) structure does not form. Its absence cannot be due to thermal dissolution, or Debye-Waller attenuation. As will be shown in Chapter 4, after more than ten sequential heating-cooling cycles of NiO(111) to above 400 K, the ring pattern still persists, and does not degrade from dissolution.

Now consider the situation when the oxidized sample is prepared at adsorption temperatures of 300 to 400 K, in which case the oxide takes the form of the (7x7) structure. For the particular experiment chosen to be presented here, the sample is first oxidized with an exposure of 370 L O_2 ($P = 8 \times 10^{-8}$ Torr) at T = 350 K. Figure 7B demonstrates that these adsorption conditions are sufficient to complete the (7x7) pattern, and erase the (1x1) and c(2x2) patterns. When this sample is heated in vacuum, Fig. 12 and 13 show the results.

Figure 12B-E displays integrated spot intensities as a function of time, while the sample is heated and cooled in vacuum. The variation of temperature with time is displayed in Fig. 12A, and selected temperatures are noted in subsequent panels. The variation of the (0,1) spot

Figure 12. Temperature and LEED intensities as functions of time, starting from a (7x7)-covered surface. The surface is prepared from Ni(100) by oxidation at 350 K, in 8 x 10^{-8} Torr O_2, and with 370 L total exposure. The LEED intensities are measured at 46 eV.

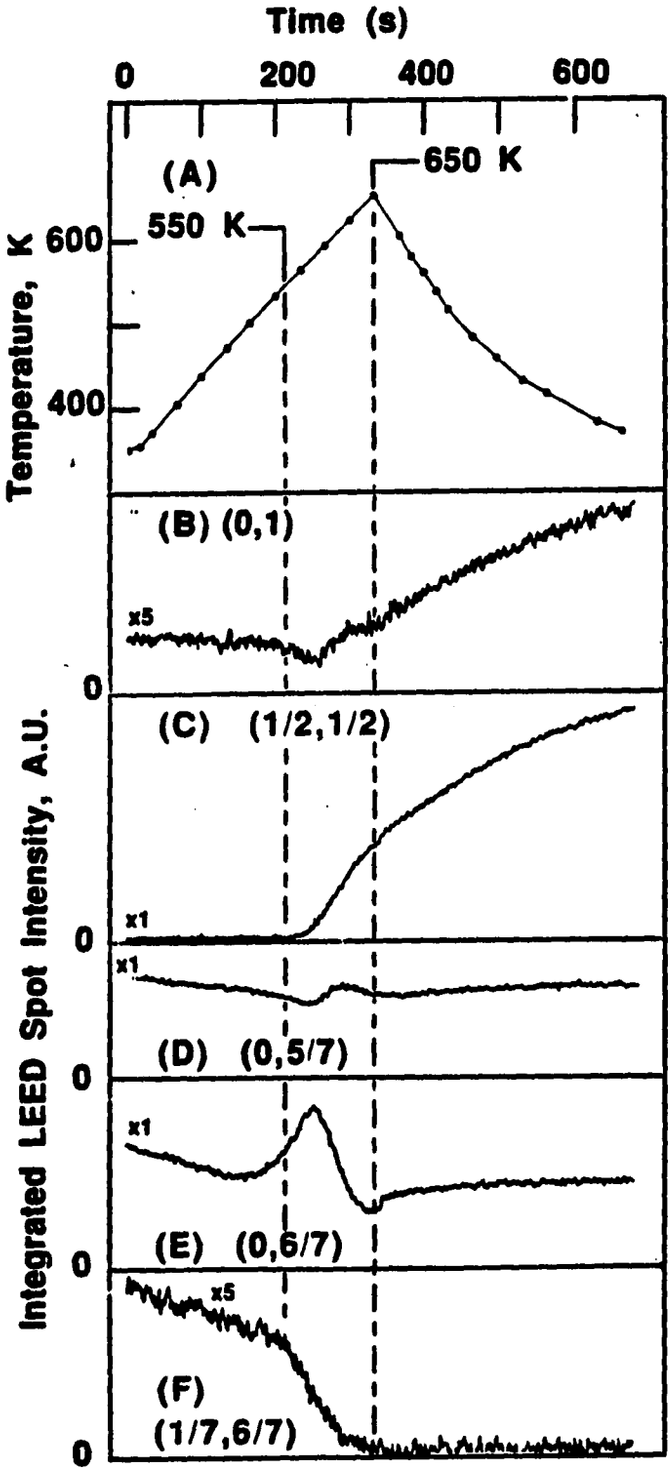
Time (s)
0
200
400
600
(A)
650 K
550 K
Temperature, K
600
400
(B) (0,1)
x5
0
(C) (1/2,1/2)
x1
0
x1
(D) (0,5/7)
0
x1
(E) (0,6/7)
0
x5
(F)
(1/7,6/7)
0
Integrated LEED Spot Intensity, A.U.

Figure 13. LEED spot profiles as a function of time, corresponding to the heat-cool cycle of Fig. 12A. Each profile intersects the (0, 5/7), (0, 6/7) and (0,1) spots. The profiles are measured at 46 eV. Each profile has been corrected by subtraction of a constant background, as described in Chapter 2. This procedure does not affect the positions of peaks along the x-axis measurably.

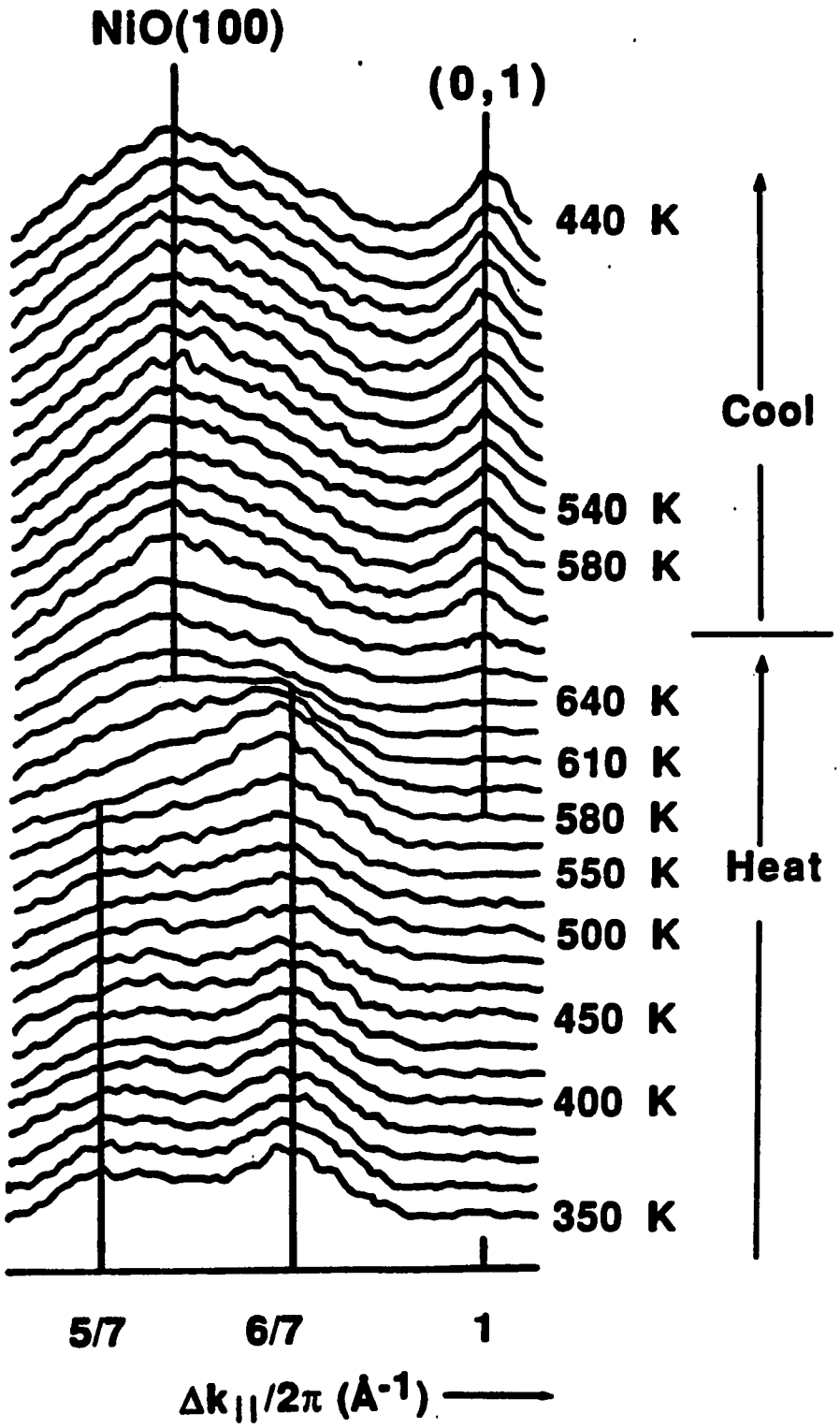
NiO(100)
(0,1)
440 K
Cool
540 K
580 K
640 K
610 K
580 K
550 K
Heat
500 K
450 K
400 K
350 K
5/7
6/7
1
Δk||/2π (Å-1)

intensity is shown in Fig. 12B. As the sample is heated, the intensity of the spot (almost zero at the outset) first reaches a weak minimum at 580 K, then grows. The (1/2,1/2) diffraction spot remains at zero intensity until a temperature of 560 K, then grows also, as shown in Fig. 12C. Panels D-F show the intensity variations of three seventh-order spots. The (0,5/7) spot first fades, then starts to intensify at 575 K, and finally fades again as the sample is heated. Meanwhile, the (0,6/7) spot intensity reaches a sharp maximum at 580 K. The (1/7,6/7) spot declines to zero in this same temperature range (560-590 K). These rather complex changes in seventh-order spot intensities are due, mainly, to changing contributions from the two types of (7x7) patterns that will be discussed in detail in Chapter 2. The intensities of the (0,1) and (1/2,1/2) spots increase in the cooling cycle, presumably because of the Debye-Waller effect. The general trends described here are very reproducible, although the relative magnitude of each intensity change depends markedly upon the temperature at which the sample was initially oxidized.

Again, these data show that gross, irreversible changes in surface structure take place above 500 K. The average temperature at which the c(2x2) appears is 560 $\pm$ 25 K, and the average temperature at which the (0,6/7) spot reaches maximum intensity is 580 $\pm$ 15 K, following adsorption at 300 to 400 K. These values are derived from a total of five similar experiments. In all cases, including Fig. 12, abrupt changes in the intensities of seventh-order spots occur shortly after the c(2x2) and (1x1) patterns emerge. The LEED patterns indicate that, as

the sample is heated, oxygen is lost and some of the metallic Ni(100) surface reappears. Figure 13, which shows profiles of two seventh-order spots during this thermal cycle, helps to clarify why the intensities of the seventh-order spots change as they do in Fig. 12D and E. In Fig. 13, the (0,5/7) and (0,6/7) spots are replaced by the broad diffraction feature which is the signature of NiO(100), at about 580 K. The latter feature is intermediate in position between the two seventh-order spots. As the sample is heated, the weak (0,5/7) feature decreases first, and then completely disappears at about 580 K. On the other hand there is a brief intensification of the (0,6/7) spot, which is most obvious between about 550 and 580 K, but then it, too, rather abruptly disappears as the NiO(100) feature comes to dominate. The brief rise in intensity which precedes disappearance of the (0,6/7) spot, obvious also in Fig. 12E, is very reproducible. This occurs <u>after</u> the (0,5/7) and (1/7,6/7) spots have started to fade, so it is not simply due to an improvement of the (7x7) structure from annealing, since then all (7x7) spots would intensify similarly. Nonetheless, it is clear from Fig. 13 (and from other data in our laboratory) that the point at which the (0,6/7) spot abruptly fades (the sharp maximum in Fig. 12D) is also the point at which the NiO(100) becomes identifiable in LEED. As noted above, the temperature at which this occurs is, on average, 580 ± 15 K. This occurs about 15 K after emergence of the c(2x2), and intensification of the (1x1) pattern. The conversion of (7x7) to NiO(100) is irreversible, since the changes described above remain in effect when the sample cools. In summary, NiO(100) and metallic Ni(100) develop at the expense of the

(7x7) structure, at about 580 K. The (7x7) structure plays a role in Fig. 12 exactly analogous to that of the ring structure in Fig. 10.

Finally, when the sample is heated after adsorption and oxidation, the ring structure never forms from the (7x7), nor vice versa. In short, heating does not bring about interconversion of these two structures. Rather, each converts directly to NiO(100) above 550 K.

Discussion

There are four main new results from this work. The first is the observation of the (7x7) LEED pattern, and its relationship to the LEED pattern of NiO. The second new result is the temperature-dependence of the oxide epitaxy on Ni(100). The third is the temperature-dependence of the oxidation threshold and oxide depth. The fourth concerns the structural changes which occur when the oxidized sample is heated in vacuum.

(7x7) Pattern. Even though oxidation of Ni(100) has been studied extensively with LEED and other structure-sensitive techniques, the (7x7) pattern has not been reported until the very recent work of Saiki et al. [33]. Results from this work, combined with theirs, show that this pattern can be formed reproducibly by oxidation of different Ni(100) crystals and in different laboratories. This is important, in view of the irreproducibility which has been suggested to result from sample history and treatment [9,24,42]. The question then arises, why has the (7x7) not been observed previously? This may be because the pattern is

quite faint, and is superposed on a large area of diffuse background. The large, diffuse background of the (7x7) (shown in Fig. 4D-E) lies in approximately the same area of reciprocal space as the NiO(100) spots, and without fairly precise measurements of spot profiles and spot positions it would be easy to mistake this background for the NiO(100) spots. In past experiments, visual observation has usually been the only means of measurement [e.g., 23, 29]. Also, it is our experience that the (7x7) is invisible at many beam voltages, which may contribute further to its omission by other authors. Therefore, we suggest that previous reports of NiO(100) formation in the temperature range 300 to 400 K and at pressures of 10^{-9} to 10^{-8} Torr [23,24,32] are in error.

The distinction between the (7x7) pattern and the NiO(100) pattern is shown most precisely by the profiles of Fig. 13, measured at a beam energy of 46 eV. At about 580 K in that experiment, the (7x7) disappears and the NiO(100) pattern emerges. Clearly, the NiO(100) spot is not at the same position as either of the nearest seventh-order spots, but rather falls between the (0,5/7) and (0,6/7) beams. On this point, we disagree with Saiki et al. [33], who say that the NiO(100) spot is nearly coincident with the (0,6/7) spot. Indeed, it should be nearly coincident: $\Delta k_{\parallel}/2\pi = 0.843$ Å^{-1} for NiO, using the bulk lattice parameters [43], whereas $\Delta k_{\parallel}/2\pi = 6/7 = 0.857$ Å^{-1} and $\Delta k_{\parallel}/2\pi = 5/7 = 0.714$ Å^{-1}. Instead, we find that the NiO feature is reproducibly farther from the (1,0) spot than it should be, at $k_{\parallel}/2\pi = 0.806 \pm 0.007$ Å^{-1}, for a beam energy of 46 eV. The mean and variance here are based upon five separate measurements. The mean value of $\Delta k_{\parallel}$ indicates that the NiO lattice is

expanded by 5% in the [010] direction. This contradicts other reports that LEED shows no difference from the bulk lattice constant of NiO [9], and that RHEED even shows a contraction of 2% in the [110] direction [24]. However, the position of the NiO(100) spot in k-space is also energy-dependent. The 5% contraction, based upon measurements at 46 eV, disappears at beam energies above 90 eV. Therefore, above 90 eV, our results agree with those of other authors [9,33]. This energy-dependence may reflect the different sample depths probed by electrons with different kinetic energies, the degree of lattice expansion then being a function of oxide depth.

Saiki et al. [33] postulate that the (7x7) structure is a strained form of NiO(100). The data (which will be presented in full length in chapter 2) from this study suggest that the situation may be more complex. It appears that there are two kinds of (7x7), or at least two different stages in its formation. These two structures, or stages, differ mainly in the relative intensities of various seventh-order spots. In this chapter, we are careful to draw only those conclusions which do not depend upon the subtle distinction between these two structures or stages. The details of our interpretation are left for Chapter 2 and 3.

Temperature-Dependence of Epitaxial Orientation. Figure 9 shows clearly that the epitaxial orientation of the oxide is a strong function of adsorption temperature. The ring pattern, which corresponds to NiO(111), reaches maximum intensity below room temperature, while the (7x7) pattern reaches maximum intensity between 300 and 400 K. Finally, true NiO(100) forms above 550 K. This temperature-dependence is a second

factor which has probably contributed to conflict in the literature over which form of the oxide develops. Many previous studies have been at adsorption temperatures around 300 K, or nominally at "room temperature." As we have shown, this is just the temperature where NiO(111) and the (7x7) structure "cross over", and a slight difference in adsorption temperature (by as little as 10-20 K) from the stated value can make a critical difference in the result.

This temperature dependence must carry information about the mechanism of oxidation of Ni surfaces. NiO(111) is favored kinetically, since it forms preferentially by oxidation at low temperatures. This is a surface consisting of layers of nickel or oxygen atoms, as shown in Fig. 14 [43], where the Ni layers are parallel to Ni(100). Fig. 15 shows the mechanism of the formation of Ni layers of (111) orientation of NiO. It is seen that nickel atoms in a Ni(100) layer only need to collectively move by rows (columns) in the x- (y-) axis, without changing the spacing between rows (columns). This results in the two equally possible domains of NiO(111) rotated 30° from each other. Therefore, the observed 12-spot ring pattern is superposed by two hexagonal patterns with 30° rotation from each other. The NiO(100) surface, however, is the more thermodynamically-stable form of the oxide on Ni(100), since it forms irreversibly when the sample is heated. (See, for instance, Fig. 13.) Indeed, theoretical calculations demonstrate that the (100) is the most thermodynamically stable surface of bulk NiO [44,45]. This is an oxide in which each layer is a mixture of nickel and oxygen atoms. (Again, see Fig. 14.)

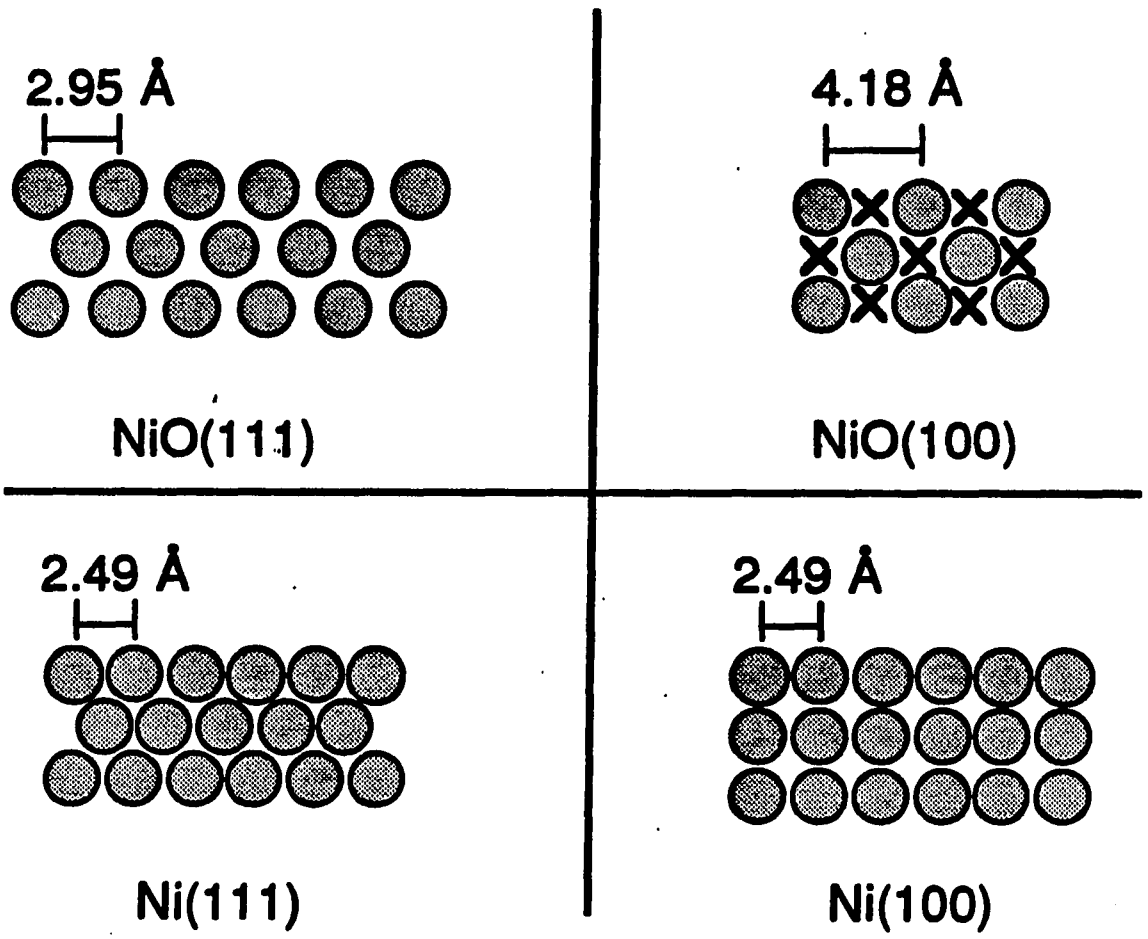

Figure 14. Representations of (111) and (100) planes of NiO and Ni, drawn to scale. The shaded circles represent Ni atoms, and the crosses indicate oxygen atoms. Note that NiO(111) may be either nickel- or oxygen-terminated; only the latter case is shown.

Figure 15. Schematic depiction of formation of two NiO(111) domains, rotated 30° from each other, from Ni(100).
(A) Ni(100) surface
(B) On the right, two equally possible domains of the (111) face of NiO. Domain 1 is resulted from the collective move of Ni rows in x-axis while keeping the space between rows unchanged and domain 2 is resulted from the collective move of Ni columns in y-axis while keeping the space between columns unchanged. Therefore, the nearest neighbor distance in the "reconstructed" (111) face is 2.8772 Å, as derived from geometrical calculation, as marked in the figure, rather than 2.9536 Å of the distance in regular NiO(111). Therefore, the observed 12-spot ring pattern may correspond to a 2.5% contracted NiO(111) epitaxy, which is diffcult to tell experimentally.

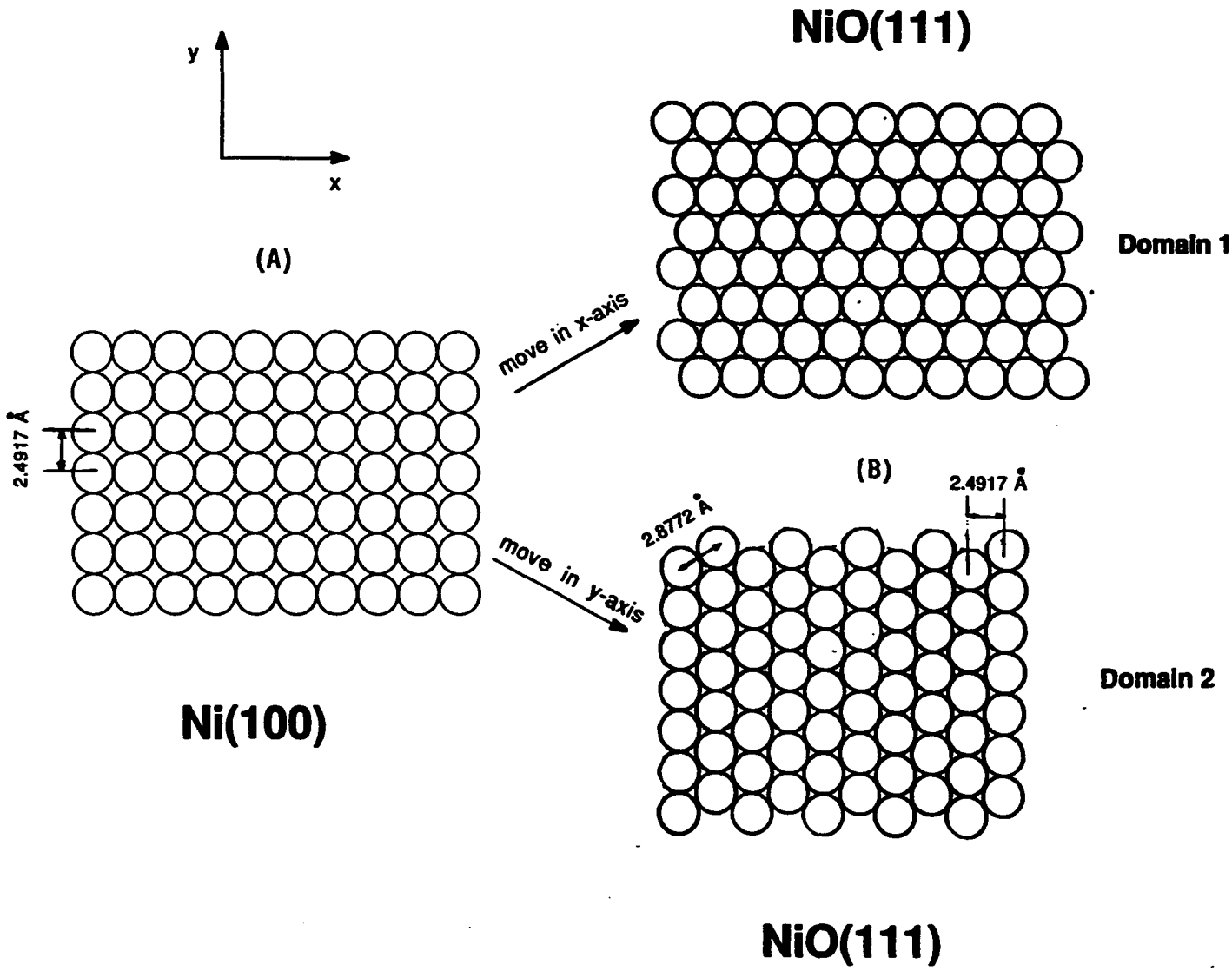
NiO(111)
y
x
(A)
Domain 1
move in x-axis
2.4917 Å
(B)
2.4917 Å
2.8772 Å
move in y-axis
Domain 2
Ni(100)
NiO(111)

We propose the following model. Layered NiO(111) forms when oxygen "slips between" layers of metallic nickel, accompanied by rearrangement of the nickel atoms within these layers. During this collective motion, most of the Ni-Ni bonds within the metallic layers need not break completely as the oxide forms; the integrity of each layer of Ni atoms can remain somewhat intact as the process occurs. The activation barrier associated with this process is perhaps low. The density of Ni within each layer must decrease by 17% as the metal transforms to the oxide, but perhaps this density change is accomplished by formation of domain boundaries and steps at the surface. By contrast, the (100) face of NiO can form only if Ni atoms move into adjacent layers, forming sheets of Ni atoms non-parallel to the metal substrate. This may lead to a higher activation barrier for formation of the (100) oxide than for the (111) oxide. Thus, the (111) oxide is kinetically favored.

This model is supported by results of other authors. The ion shadowing and blocking measurements of Frenken et al. [10,11], show that adsorption of oxygen on Ni(100) induces outward relaxation of the topmost Ni layer as shown in Fig. 16, accompanied by a substantial weakening of the force constants between first- and second-layer Ni atoms. Although the clean surface spacing is contracted by 0.06 Å, relative to the bulk interlayer separation (1.76 Å), the p(2x2) oxygen layer induces an expansion by 0.04 Å, and the c(2x2) leads to an even larger expansion of 0.09 Å. The separation between adjacent Ni planes in NiO(111) is 2.41 Å, or 0.65 Å larger than the bulk value. Clearly, the outward expansion induced by simple chemisorption is much smaller than that required for

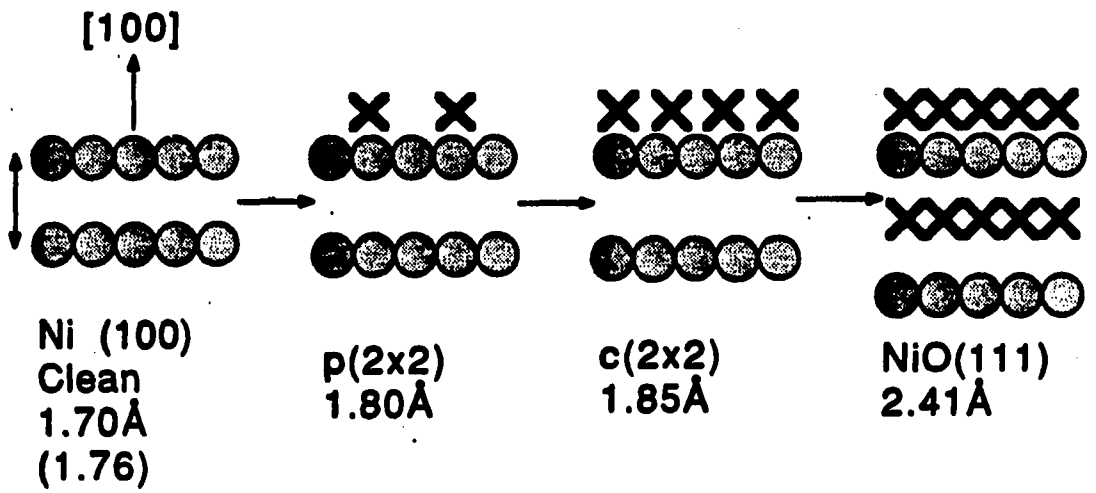

Figure 16. Schematic depiction of mechanism by which NiO(111) may form from Ni(100). The shaded circles represent Ni atoms and crosses represent oxygen atoms. Adsorption sites of the latter are not depicted literally in this sketch. Interplanar Ni-Ni spacings, drawn to scale, are taken from Refs. 10, 12, and 42. The value in parentheses is the interplanar spacing in bulk Ni.

oxidation, but it is nonetheless a step in the direction leading to NiO(111). In fact, Frenken, van der Veen, and coworkers speculate that the chemisorption-induced expansion might be a necessary precursor to surface oxidation [10,11]. The scenario that can be proposed here, in light of their results, is illustrated in Fig. 16.

It is also useful to examine the data of Christensen et al. [27], who describe the effect of oxidation temperature on oxide epitaxy between 290 and 770 K, starting from metallic Ni(111). They find that NiO(111) forms exclusively up to adsorption temperatures of 470 K, 160 K higher than the maximum temperature at which we observe NiO(111) formation on Ni(100). Presumably, this higher temperature reflects greater stability of NiO(111) on Ni(111) than on Ni(100). This can be rationalized in terms of the better symmetry match between the NiO(111) overlayer and the Ni(111) substrate (both hexagonal lattices), relative to the Ni(100) substrate (a square lattice). Christensen et al. also find that NiO(100) tends to form irreversibly at temperatures above 470 K, indicating that this is the thermodynamically-favored form of the oxide also on Ni(111) [27]. Thus, the results of Christensen et al. parallel ours. In both cases, NiO(111) is the kinetically-favored epitaxial orientation, whereas NiO(100) is thermodynamically-favored.

This comparison between the metallic Ni(111) and (100) faces, as starting points for oxidation, is informative. Christensen et al. suggested that the greater ease of formation of NiO(111), relative to NiO(100), is due entirely to the better symmetry match between oxide and metal, as illustrated in Fig. 14. However, our results, starting from

the (100) face of the metal, are analogous to theirs. This suggests that something besides symmetry match with the underlying metal makes NiO(111) kinetically-favored over NiO(100). We propose that this factor is the energy barrier to formation of a layered oxide epitaxy where Ni layers are still parallel to Ni(100), relative to the energy barrier for an oxide epitaxy that the Ni sheets are not parallel to Ni(100)(Fig. 14).

Temperature-Dependence of Oxidation Threshold and Final Oxide Depth

At temperatures of 80 to 400 K, we find good agreement between the oxidation threshold measured with AES, the very first appearance of the LEED pattern associated with the oxide, and the maximum intensity of the c(2x2). This is true, regardless of whether the (7x7), the ring pattern, or some mixture thereof represents the epitaxial orientation. Previously, Holloway and Hudson reported that the first appearance of the oxide-related LEED pattern (as determined by visual observation) lags considerably behind the maximum in c(2x2) intensity [23], and also well behind the oxidation threshold measured with AES [9,23]. This led to some discussion in the literature concerning the relative sensitivities of AES and LEED, with the conclusion that LEED suffers in the comparison due to insensitivity toward very small crystallites [9]. Because RHEED observations indicated that the oxide patterns emerge at much lower coverage than did the LEED observations, this led to the secondary conclusion that LEED is less sensitive than RHEED, at least in this system [9,24]. These previous conclusions point to the danger of relying simply upon visual observation of LEED pattern intensities as a function of exposure, as Holloway and Hudson did in their original measurements

[23]. Our data show that when quantitative measurements of LEED spot intensities are made, there is no significant difference between AES and LEED, nor (presumably) between LEED and RHEED, in measuring the onset of oxidation on Ni(100).

The increase in oxidation threshold with increasing temperature, shown in Fig. 6, has been observed by others at 300 K and above [9,23-26, 29,31]. This temperature-dependence can be interpreted in one of two ways: either, oxide growth depends upon diffusion of the (molecular) mobile precursor, whose lifetime diminishes as temperature increases [9, 23,24]; or, the oxide nucleates preferentially at defects in the adsorbed overlayer, which are less plentiful at high temperature [9,21,29]. Our data extend the range over which this threshold has been measured, to temperatures below 300 K. We observe a remnant of the first plateau in oxygen uptake, measured with AES, even as low as 80 K (see Fig. 3). Two previous, analogous measurements with XPS at 77 K failed to reveal this feature [26,29]. Future attempts to model the oxidation kinetics of Ni(100) may benefit from the broader and more continuous range of useful data presented in here.

The depth of the oxide represented by the (7x7) is approximately the same as that represented by the ring structure. This statement is based upon data such as those of Fig. 3, which show that the final intensity of the oxygen Auger signal is essentially independent of adsorption temperature, between 80 and 400 K. Also, other authors, using other techniques, have reported that there is no significant temperature-dependence in final oxide thickness between 80 and 400 K [e.g., 23,

26,29]. Most authors argue that this oxide is 2 to 3 layers deep [9,23,24,26], although recent measurements by Saiki et al. support a thickness of about four layers [33]. We do not use our data to derive a value for the thickness of the oxide, but only to support the interpretation that the thickness of the oxide is temperature-independent, and therefore epitaxy-independent, in this temperature regime.

Structural Changes Induced by Heating in Vacuum. We have made a detailed study of the structural changes which occur when a Ni(100) sample is oxidized at relatively low temperature ($T \leq 400$ K), then heated in vacuum. The results can be summarized as follows. In the range 500-550 K, oxygen atoms at and near the oxidized surface begin to move. Part of the surface oxide converts back to metallic nickel, covered with a chemisorbed c(2x2) layer, and part converts to NiO(100). The former event precedes the latter slightly in temperature. These events occur, independent of whether the initial oxide is the "ring" structure or the (7x7)-like structure. Some of the oxygen may also disappear via deep bulk dissolution, but we have no way of measuring the extent to which this takes place. Other authors report that the oxide which grows by adsorption at temperatures above 500 K is much thicker than that which forms at lower temperatures [e.g., 9,25,28], and so it is probable that the (100) crystallites which form upon heating above 500 K in our experiments are also deeper than the parent oxide. In fact, it may be that the "true" (100) orientation of the oxide is not stable unless it achieves a depth greater than that which is accessible during low-

temperature, low-pressure oxidation. These two irreversible events--conversion to a metallic nickel surface covered by chemisorbed oxygen, and nearly-simultaneous conversion to deeper oxide crystallites--suggest that the original, oxide "blanket" effectively disproportionates when it is heated above 500 K. There is one other (brief) report on this topic in the literature. Using RHEED, Mitchell et al. [24] observed that the diffraction pattern from NiO(111) is stable up to 600-625 K, where it disappears and the NiO(100) pattern intensifies. This is higher than the temperature at which the NiO(111) pattern disappears in our measurements, ca. 500-550 K. (See Fig. 8.) The difference may be due to different techniques used for the low-temperature oxidation. Specifically, Mitchell et al. [24] tend to use much higher oxygen pressures and higher oxidation temperatures than we do.

Summary

This chapter describes the temperature- and exposure-dependent development of various LEED patterns observed during oxidation of Ni(100). Diffraction spot intensities are measured quantitatively and continuously, allowing unambiguous correlation of various surface processes. Auger electron spectroscopy provides an additional measure of the oxidation onset during adsorption, and the final relative thickness of the oxide. Our major results can be summarized as follows.

1. A (7x7)-like pattern forms reproducibly upon oxidation of Ni(100).

Although the (7x7) pattern is clearly distinguishable from the NiO(100) pattern under certain experimental conditions, it may have been mistaken by other authors for epitaxial NiO(100).

2. Between 80 and 400 K, the development of LEED patterns associated with NiO is very temperature-dependent. The formation of NiO(111) is favored by adsorption temperatures below 300 K, whereas the (7x7)-like structure is favored by adsorption temperatures of 300 to 400 K. Room temperature is a "crossover" point between these two forms of the oxide, which may have also contributed to previous discrepancies in the literature. We suggest that the low-temperature epitaxy is kinetically favored because it consists of nickel and oxygen sheets parallel to the substrate.

3. In the temperature range 80 to 400 K, AES and LEED measurements of the oxidation threshold are in good agreement, independent of the oxide epitaxy. The threshold measured with these techniques also coincides with the maximum in c(2x2) intensity. The final depth of the oxide exhibits no measurable dependence on oxide epitaxy, in this temperature range.

4. When the sample is heated in vacuum after adsorption, massive rearrangements take place above 500 K. Some of the nickel reverts to metallic nickel covered by a c(2x2) oxygen overlayer, and some forms NiO crystallites which are probably deeper than the oxide skin formed at lower temperature. Effectively, the surface disproportionates into a less-oxygen-rich phase and a more-oxygen-rich phase. This is true, independent of the epitaxial orientation of the initial oxide overlayer.

CHAPTER 2: POSSIBLE MODELS OF THE (7X7) STRUCTURE

General Background Information about the (7x7)

A (7x7) pattern that forms at temperatures of 300-400 K has been reported in the previous chapter. The (7x7) pattern is different from the patterns of two known oxide epitaxies, NiO(111) and NiO(100). The pattern of NiO(111) is characterized by a 12-spot "ring", whereas the NiO(100) pattern [which is obtained after annealing the adsorbed surface above 600 K] consists of broad and diffuse spots near the Ni(100) integral spots, as shown in Fig. 4C and F of Chapter 1. The (7x7) structure has been overlooked by other workers for many years. Very recently, Saiki et al. reported a (7x7), which they interpreted to be a strained NiO(100) structure [33]. The pattern they reported is presumably the same (7x7) pattern as ours, but their observations are restricted to the structure formed at room temperature only. The authors speculate that the (7x7) pattern is due to the 1.5% contraction of the NiO lattice. Refer to Fig. 17 for the observed (7x7) pattern and its real space model. This speculation is based on the fact that there is a numerical match between the lattice constants of Ni(3.5238Å) and NiO(4.177Å) crystals, i.e., every six NiO unit cells can be lain on seven Ni unit cells, if the NiO lattice is contracted (strained) by 1.5% from its normal lattice structure:

$$\frac{(3.5238\ \text{Å} \times 7 - 4.177\ \text{Å} \times 6)}{4.177\ \text{Å}} = -1.5\%$$

However, there are some types of information which previous authors did not consider, which lend additional insight into the validity of this and other models for the p(7x7) structure. This chapter will concentrate on the presentation and discussion of that additional information. First, quantitative measurements of the integrated spot intensity and spot profiles are presented here. Second, the (7x7) structure is monitored at varied adsorption temperatures (rather than only room temperature), which reveals some detailed features that would not be available otherwise. Third, Saiki et al. attributed the observed 7th order spots to the closer lattice match at or near every 7th substrate unit cell, or to the regions of near registry between the strained oxide overlayer and the substrate Ni(100). Refer to Fig. 17E for "the lighter colored-square positions". Figures 17C and D are the real space arrays of Ni(100) and NiO(100) with 1.5% contraction. Figure 17E is resulted from overlaying Fig. 17C and D. The absence of the 7th order spots, except a few spots near substrate integral spots, was attributed to the high mismatch in some regions between the strained NiO(100) layer and the Ni(100) substrate. Refer to Fig. 17E for the "darker color regions". If this model is correct, then in Fig. 17A the same kind of 7th order split should be equally observable at (0,0) beam. However, the authors did not show splitted spots at (0,0) in the schematic drawing of the observed pattern in Fig. 17B. This is clearly conflicting with each other between the observed (7x7) pattern in Figs. 17A, B and the real space model of

Figure 17. Shows the (7x7) pattern observed from LEED and the corresponding real space structure. After Saiki et al [33].
(A) LEED spot pattern observed for ambient-temperature saturated oxide on Ni(001) at an incident energy of 64 eV. (The specimen holder obscures some spots from left to right across the image.) At right the positions and suggested origins of the several structures are indicated.
(B) Same as (A), but after a light anneal to approximately 523 K over about 10 min.
(C) The array of Ni atoms on the surface of Ni(001), with various directions noted.
(D) The Ni atoms in the proposed superlattice of NiO(001) with a $^1/_6$ = 16.7% lattice constant expansion with respect to the Ni(001).
(E) An overlay of the two structures in (C) and (D) indicating the nature of the commensurate superlattice formed, as well as regions of both good registry (lighter color) and high mismatch and/or strain (darker color).

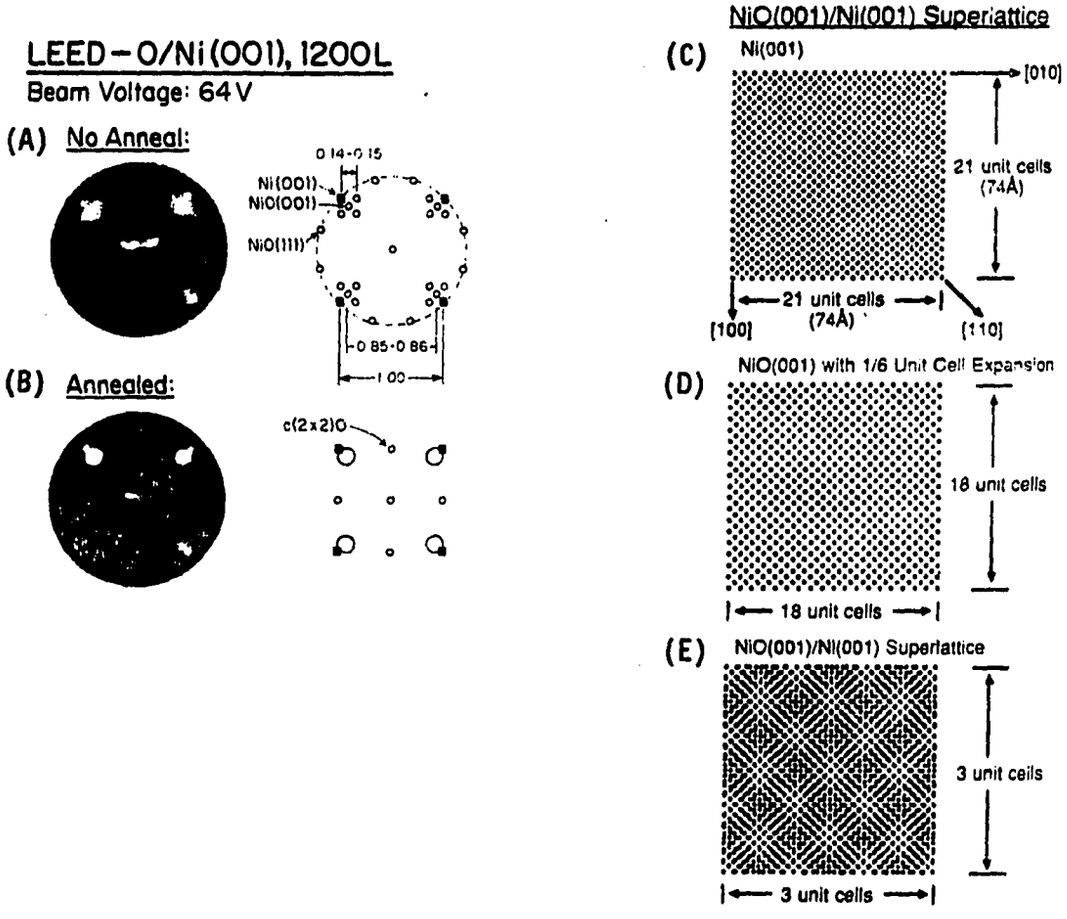
LEED – O/Ni(001), 1200L
Beam Voltage: 64 V
(A) No Anneal:
0.14-0.15
Ni(001)
NiO(001)
NiO(111)
0.85-0.86
1.00
(B) Annealed:
c(2x2)O
NiO(001)/Ni(001) Superlattice
(C)
Ni(001)
[010]
21 unit cells
(74Å)
21 unit cells
(74Å)
[100]
[110]
NiO(001) with 1/6 Unit Cell Expansion
(D)
18 unit cells
18 unit cells
(E)
NiO(001)/Ni(001) Superlattice
3 unit cells
3 unit cells

17E. The contradictions of this model to their own experimental observations, especially, to our quantitative measurements of the (7x7) pattern in the broader temperature range during adsorption and annealing process, strongly suggest that further and better understanding of the (7x7) structure is necessary.

We find that the (7x7) structure is far more complex than what they have reported. First of all, the (7x7) pattern obtained at different adsorption temperatures are slightly different. Besides the pattern they reported, with 4 fractional 7th order spots around the integral spot of Ni(100), as shown in Fig. 18B, we also see another pattern with 8 fractional 7th order spots around integral spots of Ni(100), as shown in Fig. 18A, although the ($\pm$1/7,5/7) and ($\pm$1/7,1) spots are much less intense than other spots. Refer to the LEED photos taken for the (7x7) patterns obtained at adsorption temperatures of 325 K, 350 K and 375 K in Figure 19A, B and C. Second, there are differences in relative intensities of various 7th order spots, which are clearly monitored by measuring the spots profiles as the structure grows during constant temperature adsorption. Third, when the adsorbed surface is heated, the intensity changes of various fractional spots are rather peculiar, such as those shown in Fig. 12, which are not mentioned, presumably not checked under these varied adsorption and annealing conditions, in Saiki's report.

To extend the discussion on the (7x7) structure, more data like those shown in Figs. 8, 12 and 13 will be presented. Several possible models will be compared: the multiple scattering model, the overlayer

modulation model and a model with highly correlated anti-phase walls within the (7x7) unit mesh (referred to as anti-phase wall model from now on). Preference is given to the anti-phase wall model, which not only quantitatively simulates the intensity of various 7th order spots, but also predicts there should be no split spots at (0,0). Note both the spot profiles and the integrated spot intensities presented here have been subtracted from a constant background. In the case of spot profiles, a minimum intensity in the profile data array of profile length plus additional 7 pixels at each end is taken for the constant background to be subtracted from. In the case of integrated intensity, intensities of a 7 pixel long additional area at each end are obtained and averaged as the constant background.

LEED Results for the (7x7) Pattern

Adsorption at fixed temperatures

Some of the data concerning the (7x7) LEED pattern have already been presented in Chapter 1, where we concluded that the NiO(111) structure is the low temperature (150-300 K) epitaxy and the (7x7) pattern forms at temperatures around 300-400 K. The pattern is most observable if adsorption is done at ~350 K. Patterns formed at the vicinity of above and below 350 K are slightly different, as shown in the schematic drawing of Fig. 18A and B, they are perhaps from two stages of the formation of (7x7). In this chapter, to support our argument of the observation of

Figure 18. Schematics of the two kinds of (7x7) patterns observed.
(A) First stage (7x7) pattern, where the relative intensities are noted by spot blackness. ($\pm$1/7,5/7) and ($\pm$1/7,1) are weakest in intensity among the spots shown here.
(B) Second stage (7x7) pattern, where the 4 fractional spots around (0,6/7) are about equally intense.

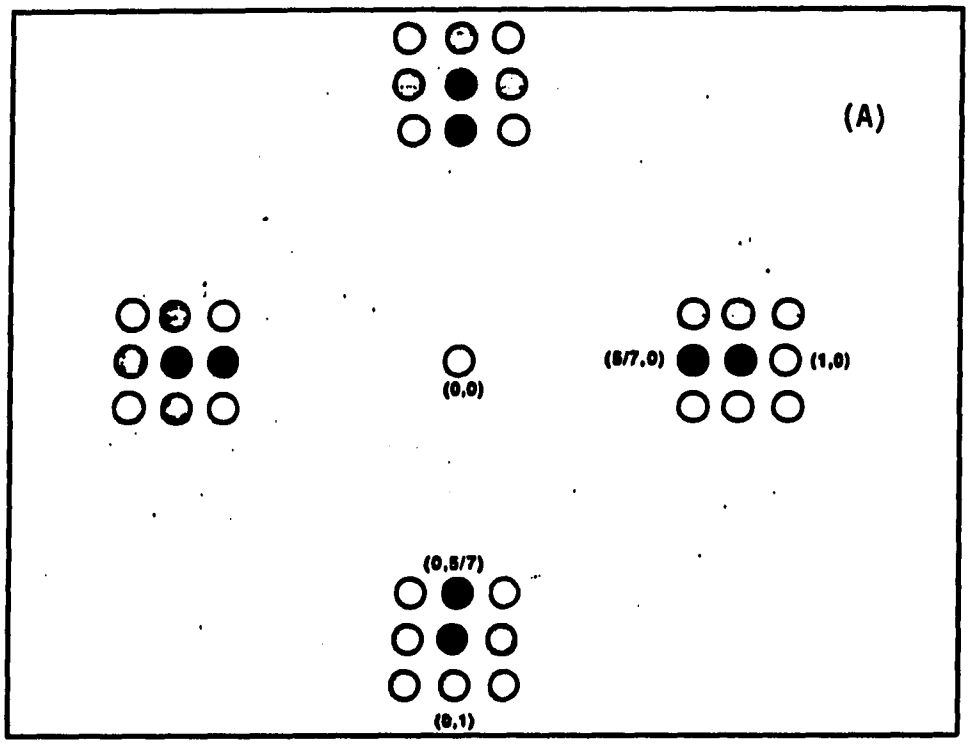
(A)
(0,0)
(5/7,0)
(1,0)
(0,5/7)
(0,1)

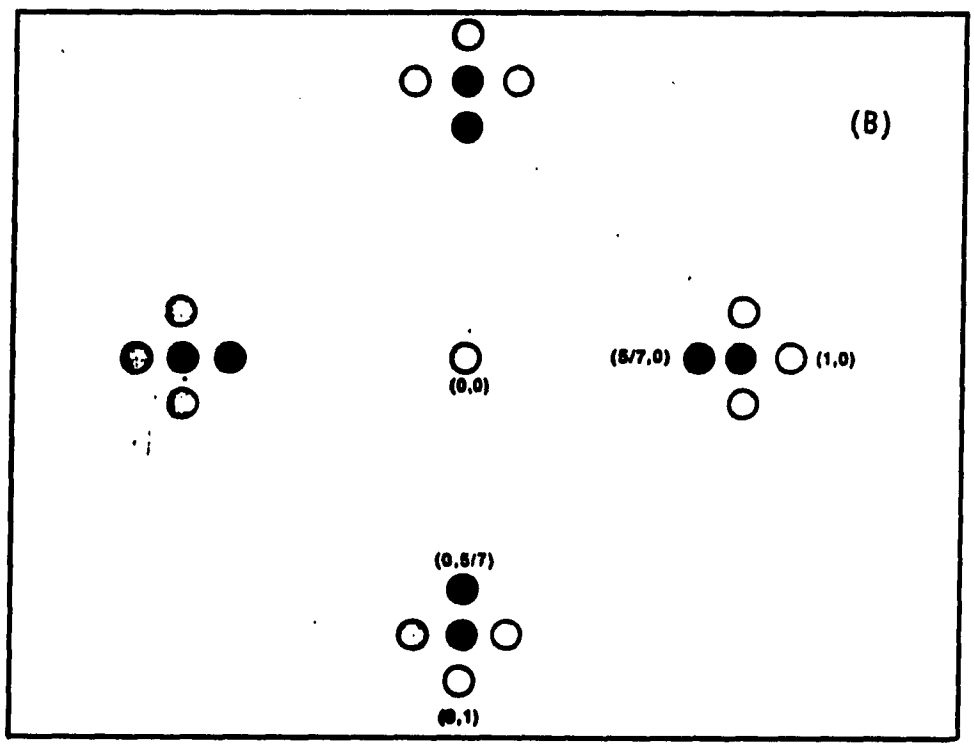
(B)
(0,0)
(5/7,0)
(1,0)
(0,5/7)
(0,1)

Figure 19. LEED photos of (7x7) pattern obtained by adsorption at different temperatures. Integral spots (1,0) and (-1,0) are indicated by arrows.

(a) Obtained after adsorption at 325 K with 5.5×10^{-8} torr for 368 L, photo taken at 58 eV beam energy and 300 K.

(b) Obtained after adsorption at 350 K with 5.5×10^{-8} torr for 400 L, photo taken at 65 eV beam energy and 80 K.

(c) Obtained after adsorption at 375 K with 6×10^{-8} torr for 527 L, photo taken at 50 eV beam energy and 300 K.

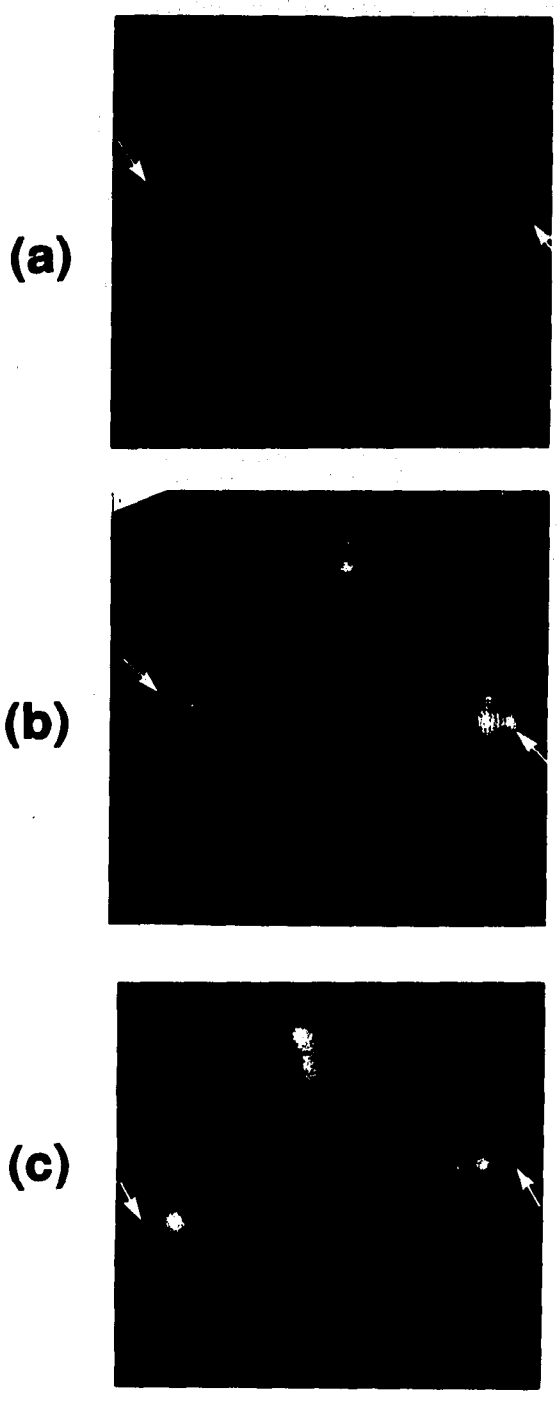
(a)
(b)
(c)

(7x7) structures we can further quantitatively show the growth profiles of 7th order spots during adsorption in Figure 20A, B, C and D, where oxygen is adsorbed at 325 K, 350 K, 375 K and 400 K respectively. Two profiles crossing the (0,6/7) spot, one along (0,5/7), (0,6/7) and (0,1), and the other along (-1/7,6/7), (0,6/7) and (1/7,6/7), are taken simultaneously in each case. Also the integrated intensities of (0,6/7) and (0,5/7) during the same adsorption processes are measured concurrently, as shown in Figure 21. But in order to see the trend clearly in the temperature range of 300-400 K, the integrated intensities are measured from 310 to 400 K at five different adsorption temperatures. Figure 20A and B clearly show that the spot (0,5/7) is more intense than that of (0,6/7), especially in B, where the 7th order spots are well-developed and resolved. On the other hand, in Fig. 20C and D, (0,6/7) spot become the more intense spot, relative to (0,5/7). These two kinds of spot profiles are evidence that suggest there are two types, or let us call them "two stages of the (7x7) structure" as in Chapter 1. Although Figure 21 shows that the (0,5/7) spot is about as intense as the (0,6/7) spot, due to the constant background subtraction, if adsorption is done at a temperature of 300-350 K, however, the intensity of (0,6/7) spots is increasingly higher than that of (0,5/7) if oxygen is adsorbed at 350-400 K temperature range. These results are at least reproduced twice at each adsorption temperature. This is another evidence that suggests as adsorption temperature goes from below 350 K to 400 K, a (7x7) pattern with stronger (0,6/7) spot is forming. Noticeably, in either cases the 7th order spots overlap with a broad and diffuse background which was

Figure 20. 7th order spots growth profiles during oxygen adsorption.
(A) Adsorption at 325 K with 5.5×10^{-8} torr pressure, beam energy is 46 eV.
(B) Adsorption at 350 K with 5.5×10^{-8} torr pressure, beam energy is 46 eV.
(C) Adsorption at 375 K with 6.0×10^{-8} torr pressure, beam energy is 46 eV.
(D) Adsorption at 400 K with 9.0×10^{-8} torr pressure, beam energy is 46 eV.

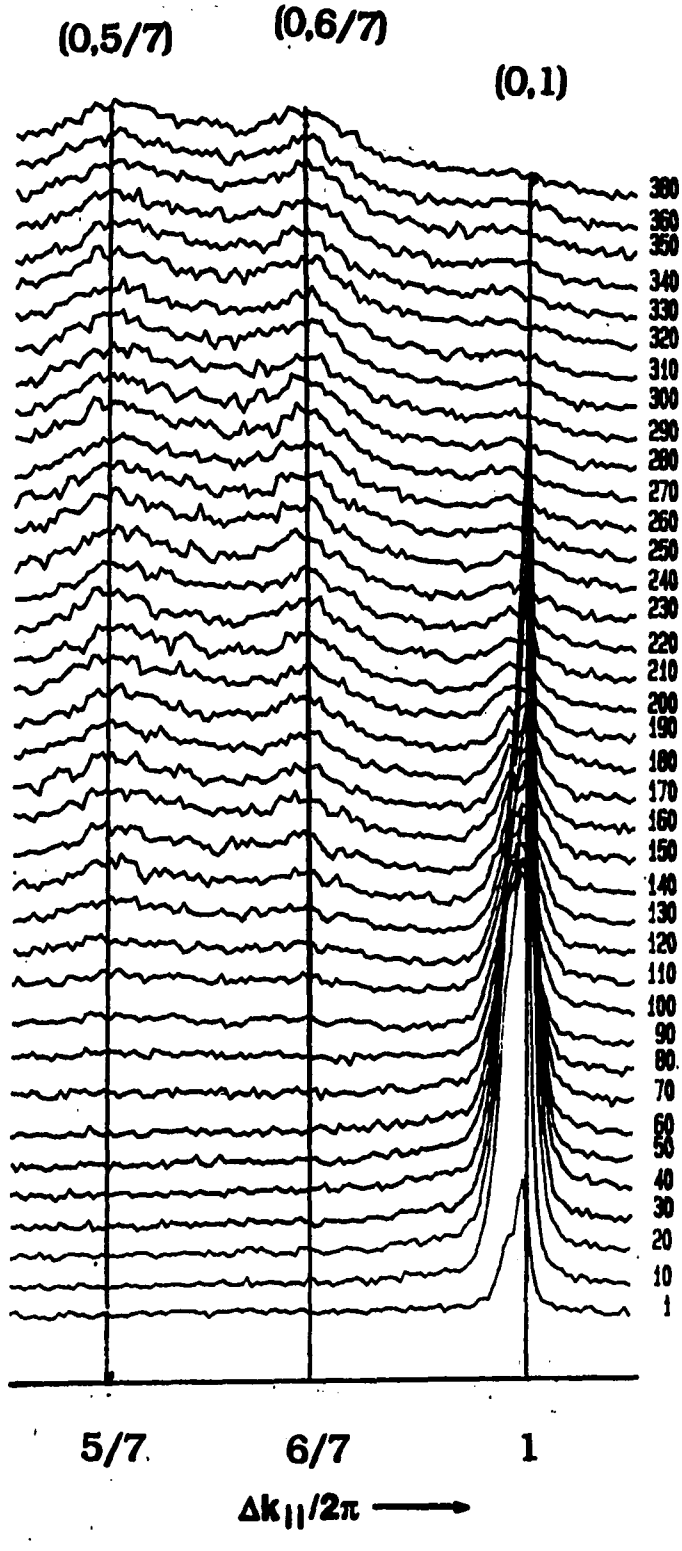
(0,5/7)
(0,6/7)
(0,1)
(A) Ta = 325 K
Exposure, L
-321 L
-275 L
-229 L
-183 L
-138 L
-92 L
-46 L
5/7
6/7
1
Δk||/2π

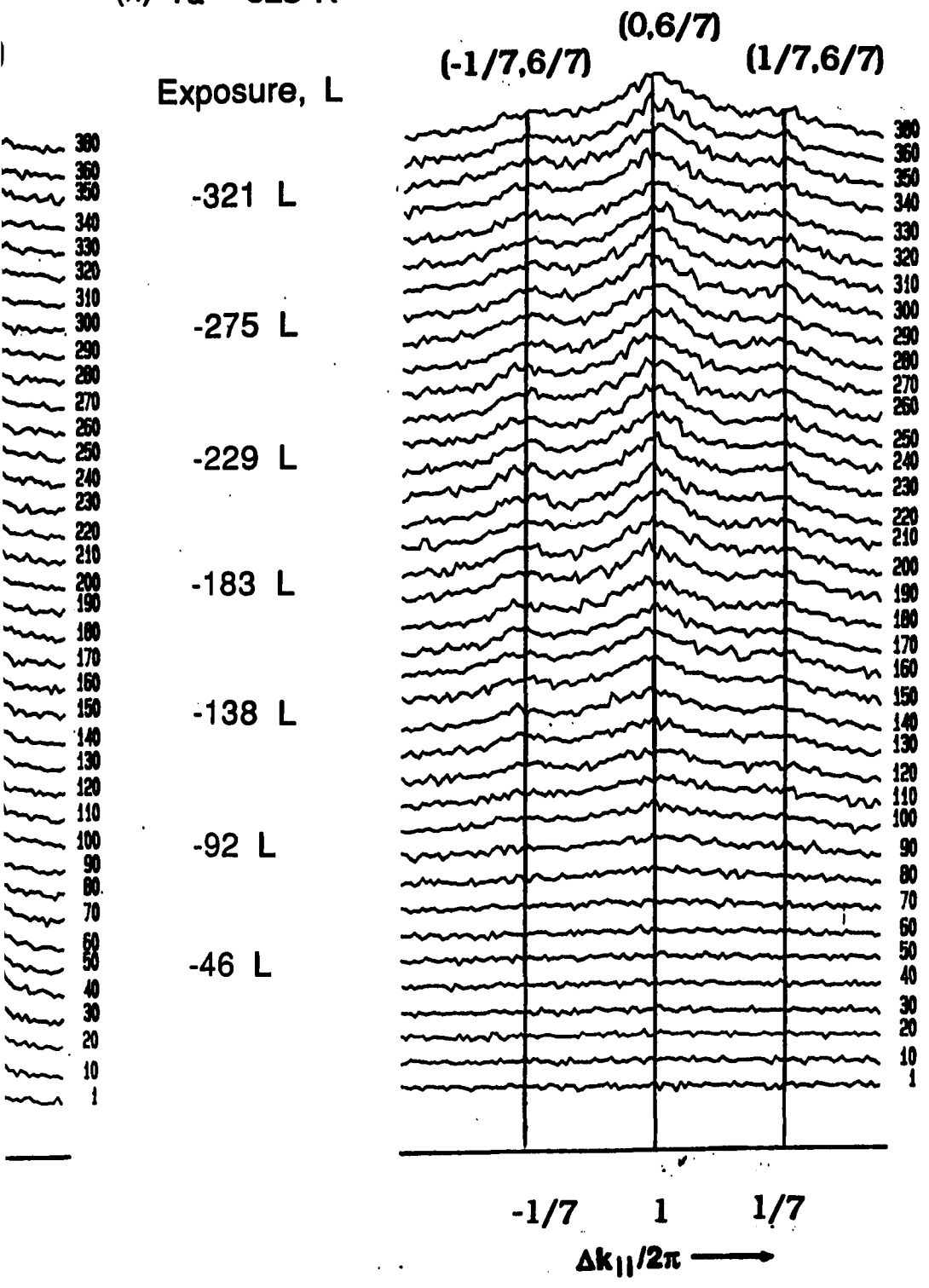
(A) Ta = 325 K
(0,6/7)
(-1/7,6/7)
(1/7,6/7)
Exposure, L
-321 L
-275 L
-229 L
-183 L
-138 L
-92 L
-46 L
-1/7
1
1/7
Δk||/2π

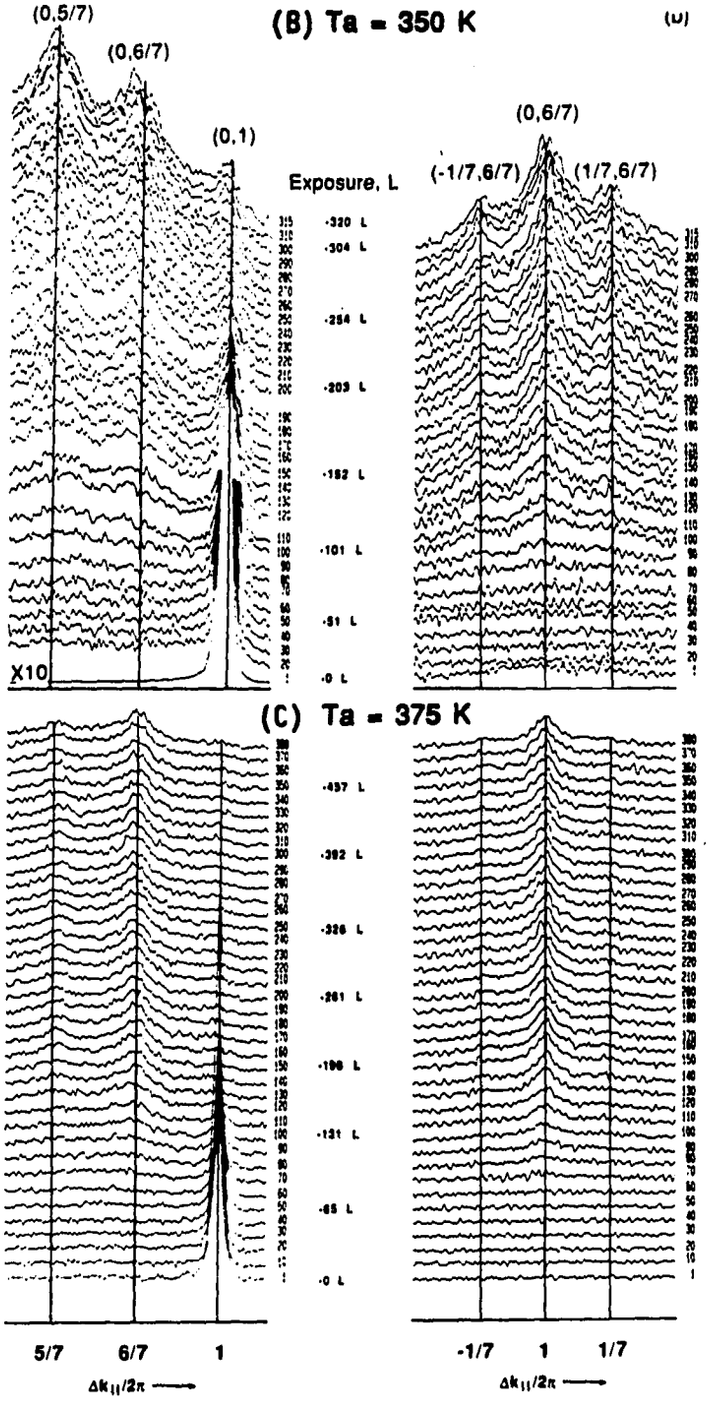

Figure 20 (Continued)

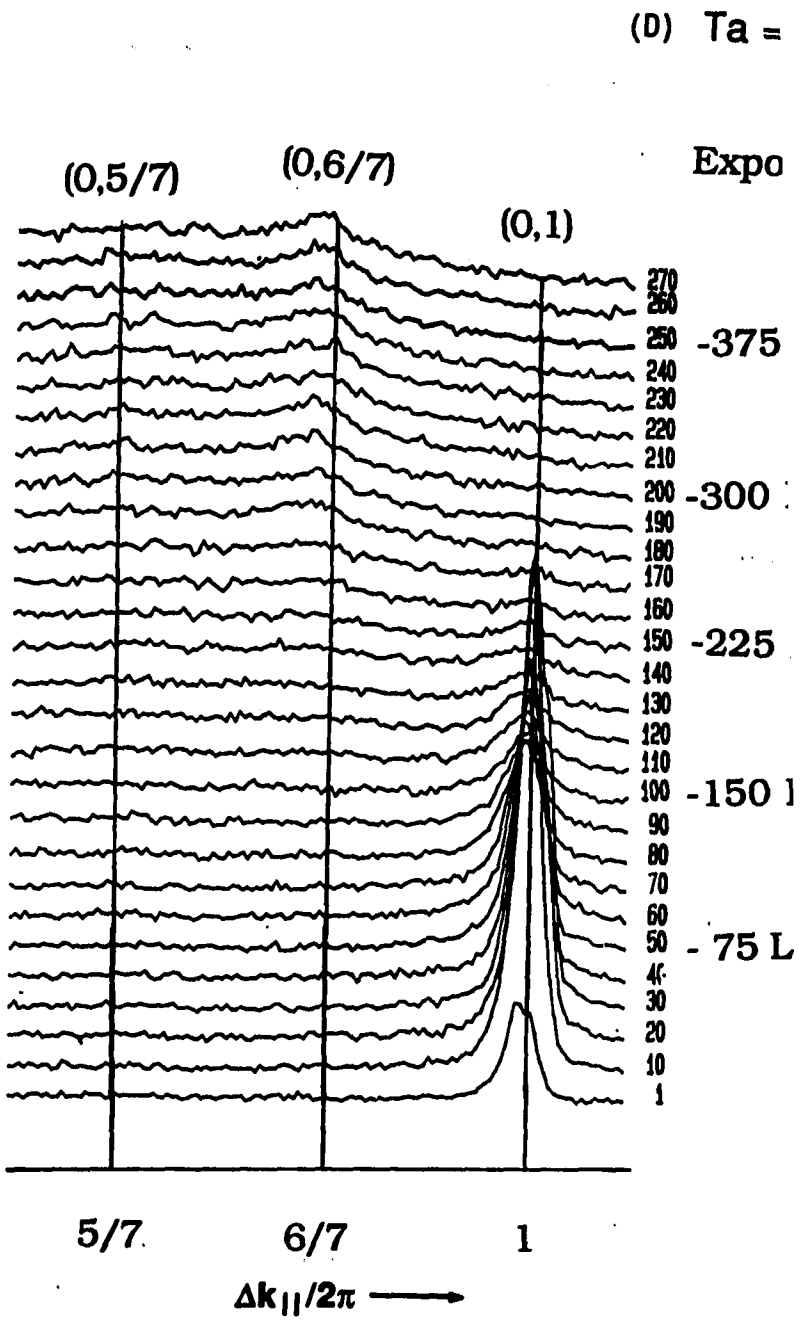

Figure 20 (Continued)

(D) Ta = 400 K

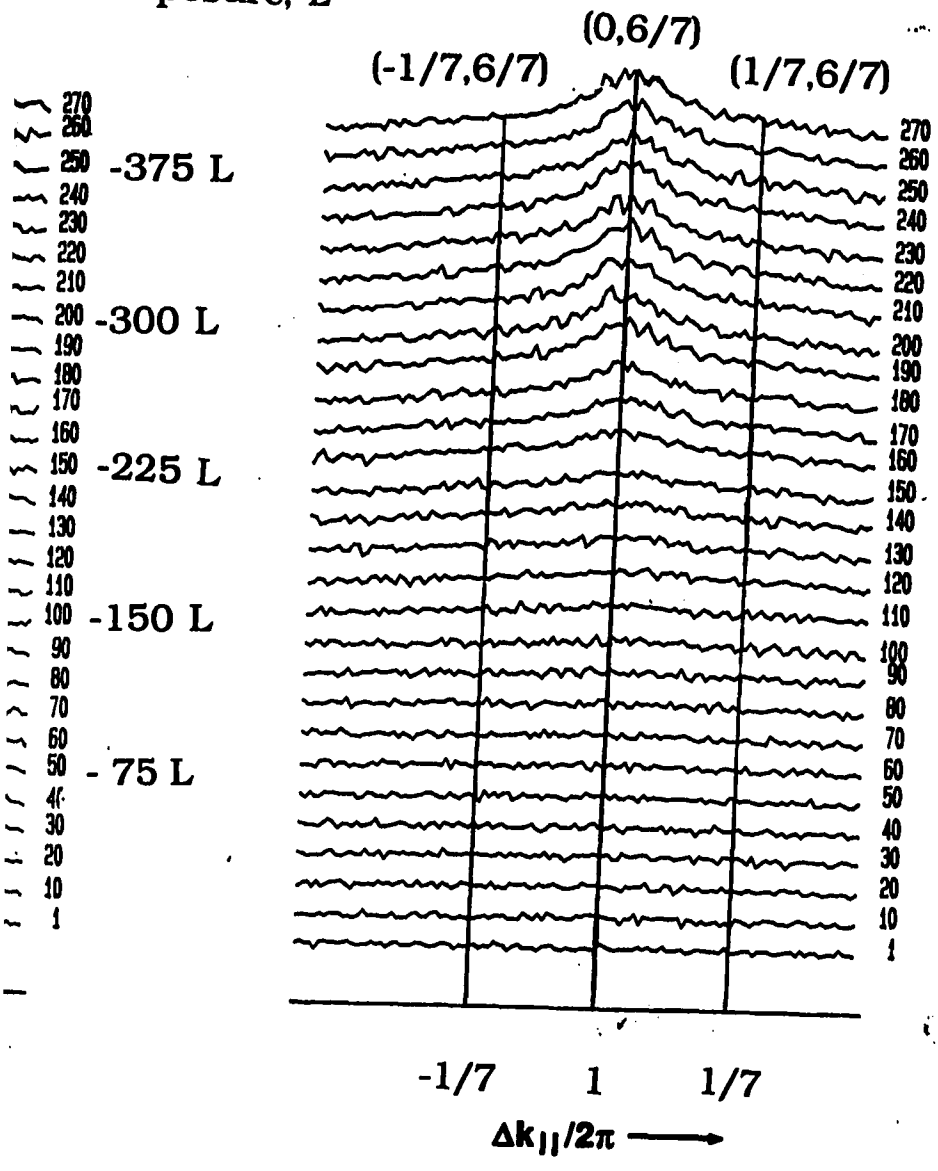

argued, by others, as owing to the coexistence of small clusters of NiO(100) domains when (7x7) structure develops [46]. It is observable in the growth profiles of 7th order spots in Fig. 19, this high background is more centered on (0,6/7) for the adsorption at 400 K and shifted toward (0,5/7) for adsorption at 350 K. The possible cause of the high background will be discussed later in this chapter.

Annealing in vacuum

The changes in the integrated intensities and spot profiles of 7th order spots during annealing have already been partly shown in Figure 12 and 13, and discussed in Chapter 1. Here, more data, measured at different conditions, are presented so that detailed discussion focusing on the (7x7) structure can follow. In Fig. 22 data similar to those in Fig. 12, from experiments where oxygen were adsorbed at two substrate temperatures 350 K and 400 K, are shown. In both Figures 22A and B, there is a noticeable common trend in the intensity change of (0,5/7) and (0,6/7) spots. We can discuss this trend according to the divided temperature regions α and β. In region α, (0,6/7) spot intensity increases, and (0,5/7) intensity decreases. In region β, (0,6/7) intensity decreases and (0,5/7) spot intensity increases, although the magnitude of intensities are different in Figs. 22A and B due to the difference in adsorption temperatures, adsorption at 350 K gives the more intense and better resolved (7x7) pattern. Also, each region in Fig. 22B slightly lags ~20 K behind that of Figure 22A. For the specific

Figure 21. Integrated intensity of (0,6/7) and (0,5/7) during oxygen adsorption at different substrate temperatures.

(A) Adsorption at 310 K with $5x10^{-8}$ torr pressure, beam energy is 46 eV.

(B) Adsorption at 325 K with $5.5x10^{-8}$ torr pressure, beam energy is 46 eV.

(C) Adsorption at 350 K with $5.5x10^{-8}$ torr pressure, beam energy is 46 eV.

(D) Adsorption at 375 K with $5x10^{-8}$ torr pressure, beam energy is 46 eV.

(E) Adsorption at 400 K with $9x10^{-8}$ torr pressure, beam energy is 46 eV.

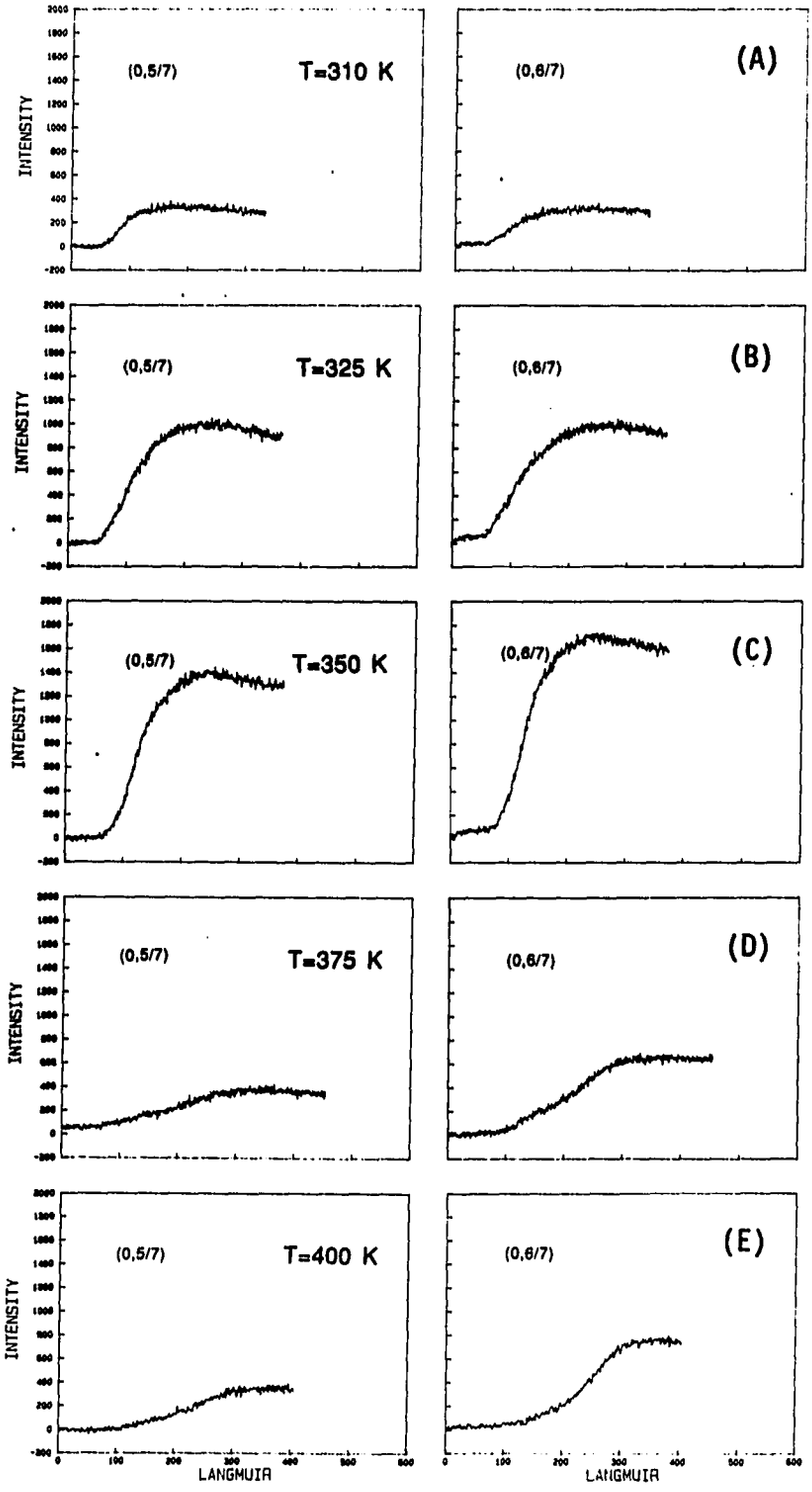
(0,5/7)
T=310 K
(0,6/7)
(A)
INTENSITY
(0,5/7)
T=325 K
(0,6/7)
(B)
INTENSITY
(0,5/7)
T=350 K
(0,6/7)
(C)
INTENSITY
(0,5/7)
T=375 K
(0,6/7)
(D)
INTENSITY
(0,5/7)
T=400 K
(0,6/7)
(E)
INTENSITY
LANGMUIR
LANGMUIR

experiment in Fig. 22A, region α ranges from 500 K to 570 K, and region β from 570 to 630 K, whereas, in Fig. 22B region α ranges from 520 K to 585 K, and region β from 585 K to 650 K. These differences in transition temperatures between Figures 22A and B are not significant. They are within the experimental error.

The intensities both of (0,5/7) and (0,6/7), in both cases, start to increase at temperature above 620-640 K, which corresponds to the appearance of the NiO(100) structure evidenced by the diffuse and broad spots near integral spots of Ni(100) as observed by LEED. This figure is the third evidence that suggests during annealing, at temperatures above 500 K, (0,5/7) spot degrades and (0,6/7) intensifies. Until temperature reaches 570-585 K, then the (7x7) structure gives in to the NiO(100). The 7th order spots profiles, similar to those shown in Fig. 13, during annealing are shown in Figure 23. Figure 23A, B and C are 7th order spot profiles during annealing of surfaces adsorbed at 300 K, 350 K and 400 K correspondingly. In Fig. 23A, the slight intensification of (0,6/7) just before it fades into NiO(100) starts between the 150th and 160th profile, ca. 520 K, then at 580-590 K (about the 200th profile), (0,6/7) completely disappears and NiO(100) emerges. Similar behavior is more obvious in Fig. 23B, where (0,5/7) is smoothed out around the 120th or 130th profile (ca. 530 K) and (0,6/7) slightly intensifies at the same time. Around the 170th profile, the (0,6/7) spot is smoothed out by NiO(100) which is located between (0,5/7) and (0,6/7). Again, in Fig. 23C, (0,6/7) slightly intensifies at ~150th profile(~520 K) and fade out between 210th-220th profile. They indicate that the point, where the

Figure 22. Changes of integrated spots intensity during annealing.
(A) Obtained after adsorbed oxygen at 350 K with
5×10^{-8} torr pressure for a total of 162 L exposure and then heating to 640 K with the heating rate 1 K/sec.
(B) Obtained after adsorbed oxygen at 400 K with
9×10^{-8} torr pressure for a total of 234 L exposure and then heating to 652 K with the heating rate 1 K/sec.

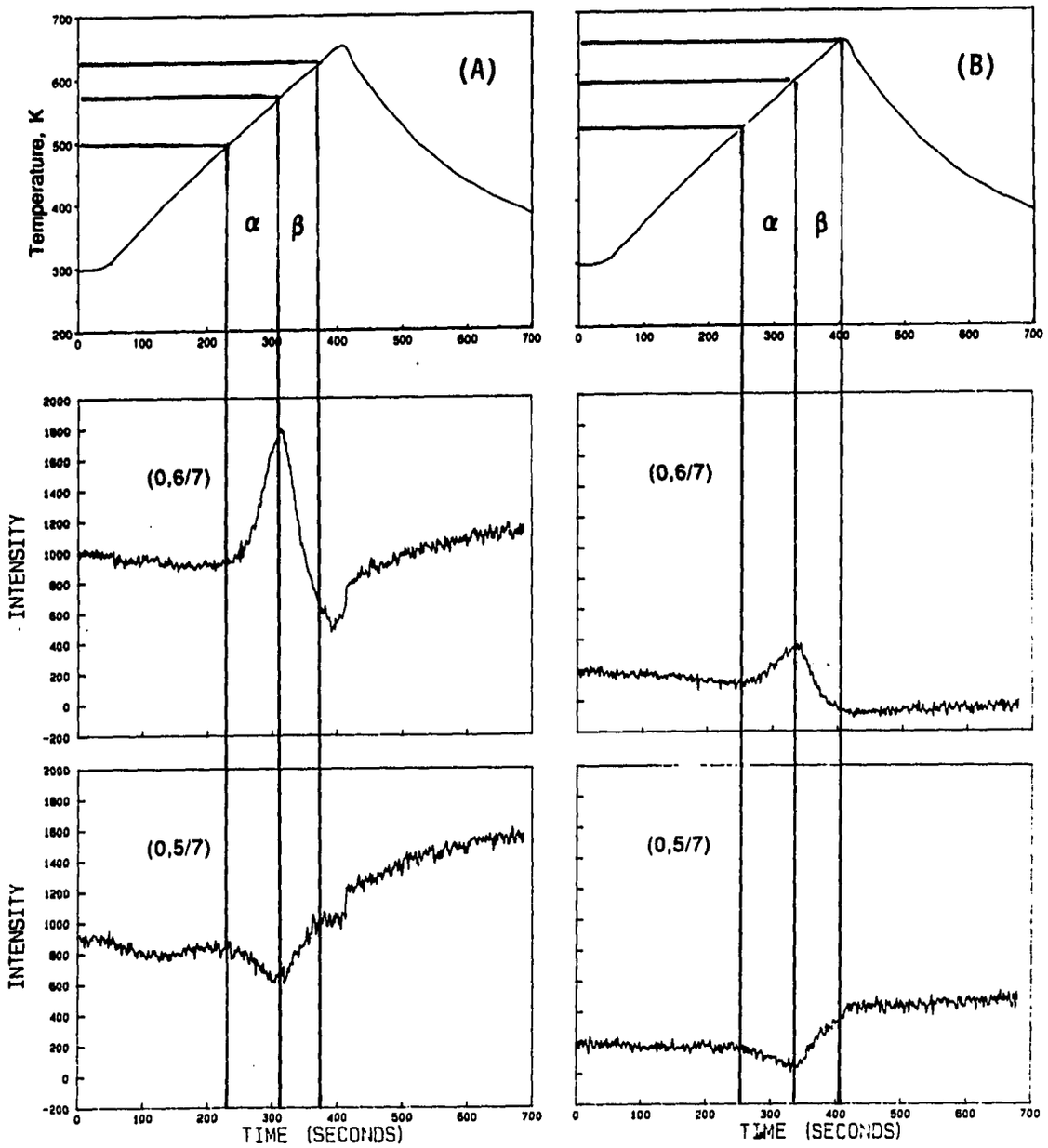
(A)
(B)
Temperature, K
α
β
(0,6/7)
(0,5/7)
INTENSITY
TIME (SECONDS)

(0,6/7) spot intensity in Fig. 22 starts to increase corresponds to the disappearance of (0,5/7) spot and slight intensification of (0,6/7) spot, marked by filled arrows in Figure 23, and the point where the (0,6/7) intensity starts to decrease corresponds to the appearance of broad NiO(100) spots and the disappearance of (0,6/7), marked by open arrows in Figure 23. This evidences that the peculiar behavior of the integrated spot intensity in Fig. 22 are not due to artifacts. The increase or decrease in spot intensity is indeed due to the intensification or degradation of (0,6/7) and (0,5/7) spots. We also notice that all the NiO(100) structure obtained after annealed to above 640 K show an average of 5% expansion, at the electron beam energy used (46 eV), from its normal lattice structure, which has been reported by Christensen et al. [27]. They observed the NiO(100) lattice expanded by about 7% from the bulk NiO lattice parameters.

Possible Models for the (7x7) Pattern

Multiple scattering model and overlayer modulation model

Satellite spots around integral order spots have also been observed on other systems with LEED. For instance, May and Germer reported satellite spots of O/Ni(110), which was attributed to multiple scattering effect [47], and Palmberg and Rhodin observed satellite spots of Ag/Cu(100), which was interpreted with both multiple scattering theory and overlayer modulation model [48]. Usually, appearance of "extra"

Figure 23: 7th order spot profiles during annealing for adsorptions done at different temperatures.

(A) Obtained after adsorption at 300 K for 232 L, then heat to 648 K.

(B) Obtained after adsorption at 350 K for 360 L, then heat 654 K.

(C) Obtained after adsorption at 400 K for 270 L, then heat to 652 K.

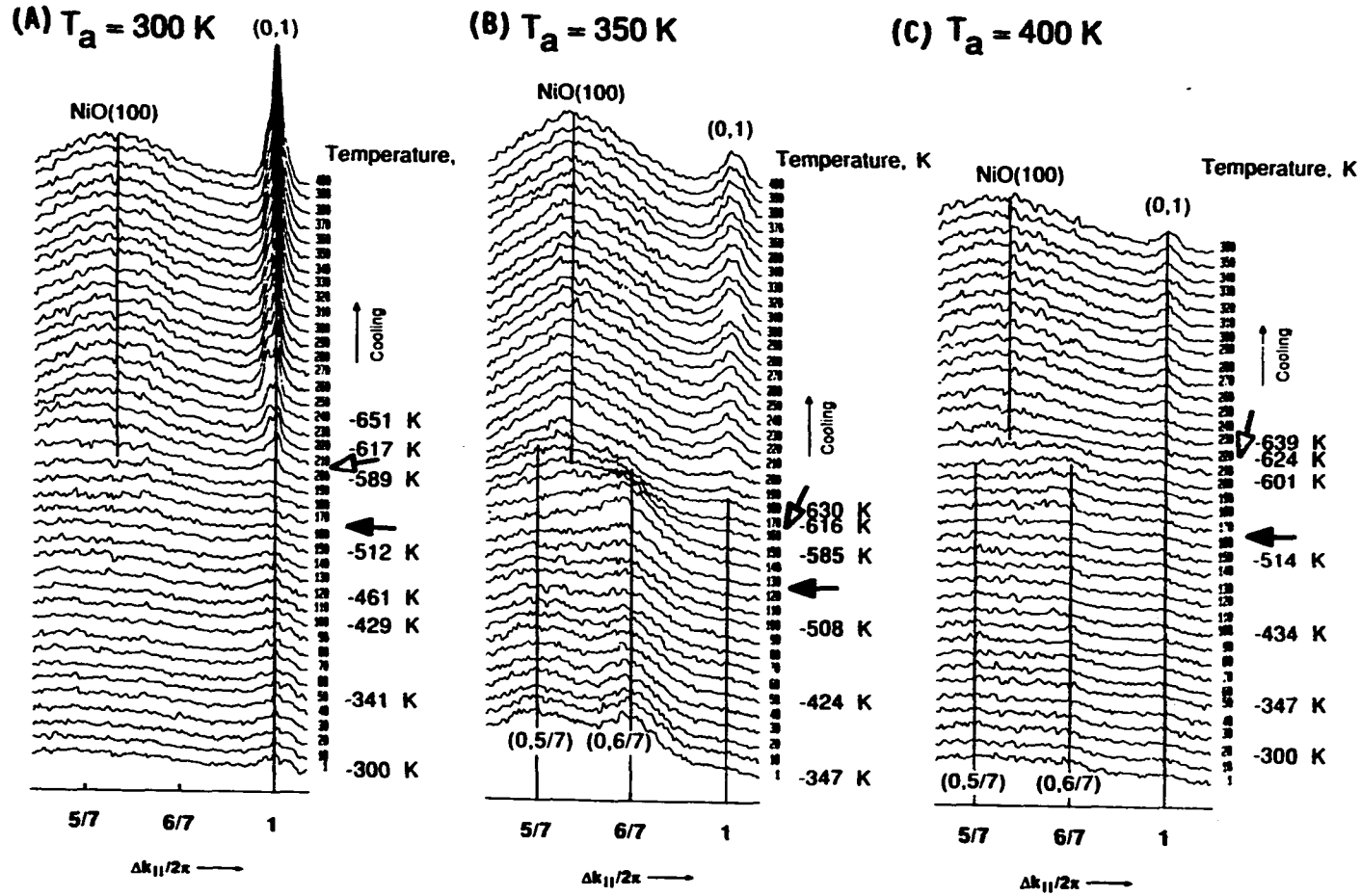
(A) T_a = 300 K
(0,1)
NiO(100)
Temperature,
Cooling
-651 K
-617 K
-589 K
-512 K
-461 K
-429 K
-341 K
-300 K
5/7
6/7
1
$\Delta k_{||}/2\pi$
(B) T_a = 350 K
NiO(100)
(0,1)
Temperature, K
Cooling
630 K
616 K
-585 K
-508 K
-424 K
-347 K
(0,5/7)
(0,6/7)
5/7
6/7
1
$\Delta k_{||}/2\pi$
(C) T_a = 400 K
NiO(100)
(0,1)
Temperature, K
Cooling
-639 K
-624 K
-601 K
-514 K
-434 K
-347 K
-300 K
(0,5/7)
(0,6/7)
5/7
6/7
1
$\Delta k_{||}/2\pi$

spots, which would not occur if only kinematical or single scattering is considered and if overlayer is planar, are important features in diffraction pattern, that indicate multiple scattering or overlayer modulation need to be considered. The former considers the occurrence of "extra" spots in terms of the multiple diffraction event. The latter considers the rise of "extra" spots in terms of the overlayer distortion relative to a planar configuration. Both theories are tried in this section to interpret the (7x7) pattern. The purpose is to see how well each theory can explain the experimental observations.

Multiple Scattering Theory The multiple scattering theory, as it is developed by Tucker [49] and Taylor [50] and later modified by Bauer [51] and Jona [52] predicts that the multiple-diffraction beams (spots) observed with the greatest intensity are those which correspond to a combination of one low-order overlayer reciprocal lattice vector and one low-order substrate reciprocal lattice vector. Additional multiple-diffraction beams, detected with considerably less intensity, can be attributed either to double-diffraction processes involving higher-order diffraction beams of the substrate and overlayer, or to triple-diffraction process.

According to this theory the spots, beside single diffraction beams of substrate and overlayer, that are intense should include:

(1,6/7), (1/7,6/7), (-1/7,6/7), (6/7,1), etc.

For instance, (1,6/7) is resulted from the combination of (0,6/7) and (1,0) of low-order overlayer and substrate spots.

The spots that are considerably less intense should include:

(0,5/7), (-1/7,5/7), (1/7,5/7), (6/7,5/7), etc.

For example (0,5/7) can be attributed to a double-diffraction process: (0,5/7) = (0,12/7) + (0,-1). Since the diffraction involves the higher order beam (0,12/7) of overlayer, (0,5/7) is predicted to be considerably less intense than those beams such as (0,1), (0,6/7), (1/7,6/7) and (-1/7,6/7) etc. However, this prediction contradicts with experimental observations, refer to Figs. 19 and 20 where the intensity of (0,5/7) is comparable or even higher than that of (0,6/7).

Overlayer Displacement Modulation Model The idea of overlayer displacement modulation considers the adatoms, that are not in registery with substrate, are trying to conform to the substrate structure to reduce the total energy. This conformity of the overlayer structure to the substrate to form a large "superstructure" unit mesh results in periodic displacements of overlayer atoms from a planar, non-distorted configuration. The picture of overlayer and substrate arrangement is similar to the one Ertl and Küpper used to describ the multiple scattering theory [53]. Refer to Fig. 24, where the open circles represent Ni or NiO unit cells of 2-dimensional. But the approach here is kinematic or pseudokinematic. It considers only how the distorted overlayer contributes to the fractional(splitted) spots.

The unit mesh scattering factor is known as [54]:

$$F(hk)=\sum_{i=0} f_i \exp\{-2\pi i[hx_j+ky_j+(1+\cos\theta)z_j/\lambda]\} \qquad (2.1)$$

where θ = angle in^out.

x_j, y_j =coordinate relative to substrate.

λ = incident wavelength.

The periodic displacement of overlayer in z-direction can be expressed in a periodic function:

$$z_j=\alpha\cos(2\pi x_j/7) \qquad (2.2)$$

α=amplitude of displacement relative to a planar substrate configration.

In the above equations x_j runs in steps of 7/6 from 7/6 to 6.

or $x_j = 7/6\xi_j$ where ξ_j=1....6, for y=0,7/6,...35/6.

Substitute x_j and z_j into eq. (2.1), complicated derivations can be found in Appendix 1., following results can be obtained:

In addition to substrate integral spots, overlayer primary diffraction spots should be observed at:

$h=m6/7$, $k=n6/7$ where m, n are integers

secondary diffraction spots should be located at:

$h=(6m\pm1)/7$, $k=(6n\pm1)/7$

higher order diffraction spots are at:

$h=(6m\pm2)/7$, $k=(6n\pm2)/7$

and so forth.

The intensities of the secondary order spots should be ~5-12% that of primary spots, and third order spots should be ~0.02-0.35% that of

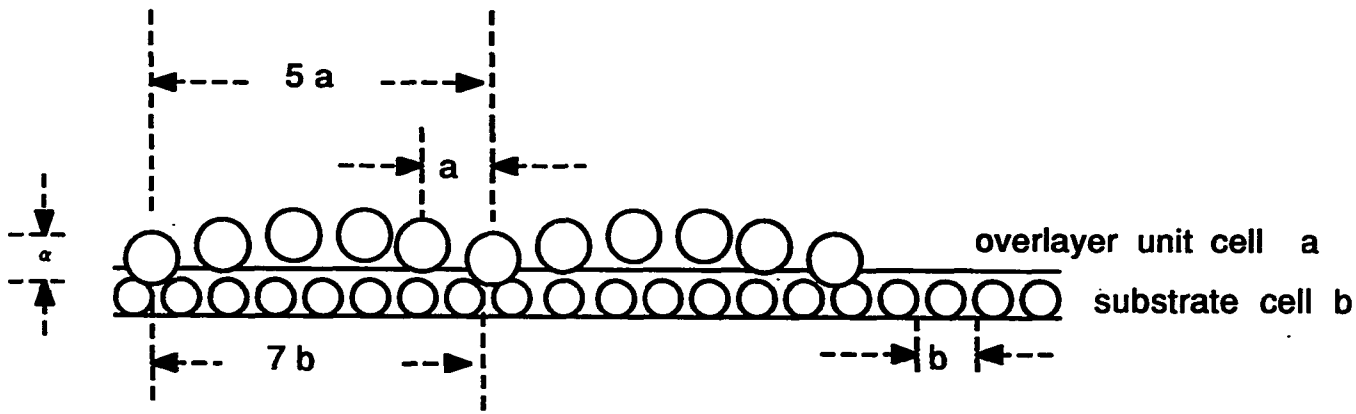

Figure 24. Model of the overlayer modulation theory.

primary spots. Again, these intensity predictions contradict the experimental observations. For instance, in this prediction, (0,5/7) is one of the secondary diffraction spots, which presumably should be 5-12% of the (0,6/7) spot intensity. This obviously disagrees with experimental results. Search of other possible model continues after the failure of the last two.

Anti-phase wall model

A new approach to the problem leads to a structure with highly correlated anti-phase walls within the (7x7) unit mesh. This structure can better explain the experimental observations than the previous two, although it too has some weakness.

It is known NiO has the NaCl lattice structure. The unit cell is drawn in Fig. 25A, where open circles and black dots represent either oxygen or nickel atoms. To simplify the problem, two-dimensional unit cell is shown in Fig. 25B and will be used in the discussion of (7x7) structure modelling from now on. The oxidation of Ni(100) is generally thought to be a nucleation and growth process. To picturize the oxidation progression, Figure 26A shows randomly distributed oxide nuclei start on the lattice mesh, B shows the 1-dimension situation when grown nuclei meet others at the boundaries (to distinguish this from the conventional concept of domain boundaries, we will call it wall from now on). In Fig. 26B, two pictures of the grown nuclei are drawn. One shows that the grown nuclei meet in-phase and form a uniform NiO lattice, the

other shows that they meet anti-phased and build anti-phase walls between them. Practically, there is no reason for them to meet in-phase and form a uniform NiO lattice. It is likely that they will meet and form walls between them. Therefore the first picture of Fig. 26B will not be discussed further. With the kinematic theory, assuming scattering factor f for NiO unit cell, the one-dimensional lattice factor of the structure, as shown in Fig. 26B, with randomly distributed walls can be written as following:

$$F=f(1+e^{(iha^*)\frac{1}{2}a}+e^{(iha^*)2a}+e^{(iha^*)3a}+e^{(iha^*)4a}+e^{(iha^*)5a}$$
$$+e^{(iha^*)6\frac{1}{2}a}+e^{(iha^*)7\frac{1}{2}a}+e^{(iha^*)9a}\ \ldots)$$

$$=\begin{cases} f(1-1+1+1+1+1-1-1+1\ldots.) & h=\text{odd} \\ f(1+1+1+1+1+1+1+1+1\ldots..) & h=\text{even} \end{cases} \qquad (2.3)$$

where $F^*F \propto I$, the diffraction intensity.

a is lattice constant.

$a^*=2\pi/a$, reciprocal space lattice constant.

Obviously, because of the presence of anti-phase walls, when h is odd, spot splitting may occur due to the alternation of scattering factors, which results in constructive or destructive diffractions. The splitting should be equally possible along k axis, when k is odd. Obviously, F varies with the distribution of anti-phase walls. Therefore changes in the oxide growth condition will result in different anti-phase wall arrangement, and therefore a different F*F. A different splitting pattern, therefore, results. This qualitatively explains why two

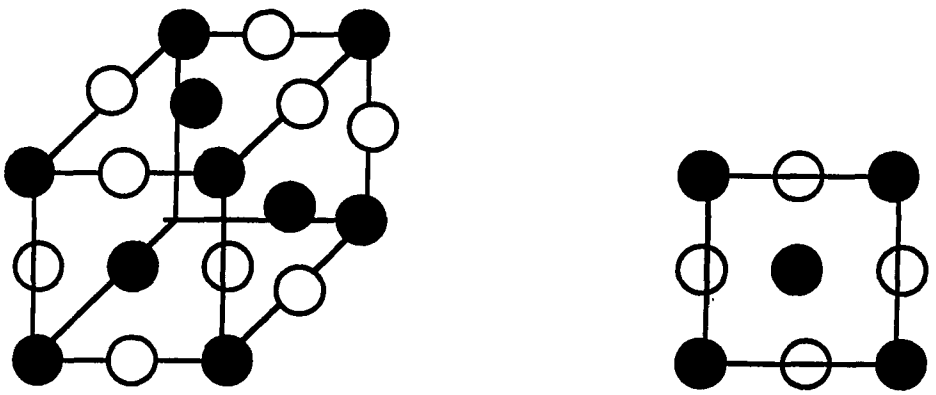

(A) (B)

Figure 25. NiO unit cell (NaCl type lattice structure).
(A) 3-dimension, (B) 2-dimension.

Figure 26. Pictures of the nucleation and growth process of Ni(100) oxidation.

(A) Oxide nuclei start randomly on the 2-dimensional lattice mesh.

(B) Two situations for the grown oxide nuclei to meet, one is to meet in-phase, the other anti-phase with anti-phase walls built randomly (one dimensional schematics).

(C) The picture of an assumed more regularly distributed wall.

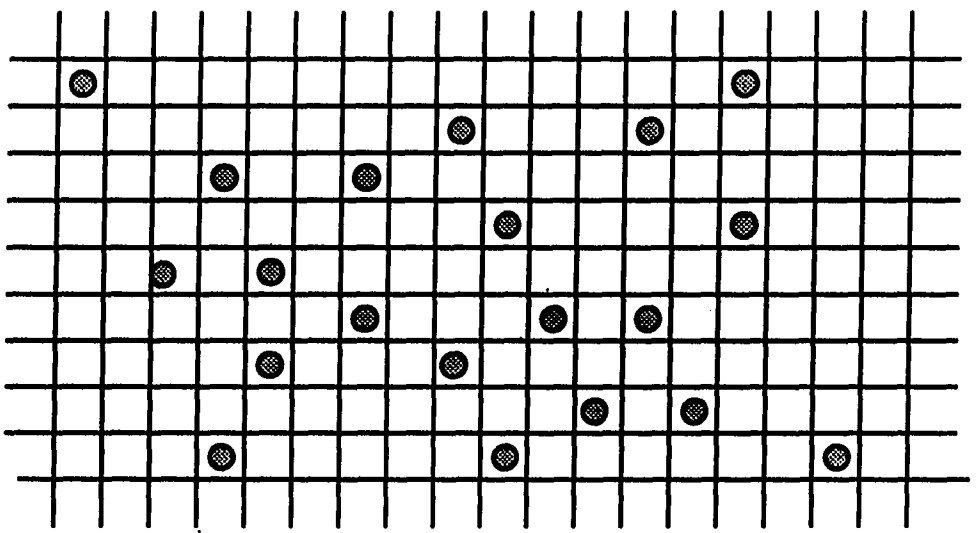

(A)

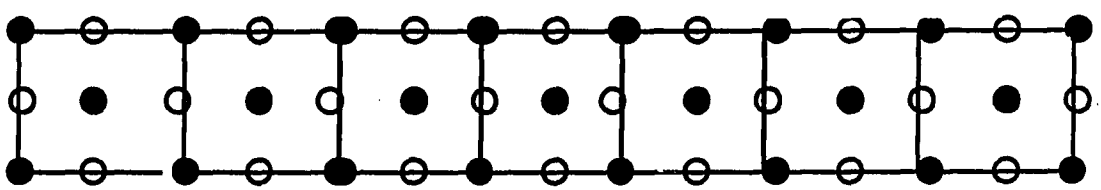

(B)

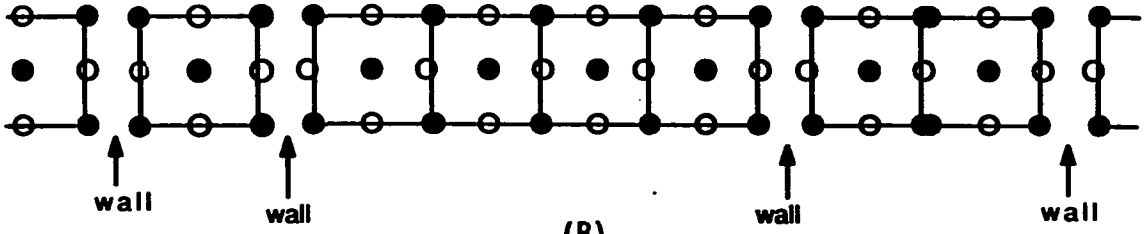

(B)

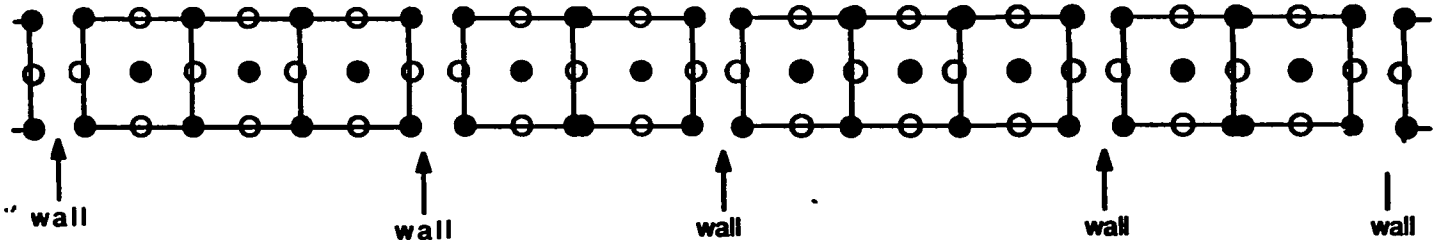

(C)

Figure 26 (Continued)

different patterns could be observed. This qualitative explanation is consistent with experimental observations shown in the LEED photos of Figures 19 and 27, where split only occurs at spots with either h or k odd, e.g., $(0,\pm1)$, $(\pm1,0)$, $(\pm1,1)$ and $(1,\pm1)$. No split is observed at (0,0) beam.

To quantitatively explain why the split is in 7th order and why there are two kinds of patterns observed, one with (0,5/7) more intense and the other with (0,6/7) more intense, some kinematic simulation is needed. Now let us look at the one-dimensional structure, with randomly distributed walls as shown in Fig. 26B, in another way. In Fig. 28A, assuming the NiO unit cells can be numbered along x-axis, then we will see, along the one-dimensional lattice, there are two types of NiO unit cells, one with positive scattering factor f, the other with negative scattering factor -f, as shown in Fig. 28B. Therefore the scattering factors of NiO unit cell on surface alternate in the way shown in Fig. 29A. To simplify the problem, anti-phase walls can be assumed to alternate in a more regular manner, as shown in Fig. 26C. The corresponding scattering factor function is shown in Fig. 29B, where M is the average periodicity of anti-phase walls. By Fourier transformation, the scattering factor function shown in Fig. 29B can be expressed in an analytical form:

$$f_M(y) = (4/\pi)\sum_{m=0}^{\infty}[1/(m+1)]\sin[(2m+1)\pi y/M] \qquad (2.4)$$

The kinematic diffraction intensity in 2-dimension is:

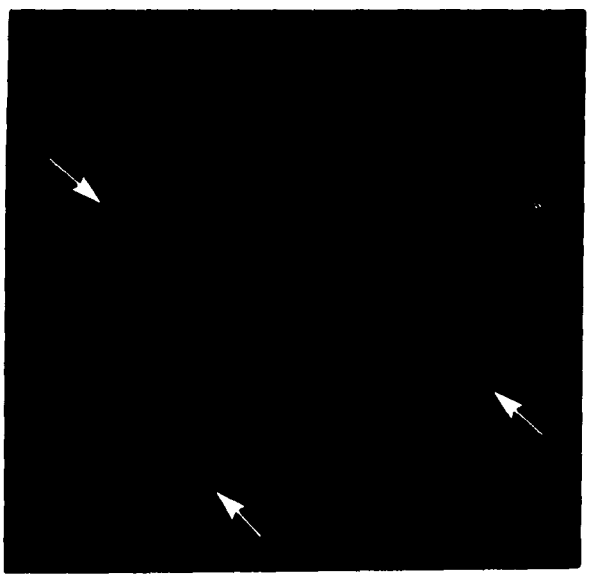

Figure 27. LEED photo of the (7x7) structure at 78 eV, obtained after adsorption at 350 K, with pressure 5.5×10^{-8} torr for 400 L. The photo is taken at liquid N_2 temperature. Integral spots (0,1), (1,0), (-1,0) are marked by arrows.

$$I(hk) = \left| \sum_{n_1=0}^{N_1-1} \sum_{n_2=0}^{N_2-2} f\, f_M(n_2)\, \exp\{2\pi i(n_1 h + n_2 k)\} \right|^2$$

or
$$I(hk) = f^* f \frac{\sin^2(N_1 2\pi h)}{\sin^2(2\pi h)} \left| \sum_{n_2=0}^{N_2-1} f(n_2)\, \exp(2\pi i n_2 k) \right|^2 \qquad (2.5)$$

It is the summation term above gives split along k-axis (similarly split along the other direction can be derived). Detailed derivation of this equation can be found in Appendix 2. The summation term in the above equation can be further simplified to give:

$$F^*F = \frac{4}{\pi^2} \left| \sum_{m=0}^{\infty} 1/(2m+1)\{\exp[i\pi\{k+(2m+1)/2M\}(N-1)] \frac{\sin N\pi[k+(2m+1)/2M]}{\sin \pi\,[k+(2m+1)/2M]} \right.$$

$$\left. -\exp[i\pi\{k-(2m+1)/2M\}(N-1)] \frac{\sin N\pi[k-(2m+1)/2M]}{\sin \pi\,[k-(2m+1)/2M]}\} \right|^2 \qquad (2.6)$$

Detailed derivation can be found in Appendix 3. It is found that when the average periodicity M=1.75 of the substrate unit cell, 7th order split will occur with the (0,5/7) fractional spot most intense, and when M=3.5 the 7th order split also occur, but with the (0,6/7) fractional spot most intense in the latter case. The simulated spot profiles are shown in Fig. 30A and B for the two cases. Neither the peak intensity ratio of (0,5/7) to (0,6/7) in Fig. 30A proportionate to that of the experimental results of Fig. 20A and B, nor the ratio of (0,6/7) to (0,5/7) in Fig. 30B to those of Fig. 20C and D. That is because in calculation the arrangement of anti-phase walls are assumed to be

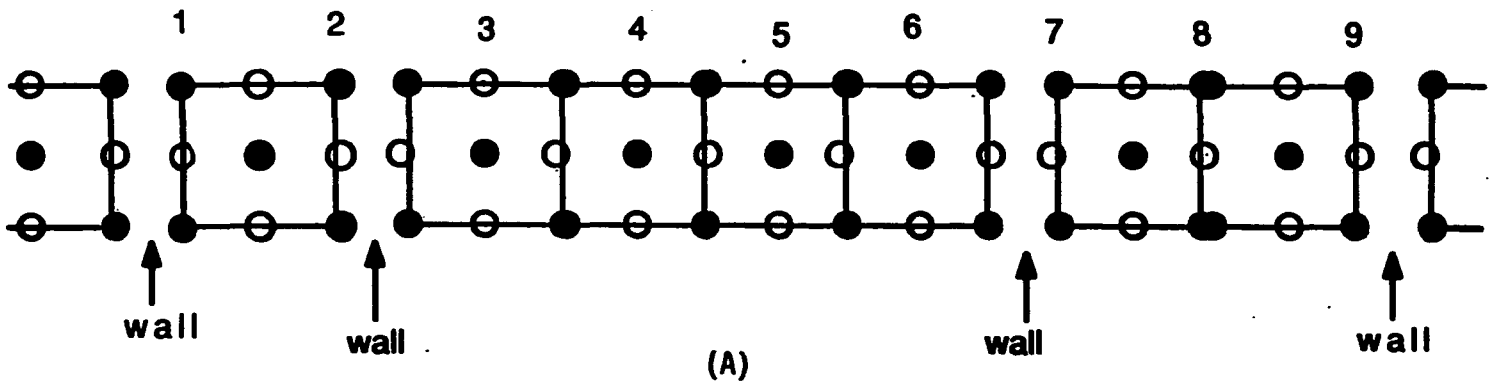

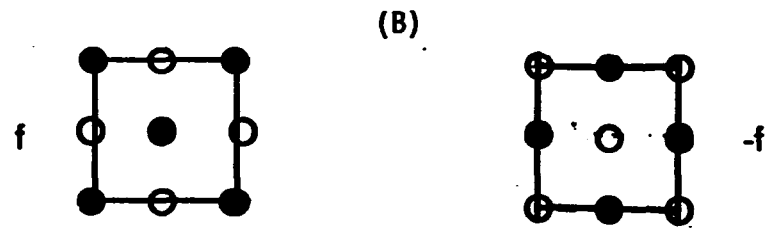

Figure 28. The same one-dimensional lattice as that shown in Figure 26b is duplicated here.

(A) One-dimensional lattice with randomly distributed walls and NiO unit cells numbered along the x-axis.

(B) Two types of NiO(100) unit cells with scattering factors f and -f.

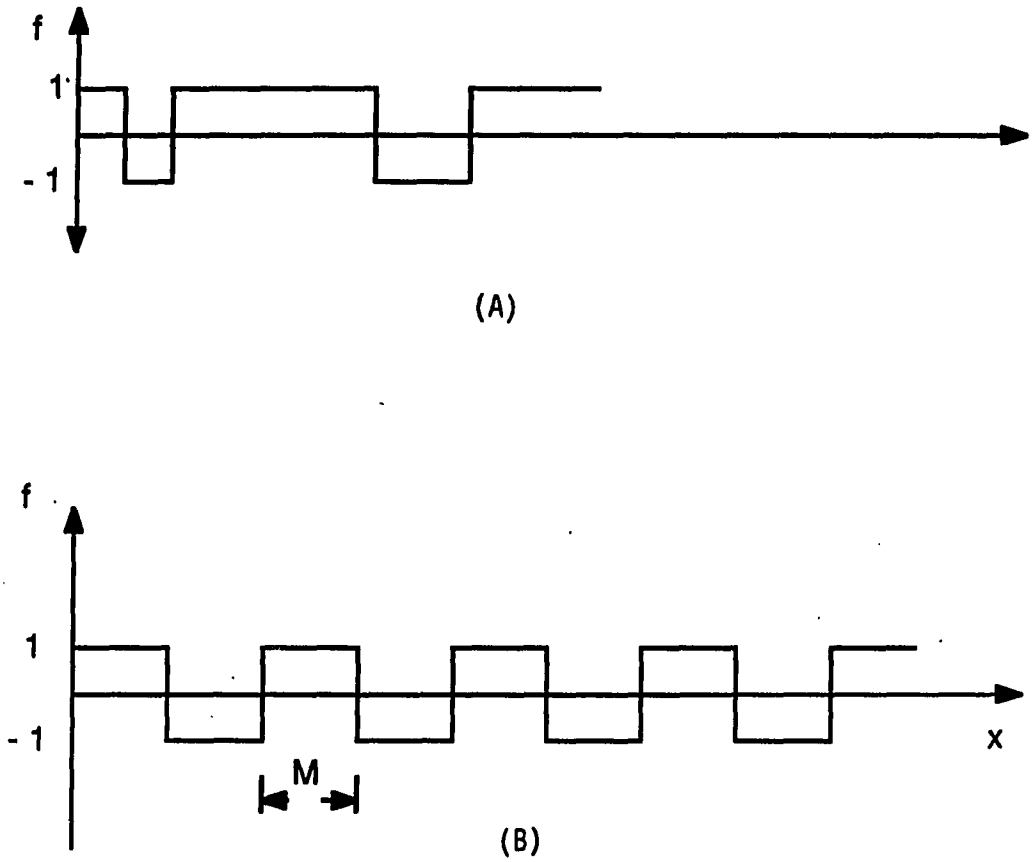

Figure 29. Scattering factor functions.

(A) Scattering factor function with randomly distributed walls of Fig. 26B.

(B) Scattering factor function of assumed regularly distributed walls of periodicity M.

perfectly uniform and regular. The size of lattice is assumed to be 100 unit cells in the calculations. The imperfection in real lattice structure broadens and reduces the diffraction peak. Also the experimental intensity of (0,1) spot is higher than what is expected theoretically, perhaps because of presence of uncovered Ni(100). Since the lattice constant of Ni(100) is 3.5238 Å and the 1.5% contracted NiO(100) lattice constant is (1-0.015)4.177 Å = 4.1143 Å, therefore 1.75 x 3.5238 Å = 1.5 x 4.1143 Å, i.e., the average periodicity M=1.75 of Ni(100) unit cell is equivalent to 1.5 of the oxide overlayer unit cell. Similarly, 3.5 of the Ni(100) unit cell is equivalent to 3.0 of the overlayer unit cell. The real space structure corresponding to M=1.75 and 3.5 can be drawn in Fig. 31A and B. However, the actual structure may not have anti-phase walls arranged so perfectly ordered. Slight disorder at the wall (for instance missing atom due to repulsion of ions, $Ni^{\delta+}$ or $O^{\delta-}$, with same charge) region are allowed. Some facts seem to support this model, for instance the FWHM (Full Width at Half Maximum) reduced by 35% when M change from 1.75 to 3.5, as shown in Fig. 32A and b. Experimentally, the data also show a slight but reproducible reduction by 5~10%. Another fact is that in Fig. 31, although the walls repeat in either M=1.75 or 3.5, the larger (7x7) unit mesh is the real repeating unit, i.e., the oxide overlayer is in registry with every 7th Ni(100) substrate unit cell. That is understandable because in order for the overlayer NiO to conform to the substrate Ni(100), forming the (7x7) unit mesh will cause the least lattice deformation (contraction or expansion). The formation of unit meshes with any other size will

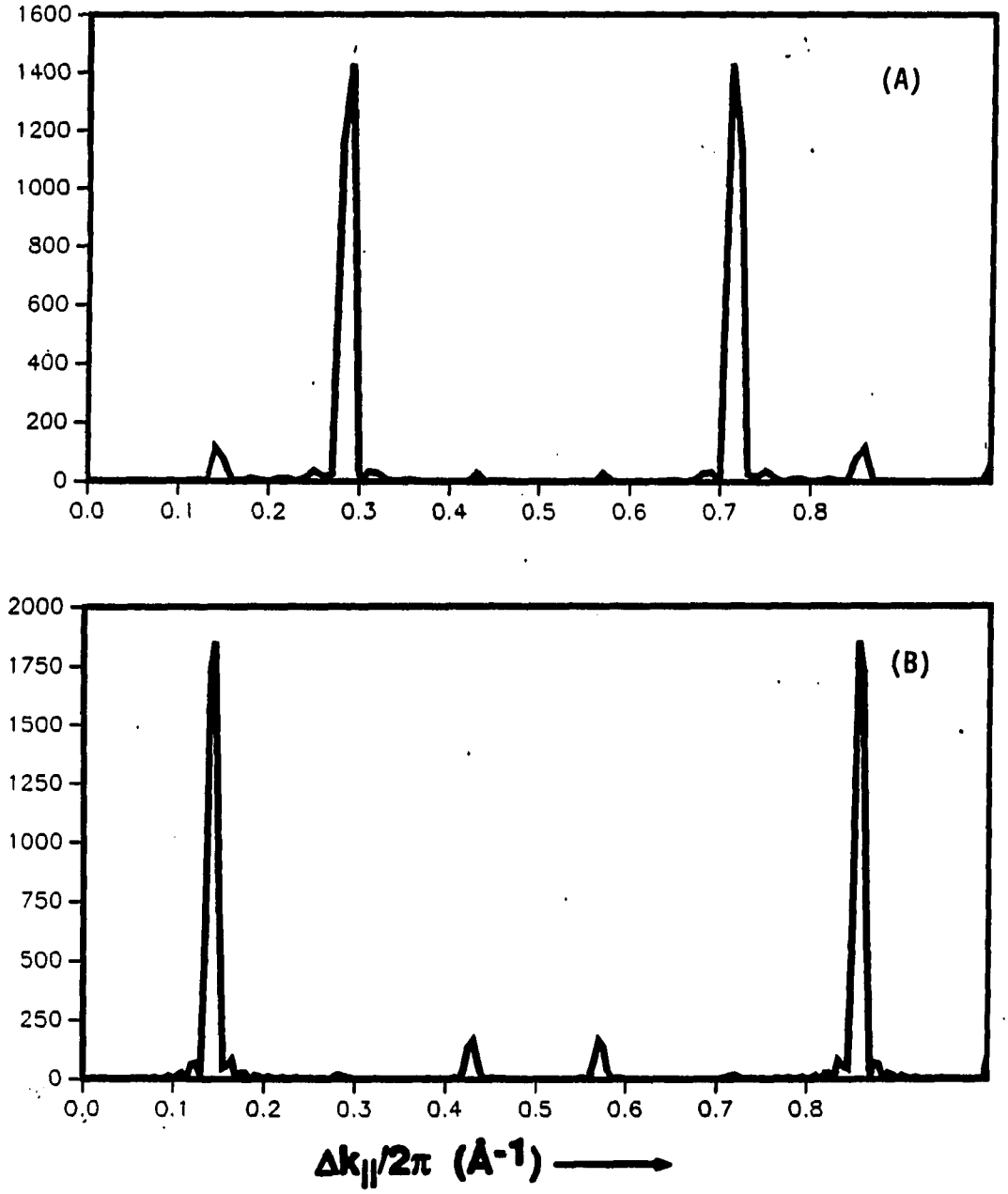

Figure 30. Theoretically simulated spots profiles.

(A) Average domain size M=1.75, number of unit cells in lattice is 100.

(B) Average domain size M=3.5, number of unit cells is 100.

accompany a larger amount lattice deformation. Additional support of the antiphase wall model is the work by Kopatzki and Behm [56]. With STM, they observed that even at chemisorption stage there are already plenty of antiphase walls present between the p(2x2) or c(2x2) domains and the average domain sizes are rather small, 2~3 atoms/domain. Therefore, with the addition of oxygen these pre-existing walls may well serve to limit the size of oxide domains to, e.g., M = 1.75 or 3.5, depends on adsorption temperatures. The weakness of the model, as mentioned before, is the presence of large numbers of walls, where same type of atoms are adjacent and repulsive. Also notice the presence of unexpected (0,2/7) and (0,1/7) spots in the simulated spot profiles shown in Fig. 30A and B. This can be explained by looking back to eq. (2.3), where the alternation occurs by assuming h = odd integer. Actually h can be any non-integer number across the Brillouin zone, such as h = 5/7 and 6/7. But in that case the phase factor

$$e^{(iha^*)a/2} \qquad (2.7)$$

across the antiphase wall will be some imaginary value. It will be difficult to show the physical picture of changes in scattering factor along the one-dimensional lattice of Fig. 26B in real numbers. The phase factor in eq. (2.7) will be real only when h is integer, and therefore, Fig. 29A results. For the points in reciprocal space where h equals to non-integer but close to 1, such as 5/7 and 6/7, we approximate them to 1, so that the step function of Fig. 29A still prevails, and we obtain the profiles of Fig. 30 correctly for $0.5 < \Delta k/2\pi \leq 1$. For the part with $0 < \Delta k/2\pi < 0.5$, since h has to be approximated to 0 rather than 1, eq.

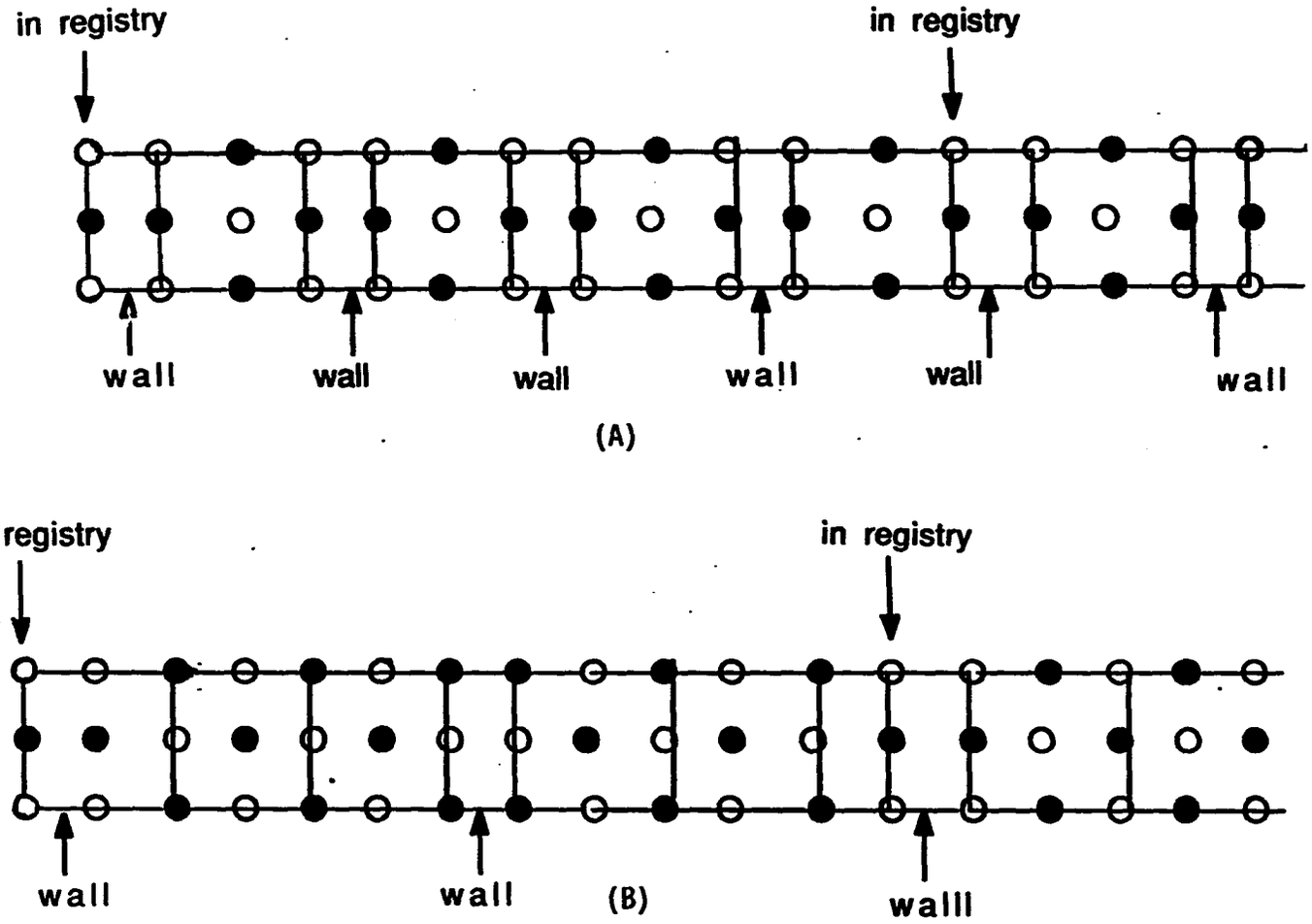

Figure 31. Real space structures of (7x7) with anti-phase wall periodicity (A) M=1.75, (B) M=3.5.

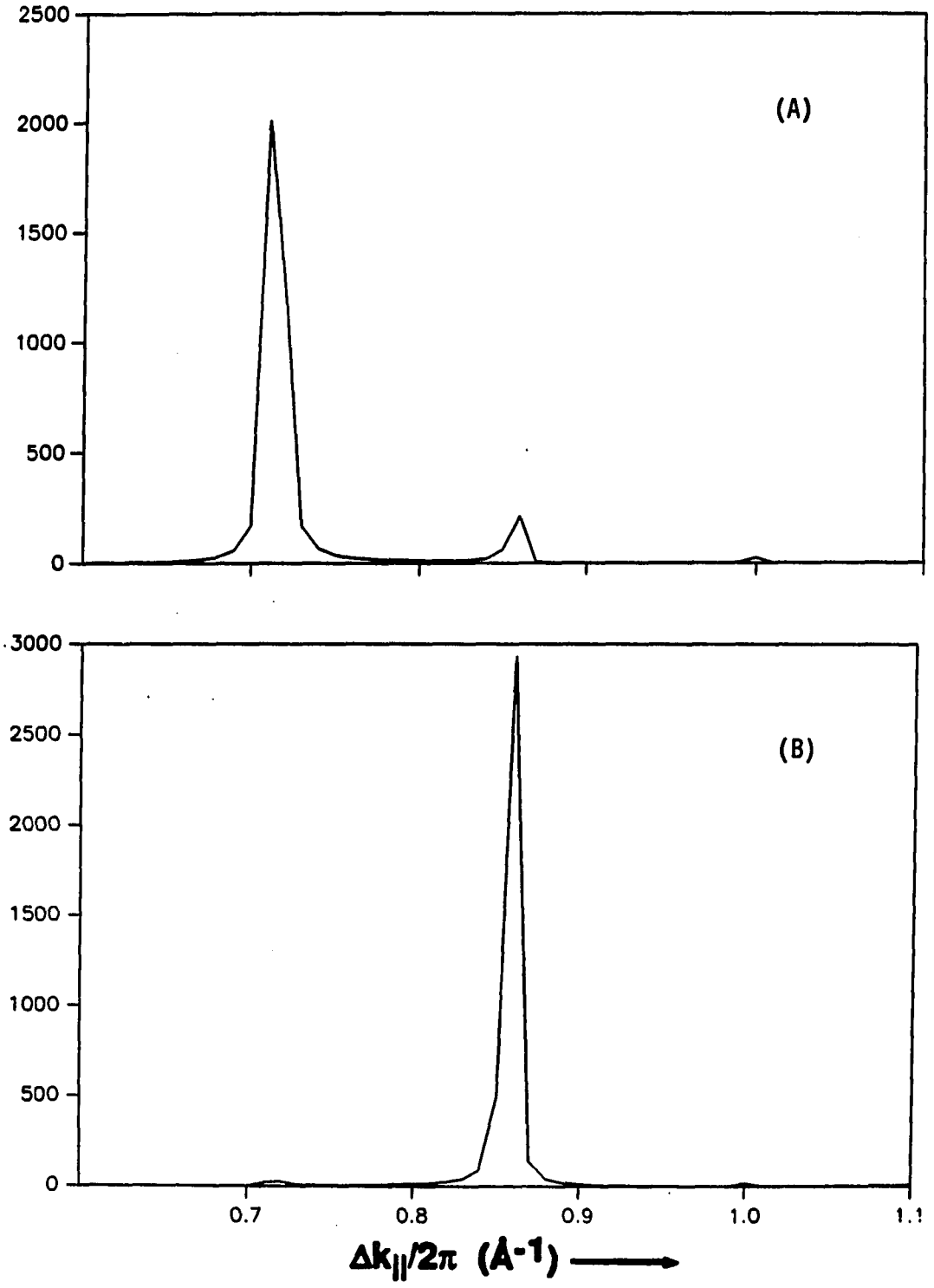

Figure 32: Enlargement of part of Fig. 26 to show the variation in FWHM of the 7th order spots in the cases (A) M=1.75, (B) M=3.5.

(2.7) results phase factor = +1, where no step function exist. Therefore, no split is expected for $0 < h < 0.5$ in the first Brillouin zone. In another word, in Fig. 30, only the part of profiles with $0.5 < h \leq 1$ should be used to compare with experimental results. The part with $0 < h < 0.5$ should be ignored.

The Diffuse Local Background The 7th order spots always overlap with a relatively high background, which, if considered as a diffraction spot, is broad in size and weaker in intensity than the true NiO(100) diffraction spots. Other researchers have previously recognized it as the indication of the existence of NiO(100) domains, although we have shown in Chapter 1 that the (7x7) is the dominant phase at 300-400 K temperature range. However, if we look at those fractional spots profiles in Fig. 20 more carefully, the following facts can be noticed. First, it is obvious that the high background does not show obvious increase in its intensity as the adsorption temperature goes from 350 K to 400 K, as shown in Figure 20. Rather it is more intense at 350 K than at 400 K. This does not support the proposition that the high background is from the diffraction of NiO(100) domains. Because as we have concluded in Chapter 1, higher adsorption temperature should favor the formation of thermally-activated phase NiO(100). There should be more and bigger NiO(100) domains forming at 400 K than at 350 K, and higher background intensity would be observed at high adsorption temperatures. But our observation is opposite to this. Second, the behavior of (0,5/7) and (0,6/7) spots intensity during annealing (refer to Figure 21) are

nearly opposite. It indicates that the high background is not due to the simple diffraction of a stable NiO(100) lattice that forms at the expense of (7x7). If a stable NiO(100) lattice does form at the expense of (7x7) as temperature increases, then the change in the spot intensities of (0,5/7) and (0,6/7) should be more or less synchronous, i.e., increasing or decreasing their intensities similarly. We make the following speculations here:

1. The high background is simply due to the overlap of 7th order spots. Since the (7x7) pattern formed at 350 K has the (0,5/7) spot relatively more intense than others, as shown in Figs. 18A and 20A and B, therefore the high background is sitting nearer (0,5/7). The (7x7) pattern formed at 400 K has the (0,6/7) spot relatively more intense, therefore the high background is more centered on (0,6/7), as shown in Figs. 18B and 20C and D. Figure 33 schematically shows the possible deconvolution of two assumed spots profiles. These profiles are by no means scaled to the measured intensities of various 7th order spot. They only relatively show, for instance in Fig. 33A, the local background is closer to (0,5/7). By assuming Gaussian distribution of the spot intensity (Lorenzian distribution or a combination of both will also work), and letting the (0,5/7) and (0,6/7) spots only differ in their relative intensity, for instance let the intensity of (0,5/7) be 1.5 times higher than the (0,6/7) and 6.7 times higher than (0,1), the overlapping of them gives Fig. 33A. By interchanging the intensities of (0,5/7) and (0,6/7) Fig. 33B is resulted. Notice there is no third spot present between (0,5/7) and (0,6/7). Similar to the profiles we observed

Figure 33. Deconvolution of 7th order spot profile with (0,5/7), (0,6) and (0,1) not equally intense and without presence of background intensity. Assuming Gaussian intensity distribution.

(A) $2Exp[-5(x-0.5)^2]+1.3Exp[-5(x-1.5)^2]+0.3Exp[-5(x-2.5)^2]$

(B) $1.3Exp[-5(x-0.5)^2]+2Exp[-5(x-1.5)^2]+0.3Exp[-5(x-2.5)^2]$

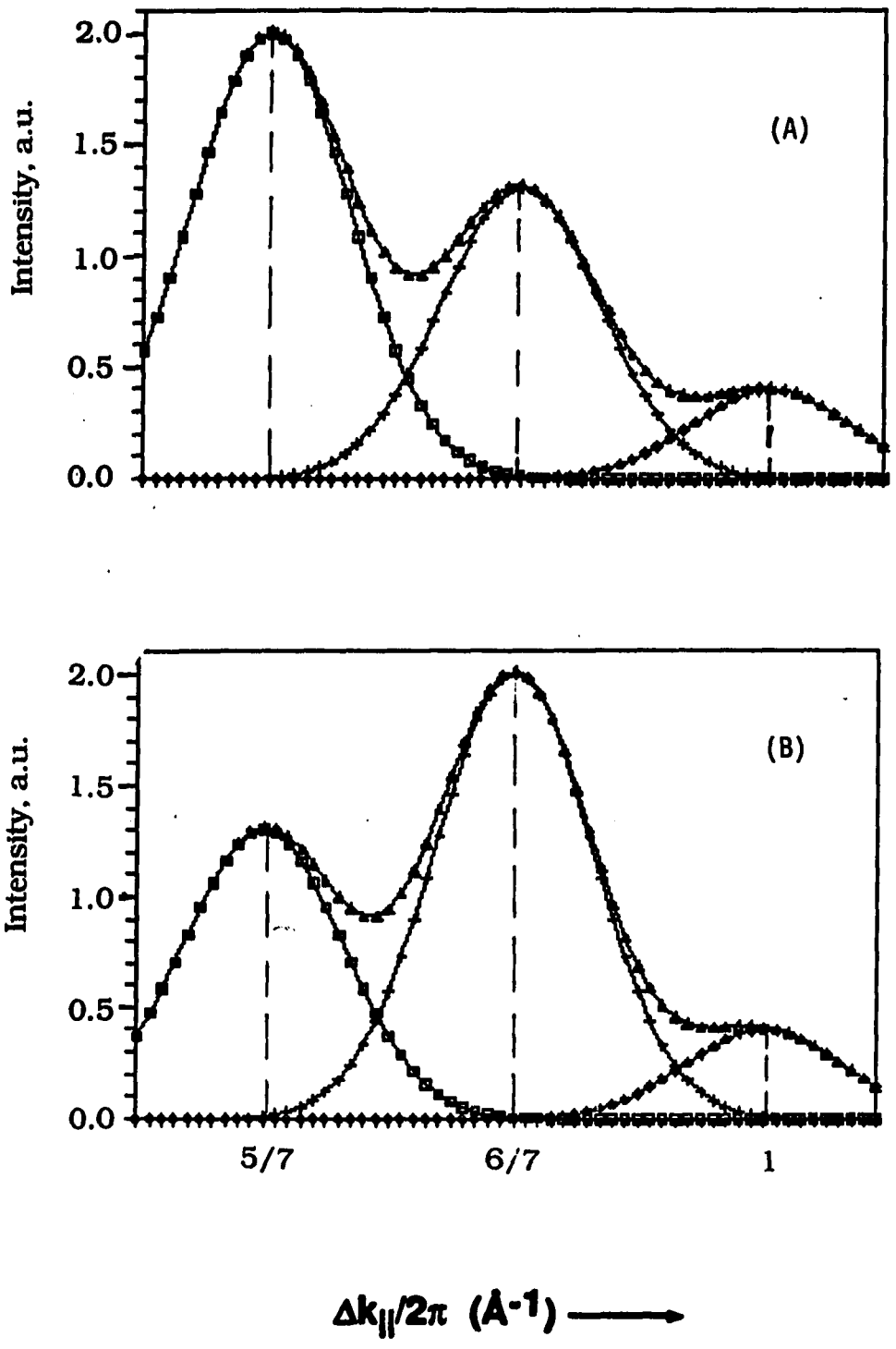
2.0
1.5
1.0
0.5
0.0
Intensity, a.u.
(A)
(B)
5/7
6/7
1
Δk||/2π (Å-1)

experimentally, indeed Fig. 33A has a high background intensity more centered on (0,5/7) and Fig. 33B has the high background more centered on (0,6/7). Therefore, Fig. 33 indicates the overlapping of two spots with different intensities can result in a high background nearer the more intense spot. This explanation is consistent with the two stage (7x7) proposition. At the first stage where (0,5/7) is more intense than (0,6/7), the overlap of the two spots results in a local high background closer to (0,5/7). At the second stage where (0,5/7) is less intense than (0,6/7), the high background is centered on (0,6/7). On the other hand, if we convolute three spots (0,5/7), (0,6/7) and the assumed coexisting NiO(100) Fig. 34 can result. In Fig. 34, same intensity is used for (0,5/7) and (0,6/7), so that the high background is only contributed by the presence of the assumed coexisting NiO(100). It can be shown in Fig. 34A and B, only by varying the location of NiO(100) diffraction spot between (0,5/7) and (0,6/7), can two type of profiles be resulted, i.e., one profile with the high background closer to (0,5/7), the other closer to (0,6/7). However, this means the coexisting NiO has different lattice constant when formed at different adsorption temperatures. This is unlikely, unless NiO(100) has lateral thermal contractions, i.e., lattice unit cell is smaller at 400 K than at 350 K so that the NiO(100) diffraction spot moves toward (0,6/7), which is almost impossible.

2. The opposite behavior of (0,6/7) and (0,5/7) during annealing, as shown in Fig. 22, is due to transition of the first stage (7x7) pattern to the second stage (7x7). Refer to Figure 18 for the observed

Figure 34. Convolution of (0,5/7),(0,6/7) and a background, presumbly from NiO(100), with (0,5/7) and (0,6/7) equally intense and superposed with NiO(100) spot. By moving the NiO(100) spot to get the higher background centered on either (0,5/7) or (0,6/7).

(A) $\mathrm{Exp}\{-[x-0.5]^2/0.3\}+1/3\mathrm{Exp}\{-[x-1.0]^2/4\}+\mathrm{Exp}\{-[x-2.5]^2/0.3\}$

(B) $\mathrm{Exp}\{-[x-0.5]^2/0.3\}+1/3\mathrm{Exp}\{-[x-2.0]^2/4\}+\mathrm{Exp}\{-[x-2.5]^2/0.3\}$

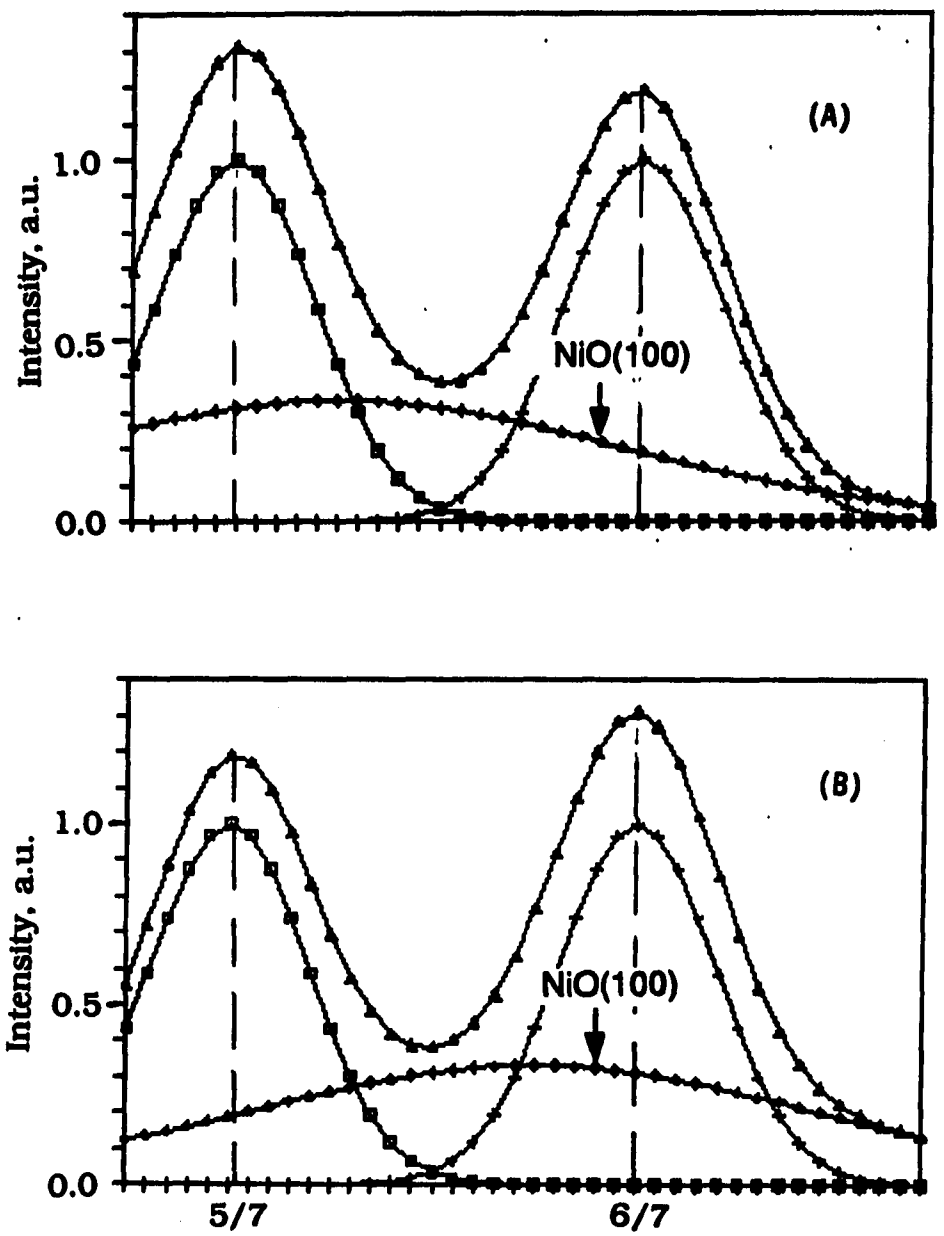
(A)
Intensity, a.u.
1.0
0.5
0.0
NiO(100)
(B)
Intensity, a.u.
1.0
0.5
0.0
NiO(100)
5/7
6/7
Δk∥/2π (Å-1) ⟶

two stages of (7x7) pattern. In region A of Fig. 22 the (0,5/7) fades and (0,6/7) intensifies. That indicates the second stage (7x7) forms at the expenses of first stage (7x7). Refer to the slight intensification of (0,6/7) spot during annealing in Fig. 23B marked by open arrows and region α of Fig. 22. In region B (0,6/7) is replaced by the broad spot of NiO(100) located between (0,5/7) and (0,6/7), refer to Fig. 23 of profiles corresponding to temperature above 600 K. This is the stage where NiO(100) forms at the expense of second stage (7x7). At temperatures above 640 K, NiO(100) is the only stable oxide phase remaining. The second stage (7x7) is thermodynamically more stable than the first stage (7x7) and kinetically more difficult to form. Therefore it might be proper to say that the first stage (7x7) forms at temperatures below 400 K and second stage (7x7) forms momentarily at temperatures above 500 K during heating process. At the intermediate temperatures, both first and second stage (7x7) structures can exist depending on their original adsorption condition. If adsorption is done at a lower (e.g., 350 K) temperature, there will be mainly domains of first stage (7x7) and this structure persists until the surface is heated to 500 K. The (7x7) pattern (profiles) show mainly the first stage character in this case. On the other hand, if adsorption is done at a higher (e.g., 400 K) temperature, a mixture of both first and second stage domains exists. NiO(100) is the most stable face of nickel oxide, but its formation is a thermally-activated slow process. The formation of NiO(100) will make the (7x7) patterns difficult to resolve. That is why we have to limit the adsorption temperatures below 400 K in studying

the two (7x7) patterns.

Discussion

We propose that the (7x7) structure of nickel oxide consists of highly correlated anti-phase walls within the larger unit mesh, p(7x7). The existence of two kinds of (7x7) patterns are due to different arrangement of anti-phase walls formed under different oxidation conditions. The first stage (7x7) has average periodicity of anti-phase walls M=1.75 of the Ni(100) unit cell, or 1.5 of the strained NiO(100) unit cell. The second stage (7x7) has M=3.5 of Ni(100) unit cell, or 3.0 of the oxide unit cell. The former forms at lower temperatures and the latter forms at higher temperatures. The transition from first stage (7x7) to the second stage (7x7) occurs at temperatures above 500 K during continuous annealing process. When temperature is high enough (above ~570 K), the NiO(100) domain start to develop, and by 640 K the only stable phase is NiO(100). Discussion on the (7x7) structure can be concentrated on four points.

The (7x7) Patterns And Their Real Space Structures This study agrees with Saiki et al. on the point that there is a 1.5% contraction in the (7x7) structure from regular NiO(100) [33]. Because the (7x7) pattern reported by Saiki et al. was obtained from room temperature adsorption, which is the condition that first stage (7x7) is supposed to form and shows eight fractional spot near (0,1). However, the reported (7x7) pattern (refer to Fig. 17) has only four 7th order spots around the

substrate integral spot rather than eight. That is perhaps because the fractional spots (±1/7,5/7) are not fully developed yet at room temperature, as shown in Fig. 20, the most observable (7x7) pattern forms at ~350 K. Other conditions result in poorly resolved 7th order spots. The (±1/7,5/7) are usually weaker than other spot even when they are observable. That is why Saiki et al. reported a (7x7) pattern which is more like the second stage (7x7) rather than the first stage (7x7). The real space (7x7) structure proposed by Saiki et al. is based on incomplete experimental results and simple geometrical calculation. Their model has uniform NiO unit cells within (7x7) unit mesh, while ours has anti-phase walls break the uniform NiO lattice. This anti-phase wall model has been used in explaining the spots splitting of bimetallic systems such as Cu_3Pd, CuAu and Ag_3Mg [55]. The only assumption made in the derivation of this kinematic model is the regularity of the walls and uniformity of the NiO lattice between walls. This requirement is relaxed experimentally, and the sharpness of the splitted spots is reduced and less resolved (7x7) pattern is what we actually observed.

The Energetic Factors Associated With The Formation Of (7x7) As we have shown in Fig. 31, although there is only one to three NiO unit cells between two neighbor walls, but the repeating unit parallel to the plane of the surface is in registry with every seventh Ni(100) unit cell. The partial registry of overlayer to substrate reduces the system total energy, relative to the formation of NiO(100). The presence of large number of anti-phase walls is perhaps also due to the huge strain and activation barrier accompanying the formation of mismatched NiO unit

cells. Actually, in the recent study by Kopatzki and Behm with STM and theoretical simulations, they found that the oxygen island size, corresponding to the p(2x2) and c(2x2) superstructures, are already rather small [56], ~three oxygen atoms per domain. On one hand, the presence of large numbers of anti-phase walls may be energetically unfavored, considering the repulsive interaction of O-O and Ni-Ni at the wall region. On the other hand, the partial registry of oxide layer with the substrate reduces the overall energy barrier associated with the formation of this peculiar structure, and the walls may serve to release the strain present at the metal-metal oxide interface. LEED pattern similar to this has also been observed on O/Ni(110) by May and Germer [47]. The pattern with fractional spots formed prior to complete oxidation to NiO(100) was assigned to a (9x4) pseudo-oxide, and the satellite fractional spots were attributed to multiple scattering effect without any quantitative explanation. If we take a close look at the LEED pattern presented in the paper (Figure 2), as shown in Fig. 35A with the integral spots (1,0) and (0,1) marked by arrows, we can see the (0,8/9) spot is much weaker than (0,7/9) and (0,1) (Miller indices are referred to the substrate), and the (5/4,0) spot is much weaker than (1,0) and (5/4,$\pm$1/9) spots. According to multiple scattering theory [48], the (0,8/9) and (5/4,0) spots are primary diffraction spot of overlayer NiO, which should be much more intense than the higher order spots such as (5/4,$\pm$1/9), (0,7/9) etc., which are due to double- or triple-diffraction process and are supposed to be considerably less intense. The LEED pattern shown in the paper contradicts this.

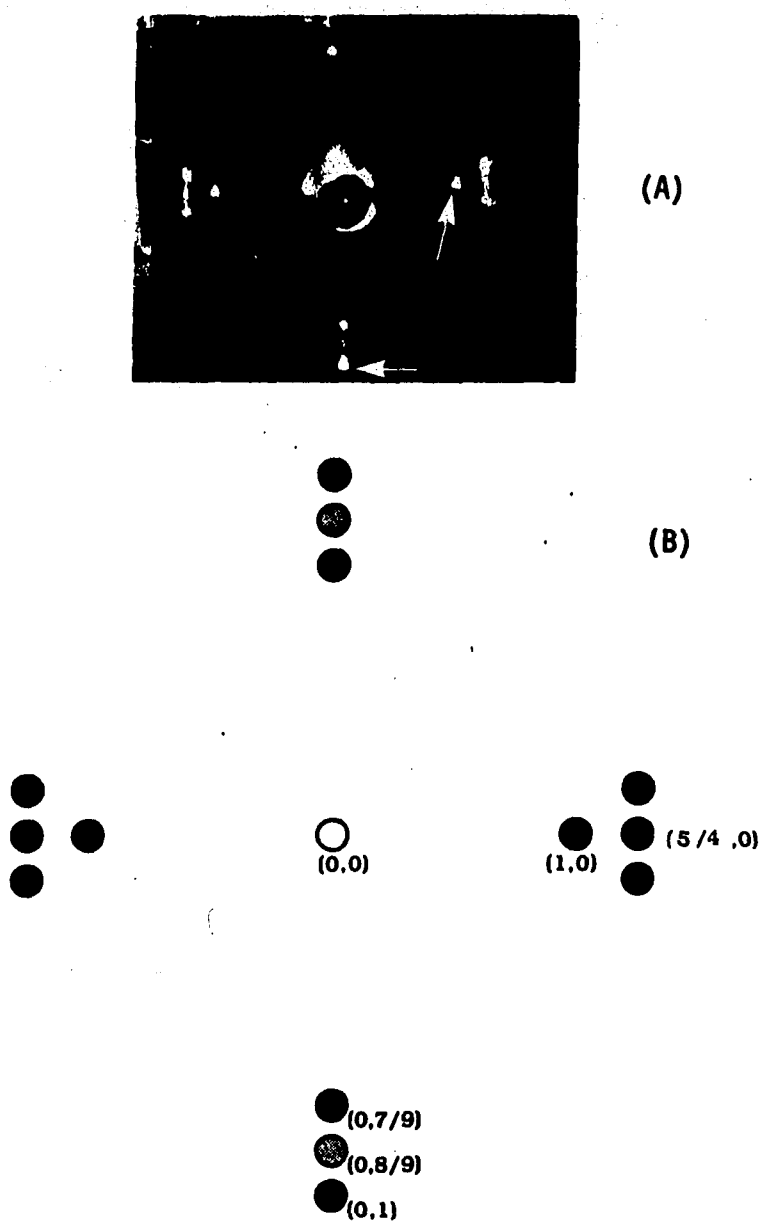

Figure 35. The observed and schematic (9x4)-O/Ni(110) patterns. After May and Germer [46].

(A) Photo of the (9x4)-O/Ni(110).

(B) Schematics of the LEED pattern in (A).

Therefore, it seems improper to attribute these satellite spots to multiple scattering effect. However if we adopt the anti-phase wall structure to the O/Ni(110) system and let the anti-phase wall periodicity along [100] to be 2 and along [110] to be 2.25, we get spot profile along the 9th order fractional spots as shown in Fig. 36A and along the 4th order spot as shown in Fig. 36B. In Fig. 36A, the anti-phase wall model predicts the 9th order spot (0,7/9) is more intense than (0,8/9). The observed intense spot (0,1) is probably due to contribution from substrate Ni(110). Again the "extra" spot (0,2/9) in the simulated profile can be ignored because it is located at $h < 0.5$ in the first Brillouin zone. The (0,8/9) spot is ~1/36 of (0,7/9) spot. We do not have quantitative intensity of (0,7/9) and (0,8/9) to compare with the prediction, but the (0,8/9) is indeed considerably less intense than (0,7/9) by visual observation of the photo. In Fig. 36B, the (3/4,0) and (5/4,0), etc., are predicted to be intense by the model. But in the photo presented in the paper, only (5/4,0) is intense. The prediction along [100] is not as good as along [110]. Perhaps it is because of the anisotropy of Ni(110) surface so that the antiphase wall structure prevails in one direction, not the other. The observed (1,0) and (0,1) spots are again perhaps contributed by uncovered substrate Ni(110). This proposed (9x4) structure, by May and Germer, [47] has recently been observed by STM study of Ritter and Behm [57]. The oxide overlayer, indeed, contracted by ~5% from regular NiO(100) structure to conform to the substrate lattice. Therefore, there must be some internal advantages about this partially registered oxide overlayer, from the system total

Figure 36. Simulations of pseudo-(9x4) pattern of O/Ni(110), see reference 46.

(A) Fractional spots profile of the 9th order spots with M=2.25, number of unit cells assumed to be 100.

(B) Fractional spot profile of the 4th order spots with M=2.0, number of unit cells assumed to be 100.

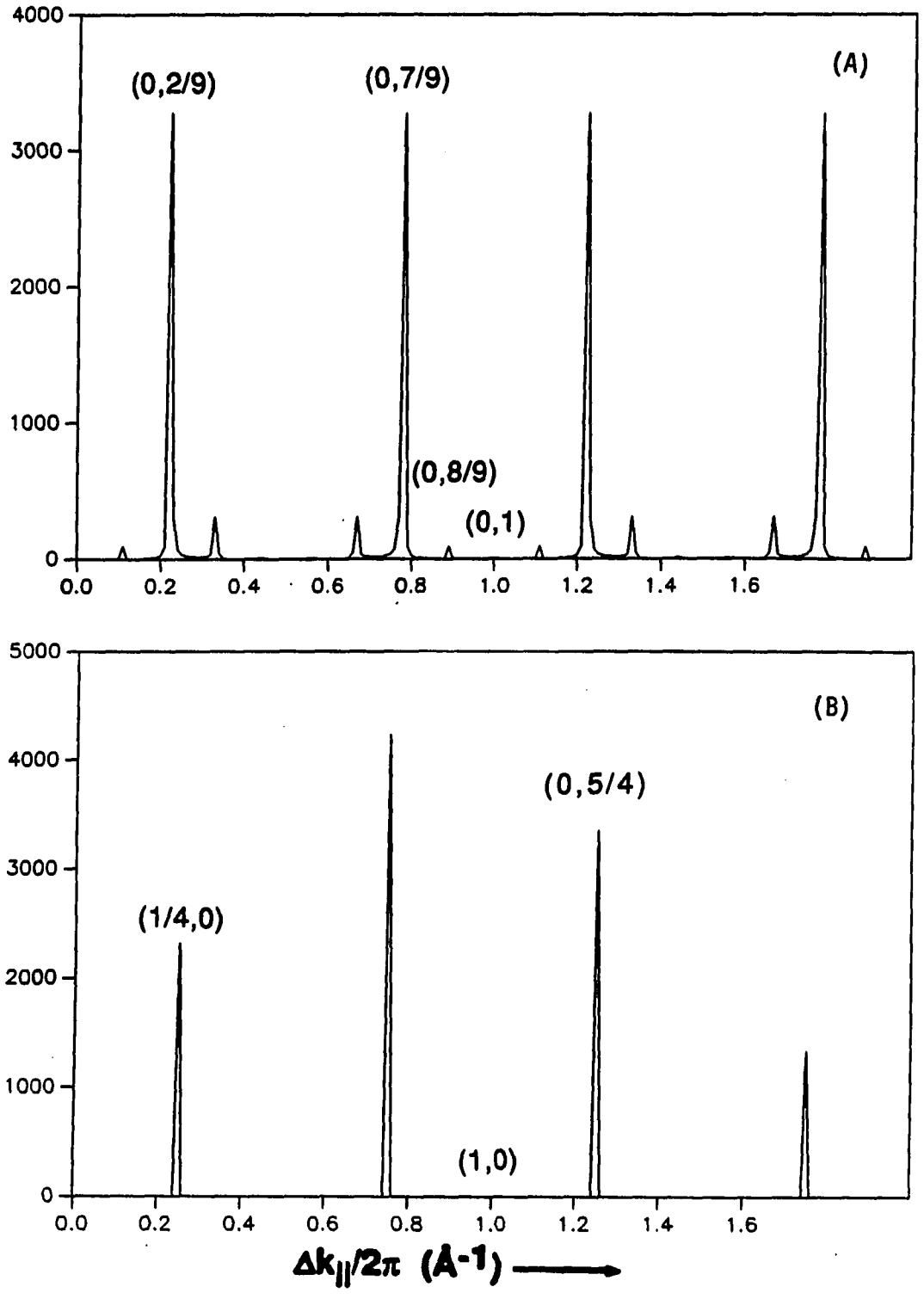
4000
3000
2000
1000
0
(0,2/9)
(0,7/9)
(A)
(0,8/9)
(0,1)
0.0
0.2
0.4
0.6
0.8
1.0
1.2
1.4
1.6
5000
4000
3000
2000
1000
0
(B)
(0,5/4)
(1/4,0)
(1,0)
0.0
0.2
0.4
0.6
0.8
1.0
1.2
1.4
1.6
Δk||/2π (Å-1)

energy point of view. This point will be further discussed at the end of this dissertation. Note, the predicted (3/4,0) is not experimentally observed. We do not know how to explain this extra spot yet at this time.

Physical Possibility Of Transition From First To Second Stage (7x7)

During transition from first to second stage (7x7), about half of the anti-phase walls have to be eliminated, refer to Fig. 31 for the different distributions of anti-phase walls when M=1.75 and 3.5. Therefore massive atomic rearrangement must occur. Although we do not possess strong evidence to show how this rearrangement actually proceed, however, high diffusion mobility has been reported for Ni in the nickel oxide [58]. It is possible that once the Ni atoms gained enough thermal energy during annealing, they will leave their positions near the walls, where strain due to lattice mismatch and repulsion from adjacent Ni atoms exist. Then, the massive rearrangement will follow this initiative.

Summary

In this chapter, possible models that might explain our observation of the (7x7) pattern are presented and compared. We find the multiple scattering theory and overlayer modulation model that are usually used in explaining satellite spots of LEED patterns can not interpret the data. However the anti-phase wall model simulates the observed two kinds of (7x7) spot profiles both in the spot location and in relative intensity of various 7th order spots.

The local high background superimposed on (7x7), refer to Fig. 4D and E, is interpreted as due to overlap of various 7th order spots rather than coexisting NiO(100) domains.

Finally, the study on O/Ni(110) together with this study seems indicate that although NiO(100) is the most stable phase of NiO on surface, but its formation has to be via some intermediate state, where oxide overlayer can be partially in registry with the substrate. Once the intermediate state (which is similar to NiO(100) but contracted slightly, -1.5% in the case of O/Ni(100) and -5% in the case of O/Ni(110) is organized and settled to a certain domain structure, further annealing of this intermediate state (or more thermal energy gained by the lattice at the intermediate state) will result in destruction of the contracted NiO(100) and formation of regular NiO(100).

CHAPTER 3: EVIDENCE FROM AES AND I-V MEASUREMENT

Results

As we have reported in Chapters 1 and 2, two different nickel oxide epitaxies have been observed with LEED when oxygen is adsorbed on Ni(100) at substrate temperatures above and below 300 K, denoted NiO(111) and (7x7)-O respectively. In this chapter, AES measurements of adsorbed and/or thermally treated surfaces are presented to show that AES may be sensitive to differences in surface orientations. AES as a surface study tool can not only answer what elements and how much of each element is present, but also answer to what other atoms is an atom of a given element bonded and how is a given element bonded to other element. By analyzing the energy positions of spectral features and the lineshapes, the change of chemical enviroment on the surface can be revealed. Chemically induced changes in spectral shape include the appearance and disappearance of peaks, changes in widths of lines in the spectrum and changes in relative intensities of spectral features.

The parameters used in our AES measurement are: 2 keV incident beam energy, 1 v peak-to-peak modulation amplitude, unless otherwise specified, and 0.2 μA beam current. The I-V curves are measured in 2-3 eV increments and scanned over an energy range 30-280 ev. Other experimental details are given in Chapter 1. Because valence electrons are expected to undergo the strongest changes as a result of changes in

chemical environment, and these changes will be both in energy levels and in density of states (DOS) distributions, thus those Auger signals involving valence electrons are expected to reflect chemical changes more directly than those that do not. Therefore, the three Auger lines with the following Auger identifications are collected in our experiments: Ni-L_3VV, Ni-$L_3M_{23}V$ and Ni-$M_{23}VV$. These are shown in Figs. 37, 38 and 39, respectively. Auger measurements are conducted on the surface that have been treated under different conditions, with varied exposure and/or annealing temperature, in order to see the Auger line changes as oxidation progresses. We put together each Auger line, from different measurements, into one figure for comparison purposes. For example Fig. 37 shows eight Ni-L_3VV Auger lines from the following measurements. Curve A through D correspond to increasing oxygen exposures at room temperature. Curve A is from the measurement of a clean Ni(100) surface, curve B is taken on the surface exposed to 1.5 L oxygen at 300 K, curve C is obtained from the surface with 50 L oxygen exposure at 300 K, and curve D is from a surface exposed to 122 L oxygen at 300 K where oxides [both NiO(111) and (7x7)] are developed. Curve E through H are measured on the surface that has gone through more complicated treatments. Curve E is obtained from a surface annealed to 442 K for 2 min after 160 L oxygen exposure at 300 K, curve F is from a surface with 180 L exposure at 350 K where only the (7x7) is observed with LEED, G is measured from a surface with 180 L exposure at 225 K where only NiO(111) is observed with LEED, and H is from the measurement of a surface annealed to 500 K after 500 L exposure at 300 K where only

Figure 37. Ni-L_3VV Auger line.

(A) For clean Ni(100) measured at 300 K.

(B) For surface exposed to 1.5 L oxygen at 300 K, measured at 300 K.

(C) For surface exposed to 50 L oxygen at 300 K, measured at 300 K.

(D) For surface exposed to 122.0 L oxygen at 300K, measured at 300 K.

(E) For surface annealed to 442 K after exposed to 160.0 L oxygen at 300 K, measured at 300 K.

(F) For surface exposed to 180.0 L oxygen at 350 K, measured at 350 K.

(G) For surface exposed to 180.0 L oxygen at 225 K, measured at 225 K.

(H) For surface annealed long enough at 500 K, after 500 L exposure at 300 K.

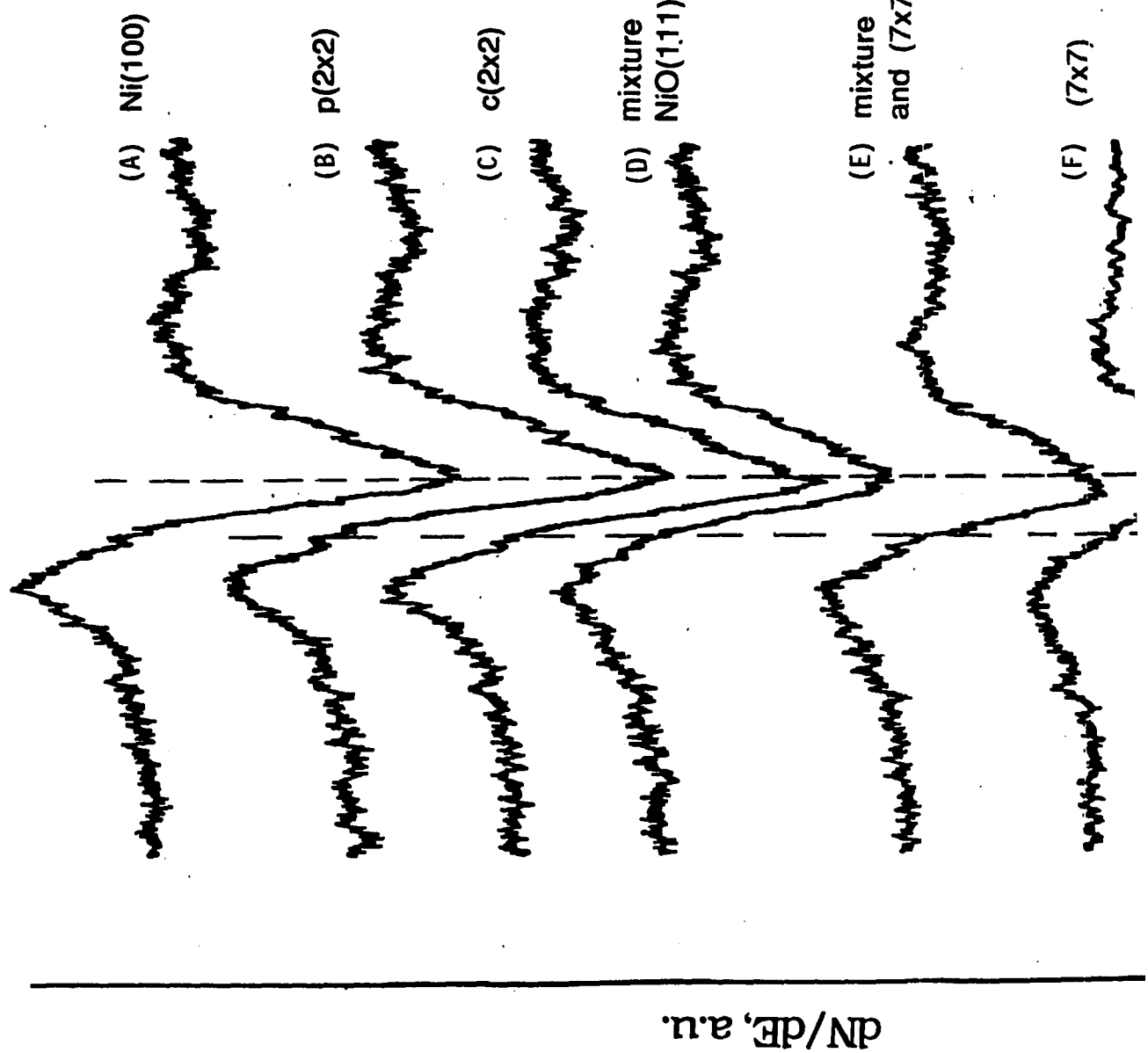
(A) Ni(100)
(B) p(2x2)
(C) c(2x2)
(D) mixture of c(2x2), NiO(111) and (7x7)
(E) mixture of NiO(111) and (7x7)
(F) (7x7)
dN/dE, a.u.

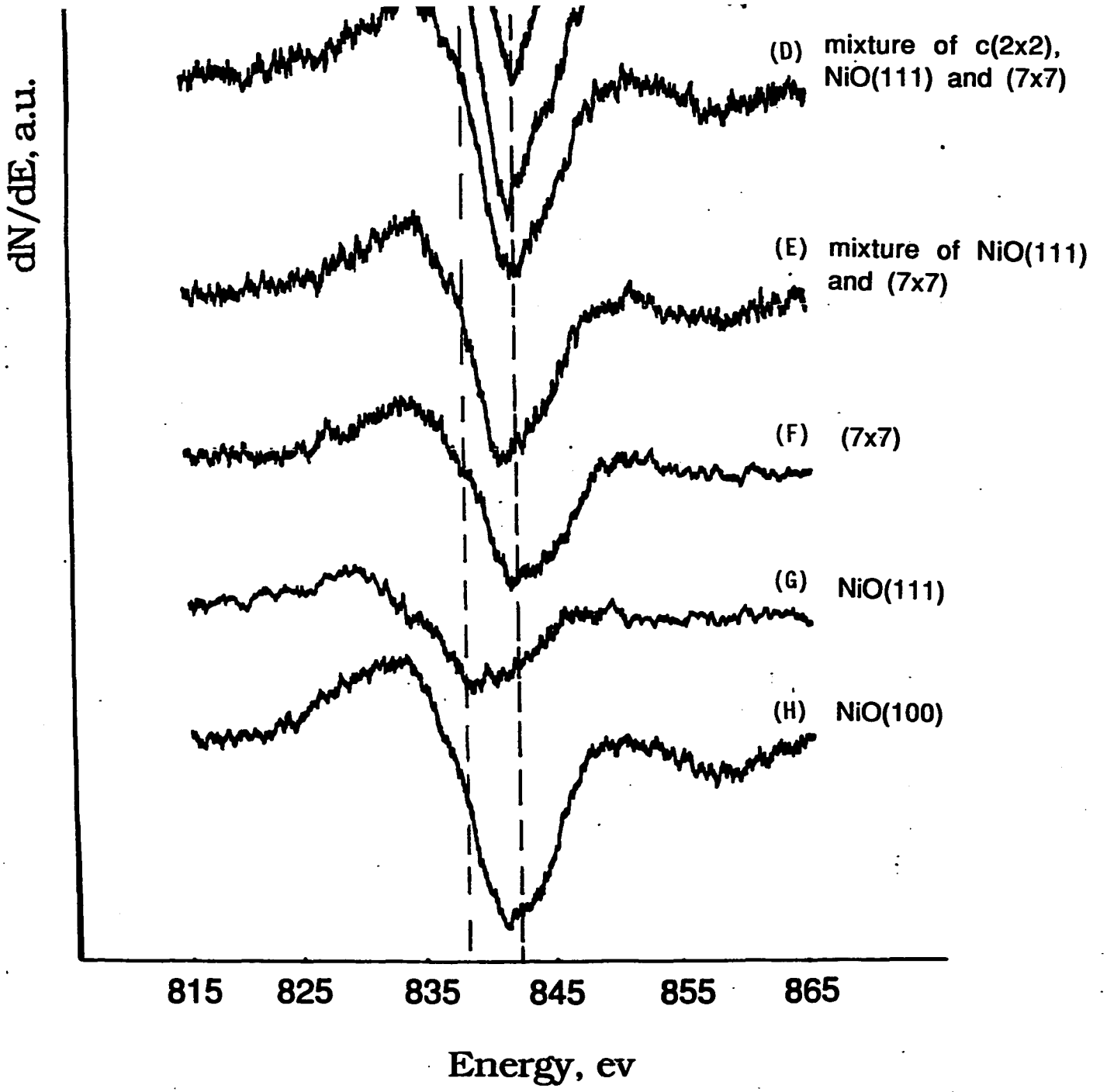
dN/dE, a.u.
(D) mixture of c(2x2), NiO(111) and (7x7)
(E) mixture of NiO(111) and (7x7)
(F) (7x7)
(G) NiO(111)
(H) NiO(100)
815
825
835
845
855
865
Energy, ev

NiO(100) and the reappeared c(2x2) are observed with LEED. Therefore curve h represents the L_3VV line of true NiO(100).

Discussion

From the results shown in Figures 37, 38 and 39, we can state the following observations: First, in the Ni-L_3VV lines in Fig. 37 NiO(111) structure shows a large chemical shift, $\delta E=3\pm0.5$ eV, as shown in curve G. However, the Auger measurement of (7x7) resembles that of NiO(100), both in the lineshape and in peak position (as shown in curves F and H). As we know chemical shift in AES are usually due to formation of chemical bond (charge transfer), which usually causes a shift of energy of a core level. The change in the energy of a core level, in turn, shifts the energy of Auger peak involving this core level [53]. Therefore the energy shift on NiO(111), which is not common on (7x7), nor on NiO(100), reflects that the chemical bonding of Ni-O in NiO(111) must be distinctive from that of (7x7) and NiO(100). Second, in the Ni-$L_3M_{23}V$ lines of Fig. 38, the known oxide epitaxy NiO(111) differs from that of (7x7) and NiO(100), both in peak position and in lineshape as shown by comparing curve G with F and H. Because the changes in the peak shape of WXY transition usually reflect variations of the electronic states of the valence electrons, the large difference in line shape shown in Fig. 38G from F and H, and the similarity between F and H, indicate the electronic structure of NiO(111) is different from that of NiO(100) or (7x7), while the latter two are similar. Third, the Ni-$M_{23}VV$ Auger lines in Fig. 39

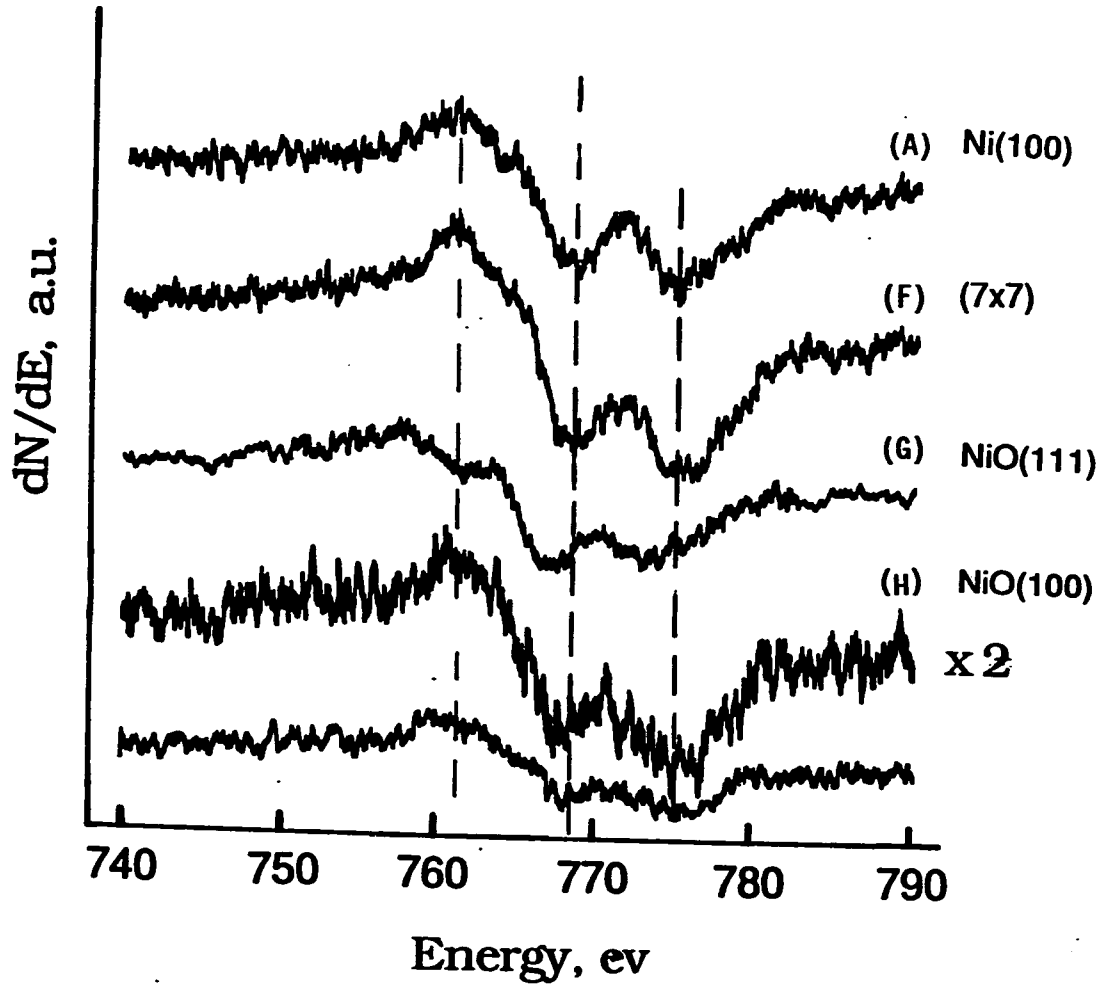

Figure 38. Ni-$L_3M_{23}M_{45}$. Conditions are all the same as in Fig. 37 for curves A, F, G and H.

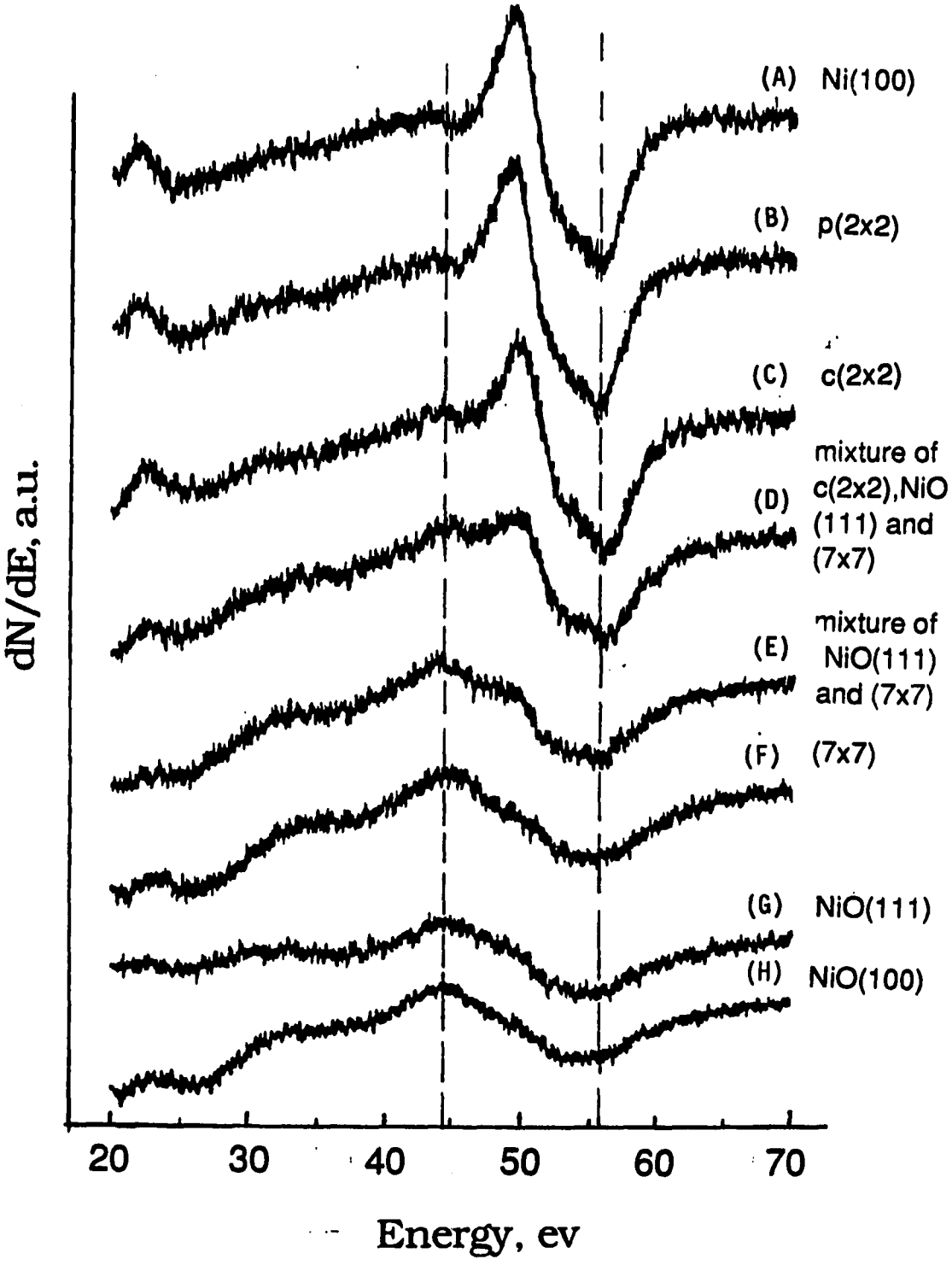

Figure 39. Ni-$M_{23}VV$. Conditions are all the same as in Fig. 37 for curves with the same label as those in Fig. 37.

show that as the clean surface goes through chemisorption to oxidation, a shoulder on the lower energy side develops. It is known that broadening of peaks shown in the low energy Auger lines is characteristics of metal oxide formation [59]. Since this shoulder (broadening) is common to all three structures associated with oxidation, NiO(111), NiO(100) and (7x7), it evidences that (7x7) is indeed an oxide formed during oxygen adsorption.

The above observations probably indicate that the (7x7) is very similar, within the sensitivity of the Auger measurment, to regular NiO(100) in both the electronic configuration and lattice geometry, while NiO(111) is different. Although analyses of AES results is usually difficult, because the valence levels lie in a relatively broad band of energy level for which the energy locations and DOS distributions can change greatly with chemical change (such as bond formation between nickel and oxygen atoms), the large chemical shift shown in NiO(111) is explained in the following. The general trend of down shift of Auger energy as oxygen exposure increases is due to the fact that the electronegative oxygen pulls electrons away from Ni atoms. The results from tight-binding calculation by Mukherjee [60] and Altmann [61] et al. show that with increasing coverage from p(2x2) to c(2x2), the nickel to oxygen charge transfer increases from 0.8e to 1.0e. Note, in the NiO compound, the transferred electronic charge to oxygen amounts to 2.0e. The fact that the Auger energy of NiO(111) shifts down more than that of the (7x7) and NiO(100) might be explained by the structure differences between them. Fig. 40 schematically shows the side and top views of

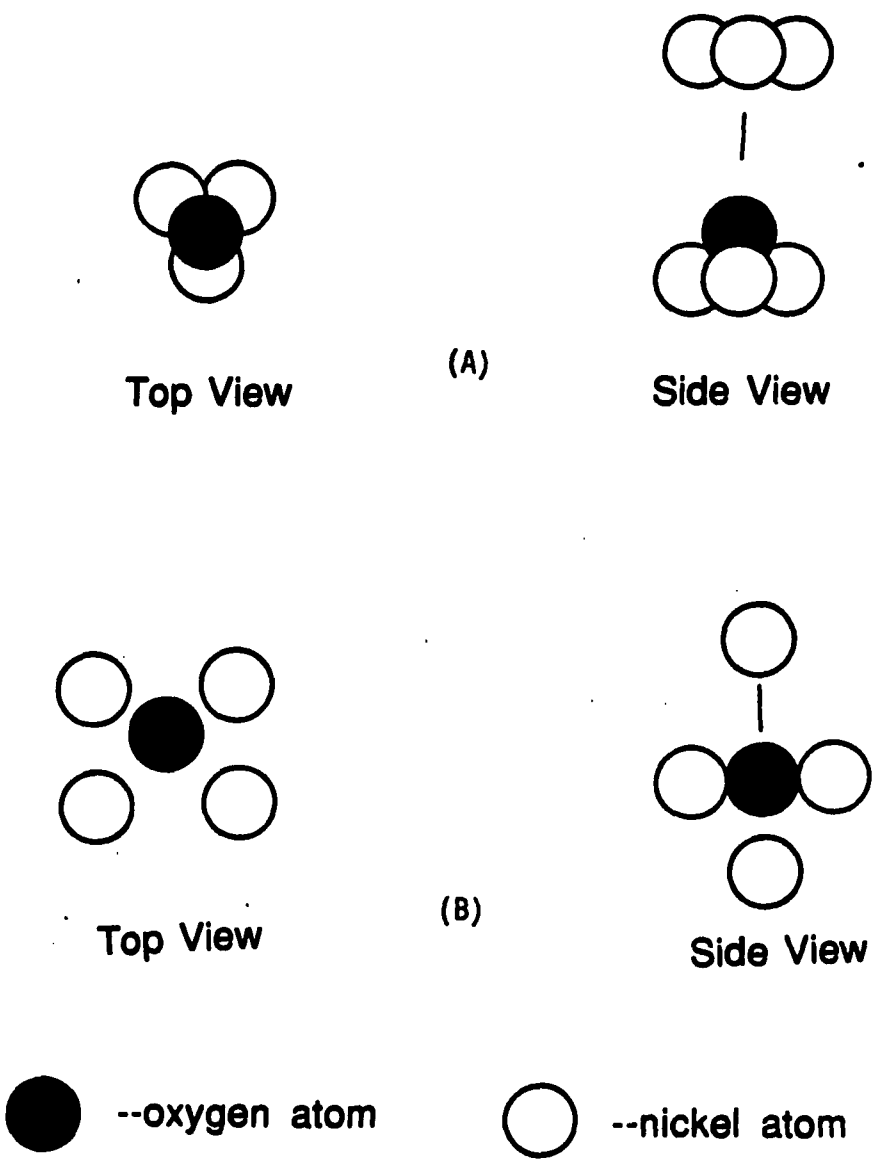

Figure 40. Atomic arrangement of NiO(111) and NiO(100) at the surface with top and side views. (A) NiO(111), (B) NiO(100).

NiO(111) epitaxy and the NiO(100) structure. In NiO(111) structure, the bulk oxygen atoms have Coordination Number (CN) = 6 with Ni-O distances all the same, 2.9536 Å (where 2.9536 Å = $a/\sqrt{2}$, a = 4.177 Å, lattice constant of NiO). But the oxygen atoms terminated at the surface only bond to three nearest Ni atoms underneath it. In NiO(100) structure, oxygen also has CN=6 in the bulk, but Ni-O distances are 2.9536 Å for the four coplanar Ni atoms and 2.08 Å for the other two Ni atoms, one above and one below the oxygen atom (where 2.08 Å = a/2, a = lattice constant of NiO). The oxygen atoms in the top most layer bond to five nearest Ni atoms. In other words, the surface oxygen loses three bonds to nickel in NiO(111), as shown in Fig. 40A, and only one bond in NiO(100), as shown in Fig. 40B. Therefore, we postulate here, the electron density will be pulled more toward oxygen in NiO(111) than in NiO(100) in order to have the electron density balanced.

Also, notice in Figs. 37 and 39 that A, B and C are basically the same, indicating that the chemical environment of surface Ni atoms does not change much when chemisorption structures p(2x2) and c(2x2) are formed, which is consistent with the experimental studies by others with LEED [62], elastic He scattering [80], SEELFS [63], EELS [64,65], UV and XPS [10] and ion backscattering [66], although theoretical studies have reported various values of spacing between oxygen adlayer and Ni first layer for p(2x2) and c(2x2) structures [67].

In Fig. 41, Auger lines of Ni-$M_{23}VV$, corresponding to surfaces with different annealing history are put together in order to study the kinetics of the formation of NiO(100). In this figure, curve A is for

Figure 41. Ni-$M_{23}VV$ Auger lines of surfaces with different annealing history.

(A) Clean Ni(100).

(E) Obtained after heated surface to 442 K for 2 min after 160 L oxygen exposure at 300 K.

(I) Obtained after briefly annealed surface to 652 K after 400 L exposure at 400 K.

(H) Obtained after annealed surface to 500 K for long enough after 500 L adsorption at 300 K until NiO(100) is the only epitaxy observed with LEED.

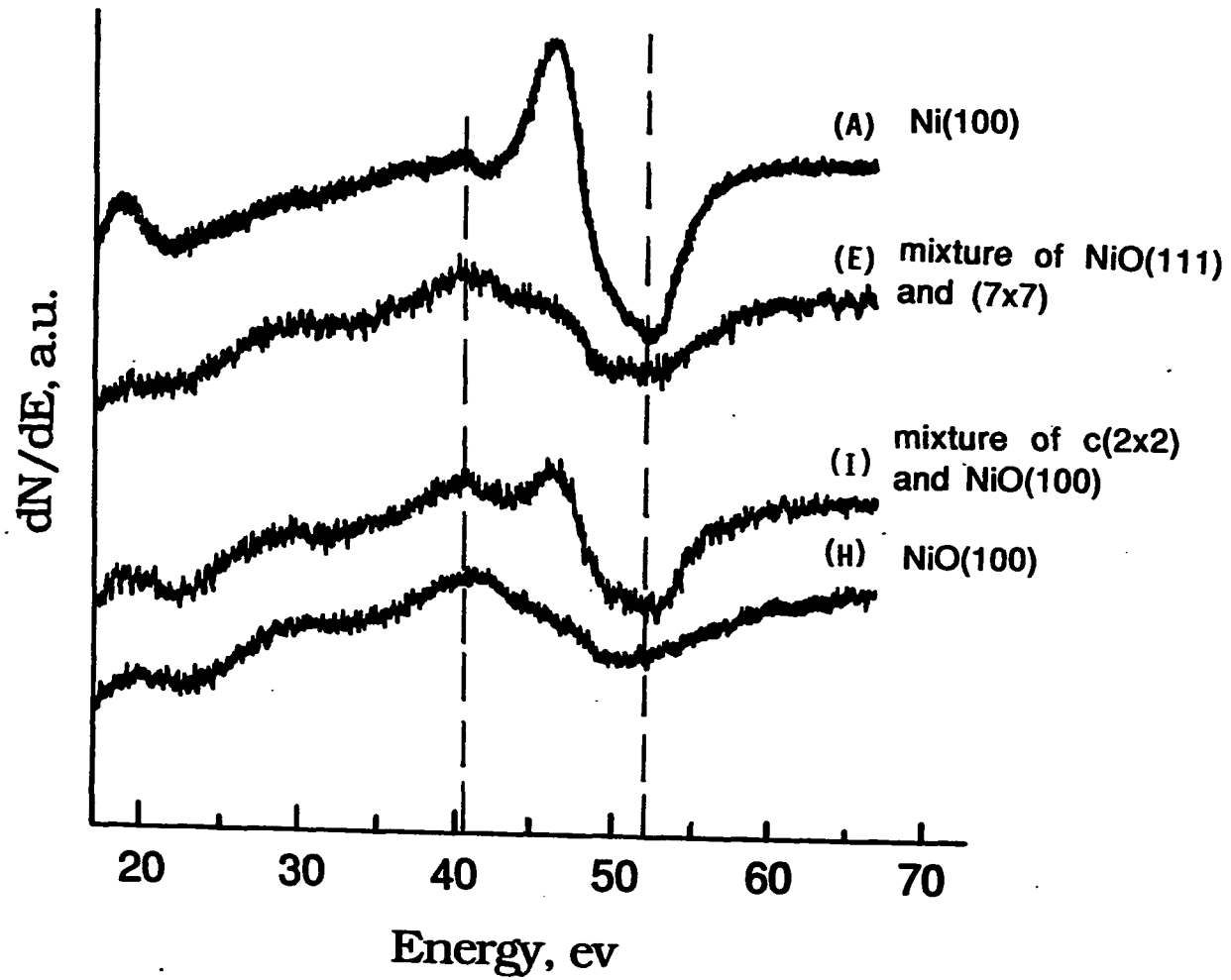
dN/dE, a.u.
(A) Ni(100)
(E) mixture of NiO(111) and (7x7)
(I) mixture of c(2x2) and NiO(100)
(H) NiO(100)
20
30
40
50
60
70
Energy, ev

clean Ni, E is obtained after heated surface to 442 K for 2 min after 160 L oxygen exposure at 300 K, I is obtained after briefly annealed surface to 652 K after 400 L exposure at 400 K, and H is obtained after annealed surface to 500 K for long enough after 500 L adsorption at 300 K until NiO(100) is the only oxide epitaxy observed on the LEED screen. Therefore, curve H is the true oxide Auger line. It appears from both the Auger peak positions and the lineshapes that curves E and I are convolutions of atomic (curve A) and oxide (curve H) Auger characters, assuming the clean Ni(100) gives atomic Auger character and true NiO(100) gives oxide Auger character. From the results in Chapter 1, we know that curve E is measured on the surface with the coexistence of Ni(111) and (7x7). Therefore the atomic Auger feature on curve E indicates either the NiO layer is not thick enough so that the substrate Ni atoms are within the measurable depth of AES, or the NiO forms islands (not uniform layers) so that Ni atoms that are not covered by these islands are exposed to the AES. The former hypothesis supports the idea that the oxide structure saturates with limited thickness. Since the electron escaping depth is $\leq$ 10 Å at 50-60 eV for the $M_{23}VV$ Auger line, the NiO must be $\leq$ 2-3 layers thick. The latter suggests either NiO(111) or (7x7) or perhaps both forms oxide island. The uncovered Ni(100) between islands contributes to the atomic nickel feature in Fig. 41E. The discussion made in Chapter 2, where we attribute the unexpected high (0,1) spot intensity in the profiles to the contribution from uncovered metallic Ni(100), is consistent with this hypothesis. The increased atomic nickel feature on curve I indicates the reappearance of metallic

Ni at temperatures above 640 K. This is consistent with the discussion in Chapter 1 about the disproportionation of NiO during annealing. The less oxygen-rich phase consists of reappeared metallic Ni and p(2x2) or c(2x2) structures.

Second, on curve E in Fig. 41, the remnant atomic Ni feature is due to uncovered Ni(100), while the atomic Ni feature on curve I is due to reappearance of metallic Ni during annealing. In order to check whether this reemerging Ni-$M_{23}VV$ peak from annealing, at 55.7 eV, is indeed the same atomic Ni character as that shown in the clean Ni(100) Auger line of curve A, first, we measured the I-V curves of the (1/2,1/2) spot before and after annealing (as shown in Fig. 42). The measurement of intensity vs. incident electron energy usually reflects the structural information of lattice in 3-dimension. Dynematic diffraction information such as the multiple scattering effect, inelastic diffraction, etc., occurs in the I-V spectra as secondary Bragg peaks. Analysis and comparison of measured and calculated I-V spectra could result in 3-dimensional structural determination. But even from simple comparison of the resemblance of measured I-V spectra for the chemisorption structures before and after annealing, we should be able to draw some conclusions about the similarities and differences of the two structures. It is evident in Fig. 42 that no major differences are observed from our measurements for the c(2x2) patterns obtained by adsorption and anneal of the adsorbed surface. Second, the continued oxygen exposure to the annealed surface with either p(2x2) or c(2x2) patterns will bring back the NiO(111) structure again at 300 K and below. These indicate that the reemerging

Figure 42. Experimental I-V curves of c(2x2) structure, obtained before and after annealing.

(A) Obtained after adsorption of O_2 at 300 K with pressure 3.2×10^{-8} for a total of 14 L, a single phase c(2x2) is observed with LEED. Measured at room temperature.

(B) Obtained after 43 L O_2 exposure at 200 K and then annealed to 662 K, measured at room temperature.

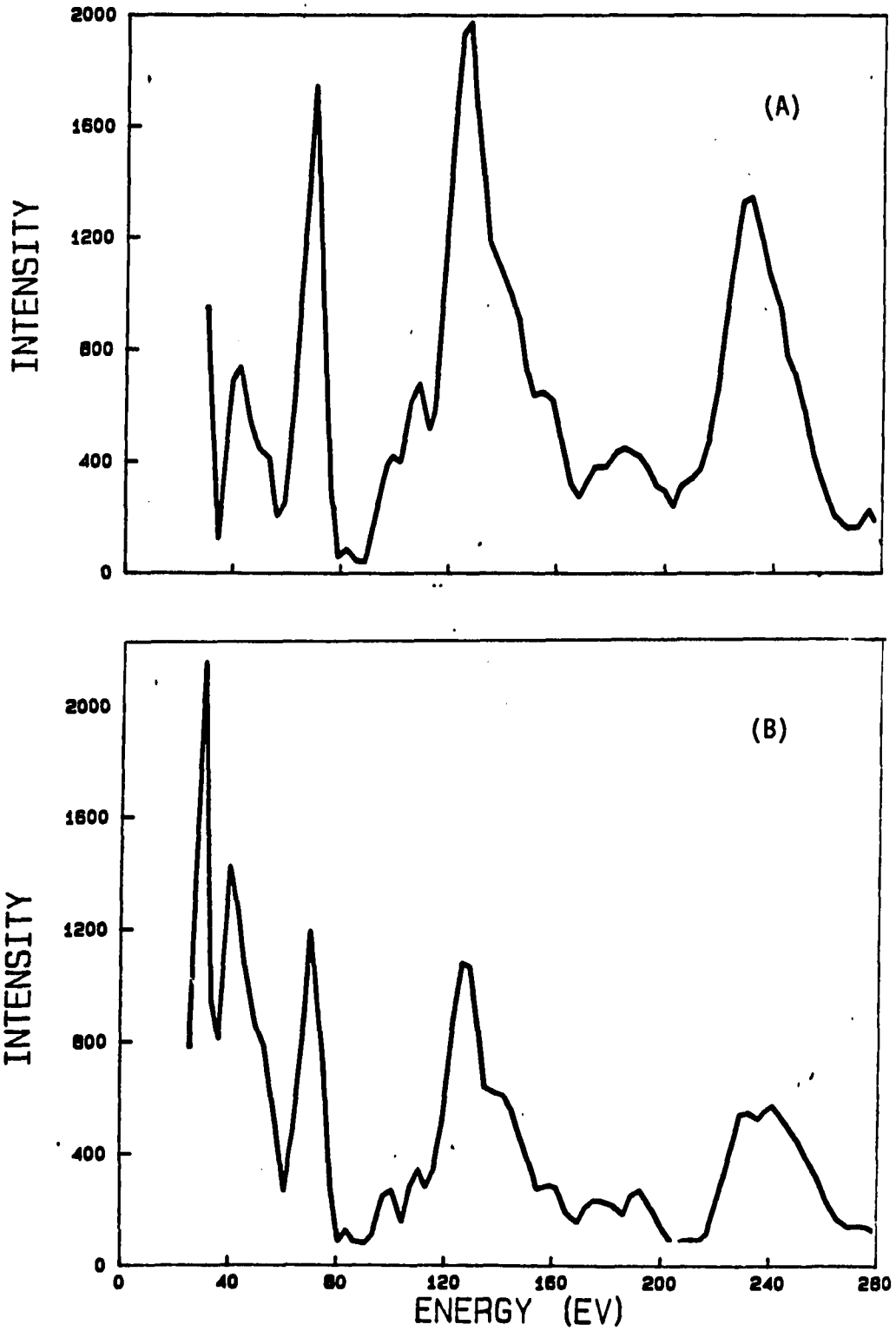
(A)
(B)
INTENSITY
INTENSITY
2000
1600
1200
800
400
0
0
40
80
120
160
200
240
280
ENERGY (EV)

metallic nickel and c(2x2) or p(2x2) structures are indeed the same as clean and chemisorption structures. These post-annealing oxygen atoms sit on the surface the same way as before annealing.

The conclusions we can draw from these AES studies are:

1. In Chapter 1, from the common distinct shape of AES signal ratio vs. exposure curves over 80-400 K, we conclude that the (7x7), together with NiO(111), should be a new nickel oxide phase. From the AES results presented in this chapter we can conclude that (7x7) is indeed a nickel oxide developed on Ni(100) during adsorption, based on the shoulder which appears on the Ni-$M_{23}VV$ lines in Figure 39. This shoulder is common to NiO(100), NiO(111) and (7x7).

2. Auger measurements show substantial differences between two epitaxies, NiO(111) and NiO(100), and great resemblance in line shape and peak positions between (7x7) and NiO(100). It indicates that (7x7) must have pretty much the same electronic and geometric structures as NiO(100). The proposed anti-phase wall model for the observed (7x7) has somewhat the same lattice unit cell and surface orientation as NiO(100) except the 1.5% contraction and the large numbers of anti-phase walls.

3. The hypothesis made in Chapter 1 about the disproportionation of NiO layer upon annealing is confirmed here by the reappearing atomic Ni feature in the Ni- $M_{23}VV$ Auger line after annealing. The reappearing Ni and p(2x2) or c(2x2) structures have no difference from the clean Ni(100) and chemisorption structures as compared by I-V measurement.

CHAPTER 4: MEASUREMENTS OF DEBYE-WALLER FACTORS OF NiO

Results

The interest in finding the Debye-Waller factor and Debye temperature is three fold. First, low-energy electron diffraction is potentially the primary tool to study surface lattice dynamics. Our computer-interfaced video LEED system has not been employed in studying this aspect of the surface property. We would like to find out whether reasonably good results can be obtained with our equipment. Second, there have not been many reports about the surface Debye temperature of nickel oxide, although there are determination of the Debye temperature of metal nickel surface and that of qualitative estimation of NiO [68]. They estimate the Debye temperature of NiO(100) must be very high because as they heated the oxygen covered Ni(100) surface up to 900 K, the broad NiO(100) diffraction spots remained intense. Therefore they estimated from this qualitative observation that the surface Debye temperature for NiO(100) is at least 800 K. Third, the surface Debye temperature is an important parameter in LEED dynamical calculations [69]. Any future structural determination by this method will require a value of the surface Debye temperature in order to obtain a successful result. In this chapter we quantitatively estimate the Debye-Waller factor and surface Debye temperatures of nickel oxide NiO(111) and NiO(100).

It is well known that there is a fall in the intensity of the beams

in an x-ray diffraction experiment (using a bulk single crystal) as the crystal temperature is raised. At the same time the intensity in the diffuse background of the diffracton pattern becomes higher. The simplest explanation of these observations is that the individual atoms of the crystal are vibrating independently about their equilibrium positions and, as a result, the exact Bragg condition is not met. This is because waves which would be scattered coherently from a perfectly rigid lattice actually have phase differences fluctuating with time due to the motion of the scatterers. The effect of this motion upon the intensity of the elastically diffracted beams is described in many solid state physics textbooks, e.g., Ashcroft and Mermin, 1976 and Kittel, 1986. If I_o is the intensity elastically scattered into a beam by a rigid lattice, then the temperature dependence of diffraction intensity is described kinematically by a factor [53,70]:

$$\exp[-\langle s \cdot u\rangle^2] \qquad (4.1)$$

which is a measure of the component of $\langle u^2\rangle$, the atomic mean square displacement, in the direction of s. The exponential factor of eq. (4.1) is usually called the Debye-Waller factor and is often written as exp(-2MT). By using the Debye model of the solid, assuming $T \gg \theta_D$ and $\langle u^2\rangle$ is proportional to the temperature, we have

$$s^2\langle u^2\rangle = 2MT \qquad (4.2)$$

Therefore, by plotting ln I vs. T in the high temperature limit, the slope gives the result of 2M.

However, previous experimental and theoretical studies on other f.c.c. and b.c.c. single crystal surfaces have shown that actually at

temperatures below about one-third of the bulk θ_D, the linearity of Debye-Waller factor in the plot of ln I vs. temperature still persists [35,71-73], i.e., the requirement of $T>>\theta_D$ can be relaxed.

NiO(111) does not show obvious degradation over repeated heating-cooling cycles if the maximum temperature is kept below 425±25 K. Therefore, the heating ramps for NiO(111) have to be limited to the range 80-425 K, where 80 K is the lower physical limit because the crystal is cooled with liquid nitrogen. This range is relatively narrow, compared with typical temperature ranges used for this kind of studies. It will be interesting to find out the lowest temperature where the linearity of Debye-Waller factor still holds. For the NiO(100) phase, the intensity vs. temperature is measured in the 80-650 K temperature range.

Discussions of the possible different ways to measure 2M and their sources of error will be presented in this chapter, then measurements of diffraction intensity vs. temperature will be presented, and finally information about surface and bulk Debye temperature, and the mean square amplitude of vibration at the surface will be extracted.

The fast computer image processing ability of our system allows us to integrate spot intensity over a window set around the spot or to obtain the intensity profile of a single slice across the spot rapidly as temperature changes. A typical heating-cooling cycle takes less than 20 min. However, the thermal expansion of the lattice during heating, can cause intensity change, i.e., spot intensity change measured at a fixed energy during a continuous heating may not be only due to temperature damping. The in-phase and out of phase diffraction condition

changes as temperature due to thermal expansion. The intensity change due to heating is especially obvious in regions where intensity changes rapidly with beam energy. This can be more easily explained in an intensity vs. energy measurement at different temperatures, where the maximas in the I-V curve should shift down as temperature increases [74]. Therefore it is best to follow the peak as it shifts to determine the intensity used in plotting ln I vs. T. But it is very time consuming to measure the I-V curves over a wide temperature range. Another procedure which should be followed is to measure the spot profile intensities while heating so that the constancy of the FWHM, as is required for an analysis of temperature dependence in terms of Debye-Waller factor [74], can be checked.

However, the intensity vs. temperature is measured under a somewhat relaxed condition in this study. It will be interesting to see how accurate our results can be, comparing with results of other methods [if any]. The I(T) is measured at a fixed energy and during continuous heating. In order to check how the Debye-Waller factor fluctuates as energy, we measure I(T) at six different energies over the range 57-156 ev. To avoid the effect of island ordering and disordering during heating, the sample is heated to a high temperature before data are taken. Presumably, as long as the heatings thereafter do not go beyond that upper limit temperature, the intensity changes during the heatings, following the first one, should be predominantly due to the Debye-Waller effect, and intensity should be reversible as the sample is heated and cooled, assuming no phase transition or oxygen dissolution in this

Figure 43. Typical sequential heating-cooling curve and integrated spot Intensity changes during heating-cooling cycles.
(A) Obtained from the first heating-cooling cycle immediately after 32 L oxygen exposure at 200 K, measured at 87 eV. Note the x-axis in this panel is different from all the others.
(B) Obtained from the second heating-cooling cycle after (A), measured at 57 eV.
(C) Obtained from the third heating-cooling cycle after (B), measured at 127 eV.
(D) Obtained from the 4th heating-cooling cycle after (C), measured at 156 eV.
(E) Obtained from the 5th heating-cooling cycle after (D), measured at 107 eV.
(F) Obtained from the 6th heating-cooling cycle after (E), measured at 72 eV.

Temperature, K
0
100
200
300
400
0
200
400
600
Time, sec

Intensity, a.u.
0
100
200
300
0
400
800
(A)
Intensity, a.u.
50
100
150
200
(B)
40
80
(D)
40
80
120
(E)

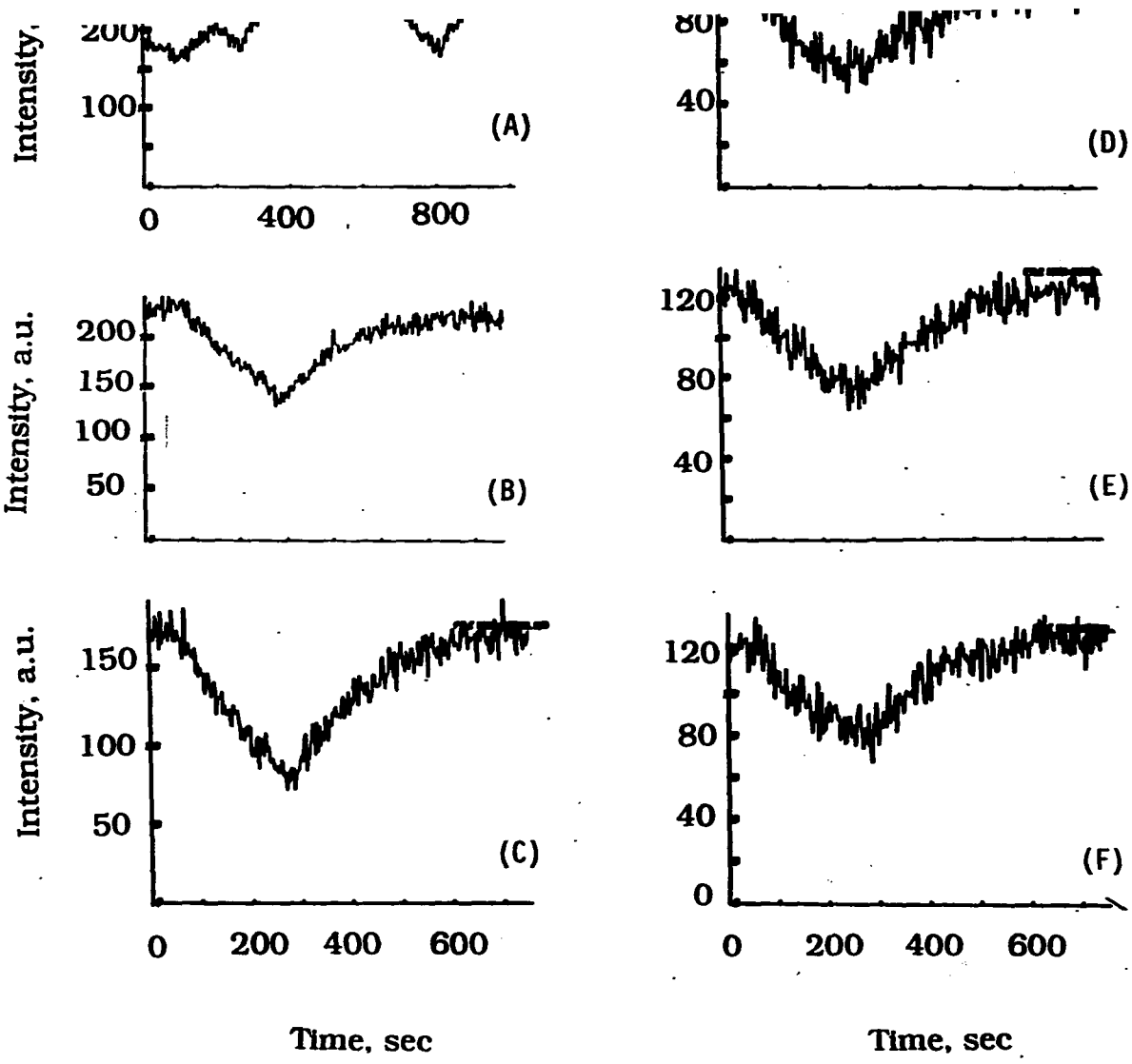
Intensity,
200
100
(A)
0
400
800
80
40
(D)
Intensity, a.u.
200
150
100
50
(B)
120
80
40
(E)
Intensity, a.u.
150
100
50
(C)
0
200
400
600
120
80
40
0
(F)
0
200
400
600
Time, sec
Time, sec

temperature range. Indeed, in Fig. 43 we show the intensity changes during sequential heating and cooling cycles at six different beam energies. A typical sequential heating-cooling curve, T(t), is also shown in this figure. Fig. 43A shows the result from first annealing immediately after 32 L oxygen exposure at 200 K. It gives much different curve shapes from all the other annealing treatments, as shown in Fig. 43B, C, D, E and F. As a matter of fact, when attempting to plot ln I(T) for Fig. 43A, very poor linear regression is obtained from the heating part, as shown in Fig. 44A, but if the cooling part curve is put in the same graph, a very good linear relationship is obtained, as shown in Fig. 44B. In Fig. 44A the initial decrease below 180 K is perhaps due to massive diffusion of oxygen atoms that have been trapped at some unstable adsorption site at low temperature. The increase following that indicates that the ordering of NiO(111) domains is dominant in the 180 K to 300 K range. The second decrease starting above 300 K is mainly due to the Debye-Waller effect, which is indicated by its overlap with the ln I(T) during cooling. We also check the reversibility of intensity for other heating-cooling cycles to make sure the change in intensity is truly a temperature effect, rather than dissolution or phase transition. This is shown in Fig. 45, which shows ln I(T) of a heat-cool cycle at 127 eV. The reversibility of intensity is obvious. The temperature measurement is through a W-5%Re/W-26%Re thermocouple mounted on the back of the Ni(100) sample, output both to a DVM, and an X- Y recorder as the integrated LEED spot intensities are recorded simultaneously by computer [38]. The temperature accuracy is estimated to be $\pm$1 K, based on the DVM

Figure 44. LnI vs. T from the sequential heating-cooling results of Fig. 43A.

(A) Ln I(T) from heating process.

(B) Overlap of ln I(T) from both heating and cooling process.

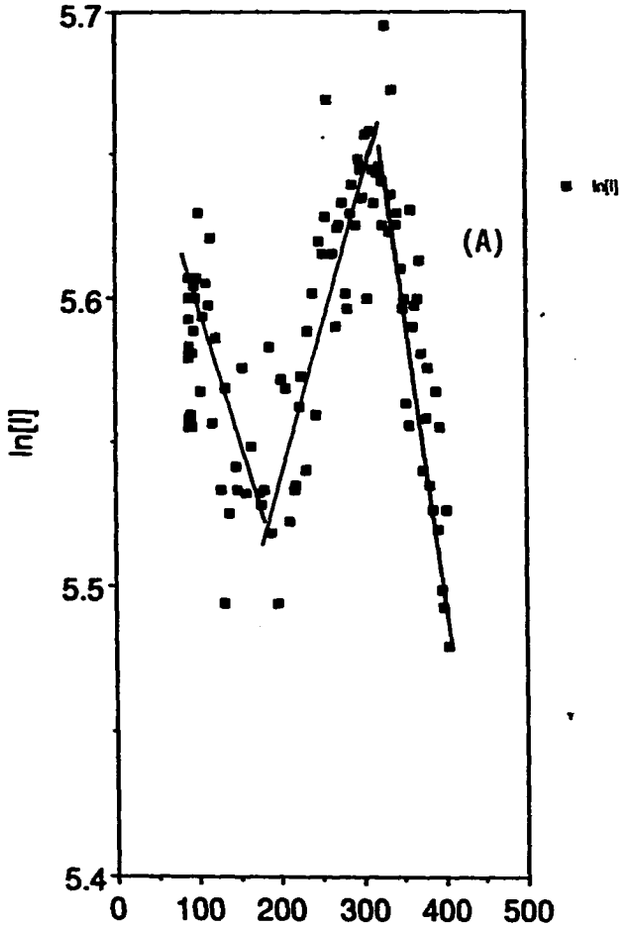
5.7
5.6
5.5
5.4
ln[I]
(A)
ln[I]
0
100
200
300
400
500
T, K

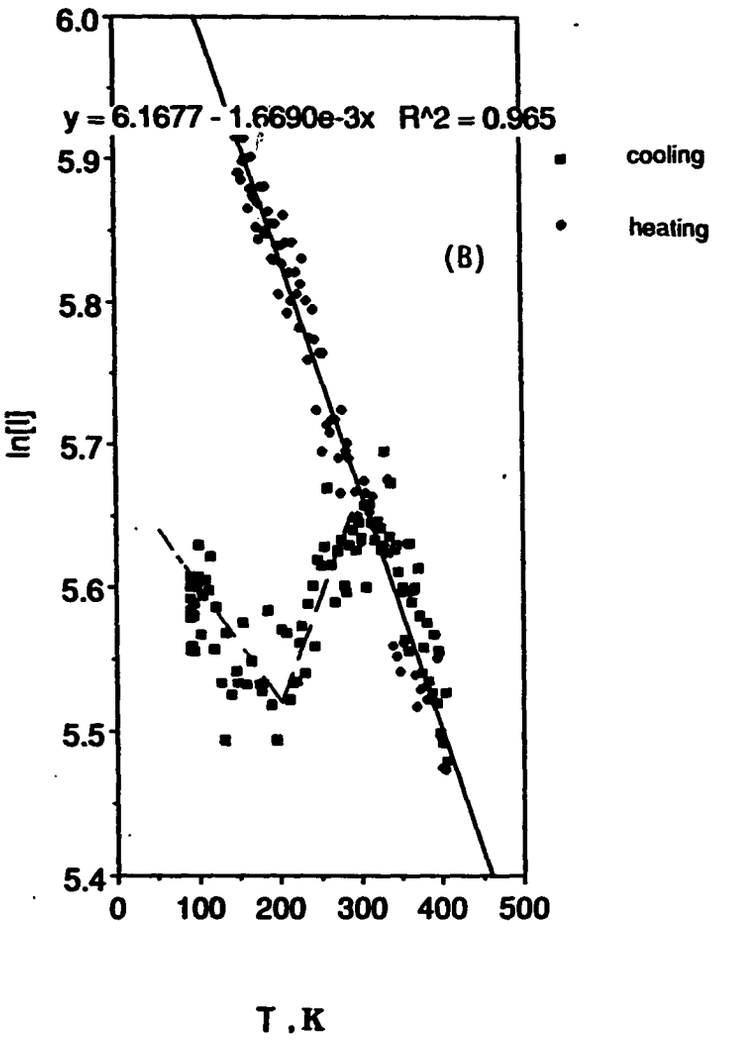
6.0
5.9
5.8
5.7
5.6
5.5
5.4
ln[I]
y = 6.1677 - 1.6690e-3x R^2 = 0.965
(B)
cooling
heating
0
100
200
300
400
500
T, K

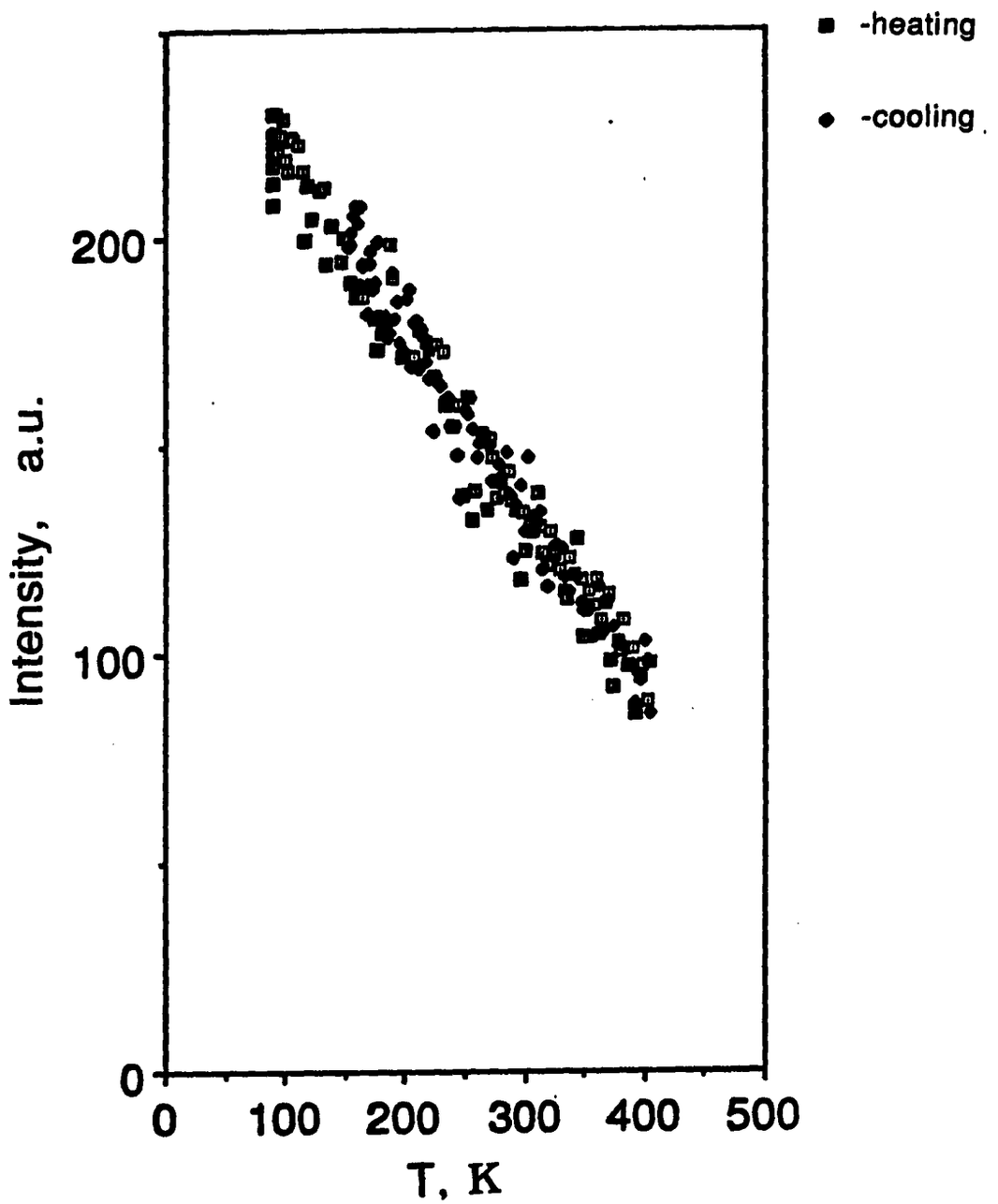

Figure 45. Showing that good reversibility of I(T) are maintained for those heat/cool cycles of Fig. 43. Data shown here reflect the I(T) of Fig. 43C, measured at 127 eV.

reading which is accurate to ±0.01 mV. The Herz temperature controller is used to obtain the linear heating slope [41]. Fig. 46 shows ln I(T) corresponding to the measurements in Fig. 43 for NiO(111) epitaxy during heating. Fig. 46A through E are put in sequential order as they are taken. The heating is only up to 423 K so that no apparent NiO(100) forms within this temperature range.

The increasing scatter in ln I(T) is obvious, as shown in Fig. 46A through E, due to repeated heatings. Slight and gradual degradation of NiO(111) is resulted from repeated heatings. That causes the increase in background noise relative to spot intensity. Deviations from constant slope occurs at low temperature, which is usually attributed to the zero point motion, and at high temperature where the measurements include diffuse scattering [35, 75]. The least square curve fittings are also shown in the figure. The 2M values obtained from plotting ln I(T) are listed in Table 1, where we also list results of simultaneous measurement on another "ring" spot in order to check the variation of the 2M values.

In Table 1, the 2M values show fluctuation with energy by a factor of 3 and with different spots by a factor of 1.5. It is hard to say whether this fluctuation indeed reflects the variation of electron penetration depth at different incident beam energy, because electron energies around 100eV ± 50eV have about the same mean free path. Therefore it is not conclusive from Table 1 to say that different electron penetration depths at different energies cause the variation in 2M. Also, because the intensity of NiO(111) after subtracting the relatively high background, due to either disordered adsorbate at surface

Figure 46. Plot of lnI vs. T for results of Fig. 43B through F. Least square curve fittings are also shown in each panel.

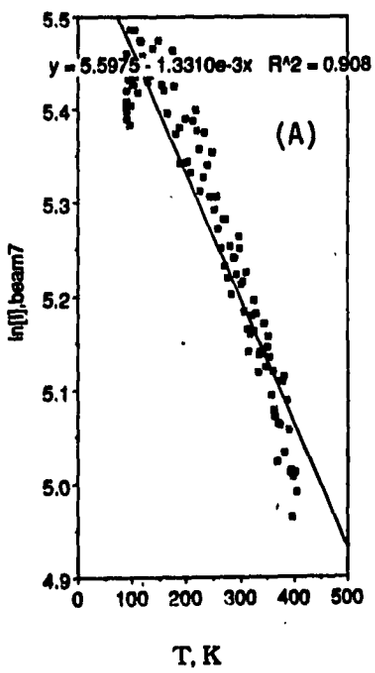
y = 5.5975 - 1.3310e-3x R^2 = 0.908
(A)
ln[I],beam7
T, K

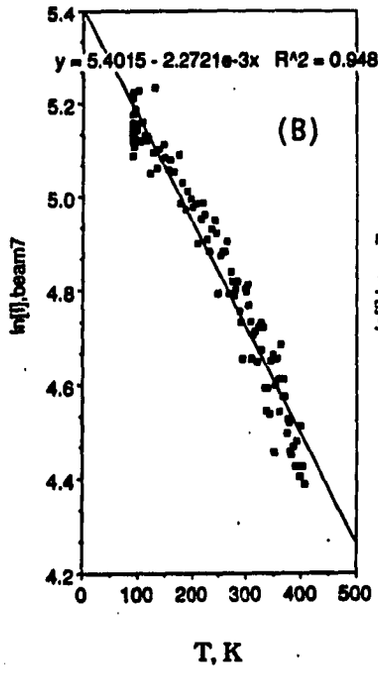
y = 5.4015 - 2.2721e-3x R^2 = 0.948
(B)
ln[I],beam7
T, K

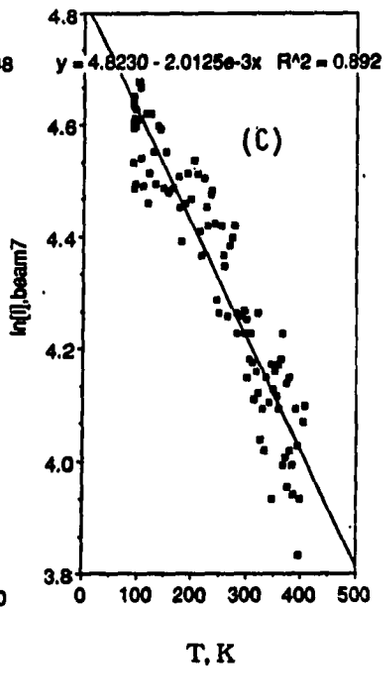
y = 4.8230 - 2.0125e-3x R^2 = 0.892
(C)
ln[I],beam7
T, K

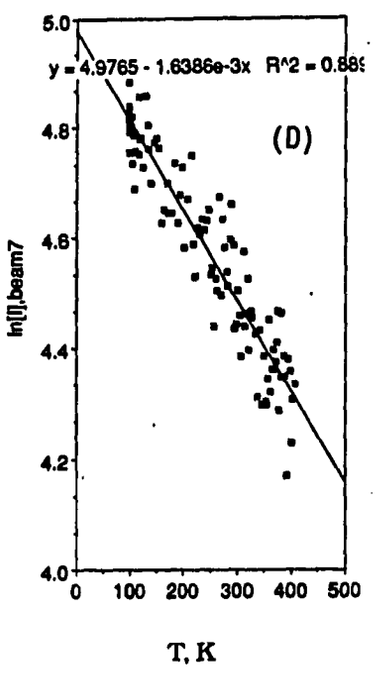
y = 4.9765 - 1.6386e-3x R^2 = 0.88
(D)
ln[I],beam7
T, K

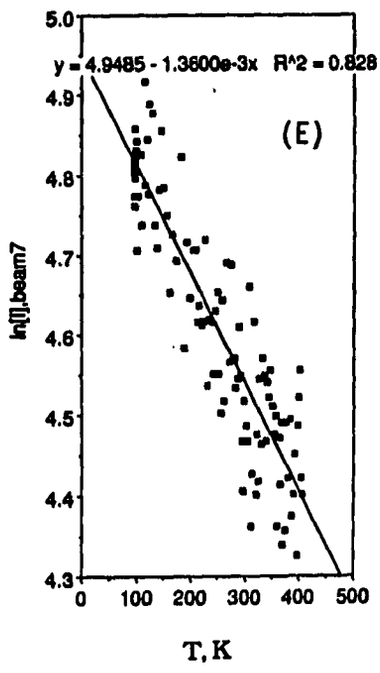
y = 4.9485 - 1.3600e-3x R^2 = 0.828
(E)
ln[I],beam7
T, K

Table 1. Measured Debye-Waller factors and surface Debye temperatures of NiO(111)

beam energy	2M x 1000			θ_D, K		
	beam 7	beam 8		beam 7	beam 8	average
57 eV	1.3310	0.9965		336.0	396.5	366.0
72 eV	1.3600	1.1912		373.7	399.3	386.0
87 eV	1.6690	2.5999		370.8	297.1	334.0
107 eV	1.6386	2.0022		415.1	375.5	395.0
127 eV	2.2721	1.7985		384.0	431.6	407.0
156 eV	2.0125	2.9455		452.2	373.8	413.0
						average = 383 ± 29 K

Table 2. Measured Debye-Waller factors and surface Debye temperatures of NiO(100)

beam energy	2M x 1000		θ_D, K
64 eV	1.6803		317.0
72 eV	1.4386		363.3
			average = 340 ± 23 K

or disorder in the subsurface oxide region, is low and the temperature range, over which the sample is heated and cooled, is narrow, the drawing of the straight line for ln I(T) plot can be less definite, or arbitrary in a sense. Therefore the fluctuation of the 2M with energy and the spots measured is understandable. Fig. 47A is measured on the surface annealed to 574 K after exposed to 6 L at 130 K. Fig. 47B is obtained on the surface annealed to 607 K after exposed to 175 L oxygen at 225 K. The good linearity down to ~150 K is obvious in Fig. 47. The measured Debye-Waller factors for NiO(100) are listed in Table 2. The difference between NiO(111) and NiO(100) in 2M results are within the measurement scatter. Presumably because Debye-Waller effect is due to the lattice 3-dimensional, collective motion, it is not so sensitive to the surface differences of different epitaxies.

Another form of eq. (4.1) can be derived which relates the observed intensity to other measurable quantities:

$$I(T) = I(0)\exp\left\{-\frac{12h^2 (\cos\phi)^2 T}{m k_B \lambda^2 \theta_D^2}\right\} \qquad (4.3)$$

where λ is incident wavelength,

ϕ is entrance angle to normal incidence,

θ_D is the Debye temperature of the outermost layers where the low energy electrons penetrate,

h is Planck constant,

m is atomic weight,

k is Bolzmann constant,

Figure 47. Plot of lnI vs. T measurements on NiO(100).

(A) Obtained from heating of a surface exposed to 6 L oxygen at 130 K.

(B) Obtained from annealing of a surface exposed to 175 L oxygen at 225 K.

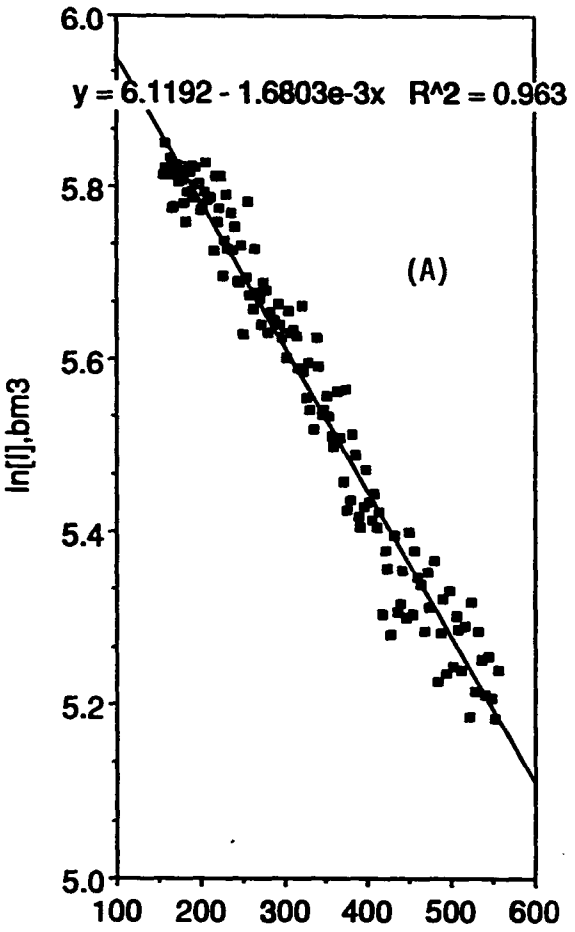
y = 6.1192 - 1.6803e-3x R^2 = 0.963
(A)
ln[I],bm3
6.0
5.8
5.6
5.4
5.2
5.0
100
200
300
400
500
600
T, K

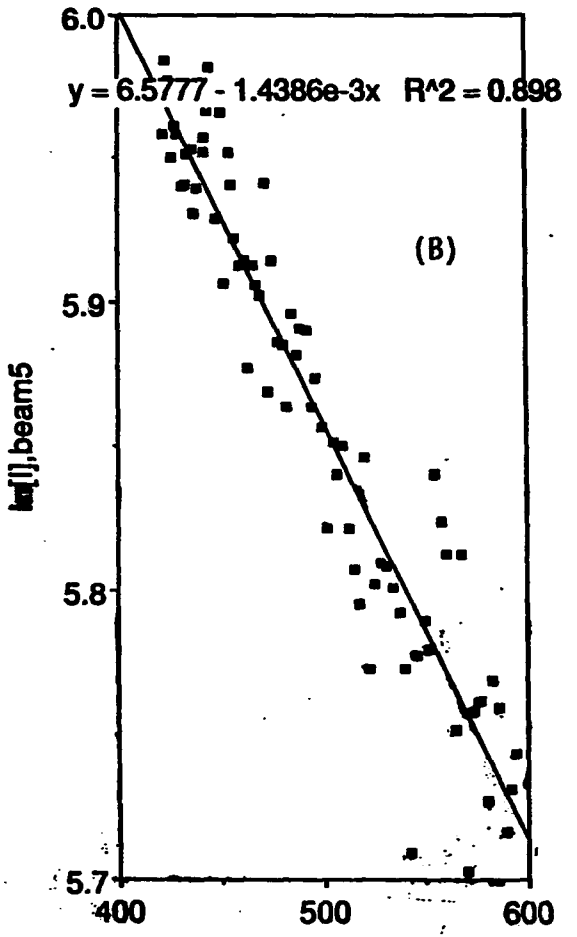
y = 6.5777 - 1.4386e-3x R^2 = 0.898
(B)
ln[I],beam5
6.0
5.9
5.8
5.7
400
500
600
T , K

surface Debye temperature is then obtained.

Discussion

The surface Debye temperature of NiO(111) and NiO(100) are listed in Tables 1 and 2 in the corresponding columns. In Table 1, the maximum range of error for the surface Debye temperature on the two spots from the two different domains of NiO(111) is about $\pm$40 K. The θ_D averaged over 6 measurements, over the 57-156 eV energy range, gives θ_D = 383 K, with standard deviation 29 K. The variation in measured θ_D more or less reflects the differences in electron penetration depth at different energy. Lower electron energy samples the outer layers, which usually have larger vibration amplitude. Therefore the Debye temperature is lower, i.e., the temperature damping on the spot intensity is stronger.

It is known that the mean square displacement of lattice points is related to the Debye temperature in the form [76,77]:

$$\langle u^2 \rangle = \frac{3 N h^2 T}{4 \pi^2 m k_B \theta_D^2} \qquad (4.4)$$

where

N=Avogadro's constant

h=Planck's constant

T=absolute temperature

m=atomic mass

k_B=Boltzmann's constant

θ_D=the effective Debye temperature

By using a nearest neighbor central force model for fcc metals, Wallis et al. have predicted the mean square displacement normal to the surface is twice the value of the bulk mean square displacement [71]. Experiments also show that of the surface is at least twice as large as that of bulk [78]. Therefore the bulk Debye temperature of NiO should be

$$\theta_{D(bulk)} = \theta_D\sqrt{2} = 383\sqrt{2} = 542 \text{ K}$$

The surface mean square displacement at room temperature according to eq. (4.4):

$$\langle u^2\rangle_{surf} = 3.08 \times 10^{-18} \text{ cm}^2 \quad \text{or} \quad \langle u^2\rangle^{1/2}_{surf} = 0.176 \text{ Å}$$

and that of bulk is therefore

$$\langle u^2\rangle_{bulk} = 1.54 \times 10^{-18} \text{ cm}^2 \quad \text{or} \quad \langle u^2\rangle^{1/2}_{bulk} = 0.124 \text{ Å}$$

In summary, first, good linearity is preserved in temperatures extending down to at least 1/2 below θ_D when plotting lnI vs. T. That means the high temperature limit ($T>>\theta_D$) requirement can be relaxed when using the linearity of Debye-Waller factor to obtain θ_D. Second, the results from our measurements conducted under a less strict condition (using fixed energies and continuous heating) appears reasonable. It promises an easy and fast way of measuring the surface Debye temperatures, comparing with those strict, time-consuming methods [78]. Third, the average surface and bulk Debye temperature of NiO, by averaging over that of NiO(111) and NiO(100), are 383 K and 542 K from this study. The reported θ_D for NiO of above 800 K seems doubtful.

CHAPTER 5: PRESSURE EFFECT ON THE GROWTH OF OXIDE EPITAXIES

Results

The effects of oxygen pressure on Ni(100) oxidation can be discussed in two respects. One is the effect on the epitaxial orientation of the growing NiO on Ni(100). The other is the effect on the growth rate and thickness of the oxide. Other authers have expressed the belief that the orientation of NiO which grows on Ni(100) depends on the oxygen pressure [9]. In order to test this hypothesis, we repeat some of the experiments of Figs. 5 and 7 over a range of oxygen pressures. Fig. 48 shows representative results. Curves I, II and III correspond to results from three independent measurement at pressure $7x10^{-9}$, $6x10^{-8}$ and $5x10^{-7}$ torr. In each measurement, the (0,1), (1/2,1/2), (0,1/2) and "ring" spots are monitored simultaneously. It can be seen that the intensities of the diffraction features do, indeed, vary with oxygen pressure, higher pressures leading to fainter patterns. However, the nature of the patterns formed, and the exposures at which they intensify or diminish, are independent of the oxygen pressure. These and other data indicate that oxygen pressure has no bearing on the orientation of NiO which grows during oxidation, nor the exposure at which the oxide forms, at least within the pressure range 10^{-9} to 10^{-7} torr. Rather, sample temperature is the sole determining factor within this pressure range. This is true for the formation of NiO(111) at 300 K or below, and also true for the

Figure 48. Integrated spot intensity vs. exposure are measured at three different oxygen pressures. Curve I, II and III correspond to 7×10^{-9} torr, 6×10^{-8} torr and 5×10^{-7} torr.

(A) Obtained by monitoring the intensity change as exposure on (0,1) spot.

(B) Obtained by monitoring the intensity change as exposure on (1/2,1/2) spot.

(C) Obtained by monitoring the intensity change as exposure on (0,1/2) spot.

(D) Obtained by monitoring the intensity change as exposure on the "ring" spot.

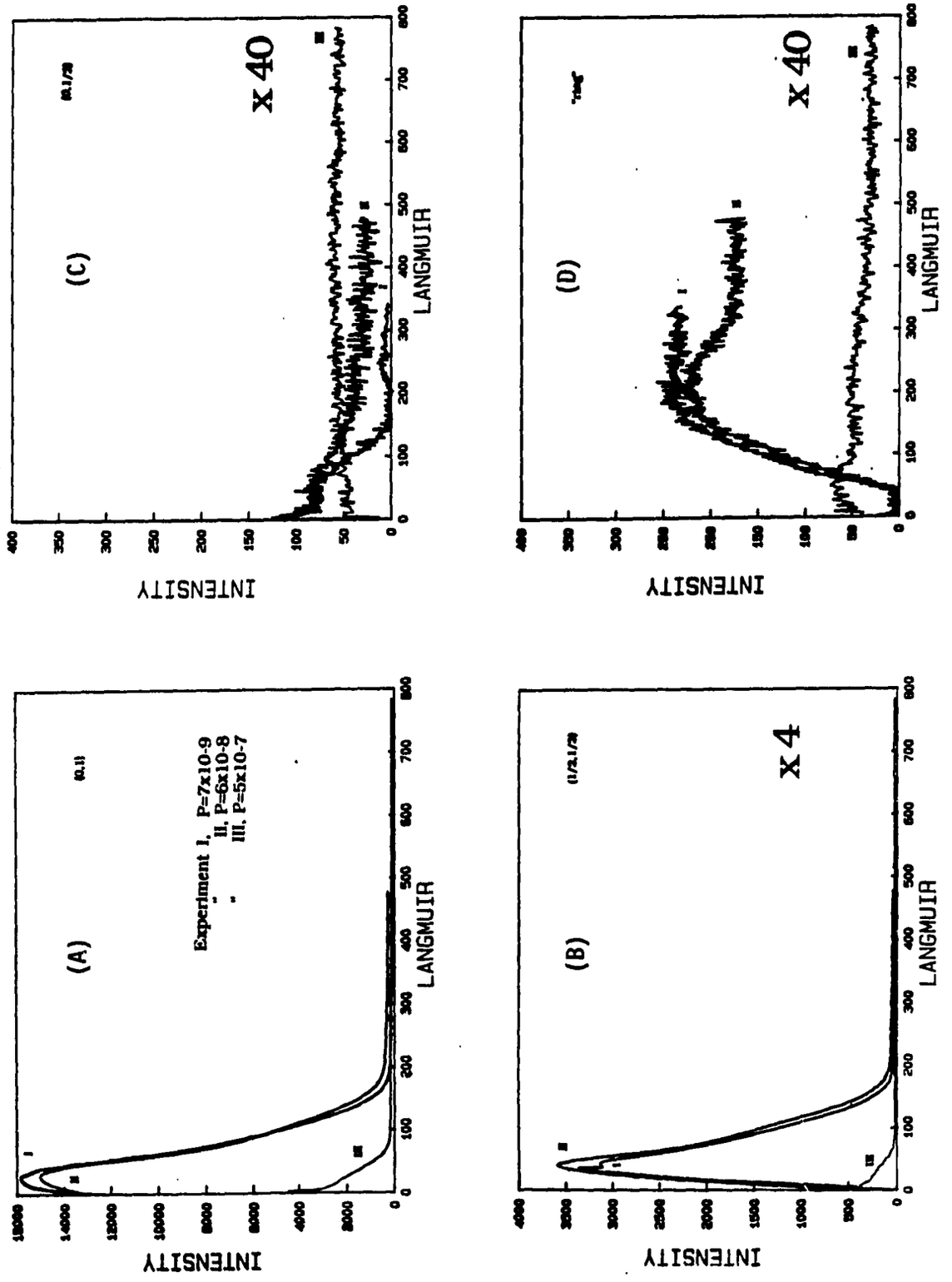
(A)
Experiment I, P=7x10-9
II. P=6x10-8
III. P=5x10-7
(B)
x 4
(C)
x 40
(D)
x 40
INTENSITY
LANGMUIR

formation of (7x7) structure at above 300 K.

Discussion

The pressure effect on spot intensity is a kinetic effect. As pressure increases from 10^{-9} to 10^{-8} torr, the intensity is not reduced much. But as pressure goes to 10^{-7} torr, intensity drops sharply and the (0,1) spot intensity shows monotonical decrease rather than an initial increase then start to decrease after reaching a maxima as these shown in curves I and II of Fig. 48A. These two types of intensity changes with different oxygen pressure indicate that the former corresponds to the situation where the gas particle impinging rate is so high that there is no time for the adsorbate to form ordered overlayer and result in the initial intensity increase of (0,1). Oxidation starts once the coverage (exposure) reaches what is needed for oxide formation. On the other hand, the latter corresponds to the situation where adsorbate forms ordered overlayer, p(2x2) or c(2x2), so that the intensity of (0,1) spot is a superposition of substrate integral spot and higher order p(2x2) or c(2x2) spot intensities during initial chemisorption stage. In this sense, the oxygen pressure does have effect on the oxide growth. But whichever oxide epitaxy that grows on Ni(100) at a given adsorption temperature is independent of the oxygen pressure. Adsorption temperature is the sole factor in determining the orientation of oxide epitaxies that grows on Ni(100) during oxidation.

SUMMARY OF THE OXIDATION MECHANISM OF Ni(100)

We believe that significant contributions have been made to the understanding of nickel oxidation mechanism. Three oxide structures, NiO(111), (7x7) and NiO(100) can grow on Ni(100) during oxidation, depending on the adsorption temperature. NiO(111) is the low temperature epitaxy, NiO(100) is the high temperature epitaxy and (7x7) structure forms at intermediate temperature.

It probably can be speculated that the energy barrier associated with the formation of NiO(111) is low. Others have expressed that those metal oxidation processes occurring below room temperatures must be associated with essentially zero energy barriers [58]. NiO(111) forms at the lowest adsorption temperature among the three oxide structures. It can be explained by the fact that Ni layers in NiO(111) are still parallel to the Ni(100) surface so that the formation of NiO(111) need only to insert oxygen between Ni layers without intra-layer bond breaking, as shown in Figs. 15 and 16. The energy needed for the rearrangement of Ni atoms within the Ni layer (as shown in Fig. 15) is perhaps compensated by the energy released from chemisorption. The heat of chemisorption is approximately equal to the heat of formation of the most stable oxide [77,78], which is 107 K cal/mole for NiO [79]. The (7x7) is similar in its orientation to NiO(100), but has 1.5% lattice contraction and regulated anti-phase walls within the (7x7) unit mesh. NiO(100) is the most stable face due to its structure of coplannar positive and negative ions. But the energy barriers associated with the

formation of both structures are perhaps high. Therefore the (7x7) as an intermediate state forms under the slightly mild condition, i.e., its formation associates with a slightly lower energy barrier than that of NiO(100). This can be depicted in the energy diagram below.

In Fig. 49, start with the chemisorbed Ni(100) at point A, to the right, by passing an energy barrier E_a and forming a perhaps highly unstable state B, the final state NiO(100) can be formed. However, state B is such an energetically unfavorable structure that E_a is much higher than E_b, which corresponds to the formation of the (7x7) structure. Because of the partial registry of oxide overlayer with the substrate Ni(100) in this structure, the total energy of the structure is lowered. It becomes an intermediate state on the way to the most stable face NiO(100). The study on O/Ni(110) seems also to indicate that although NiO(100) is the most stable face of NiO, but the formation of this structure has to be via other intermediate structure, called Ni-(9x4)O or pseudo nickel oxide [47], which is the NiO(100) contracted by ~5% in both directions to conform to the substrate lattice. This partial registry of oxide overlayer to Ni(110) has been observed by STM recently [57].

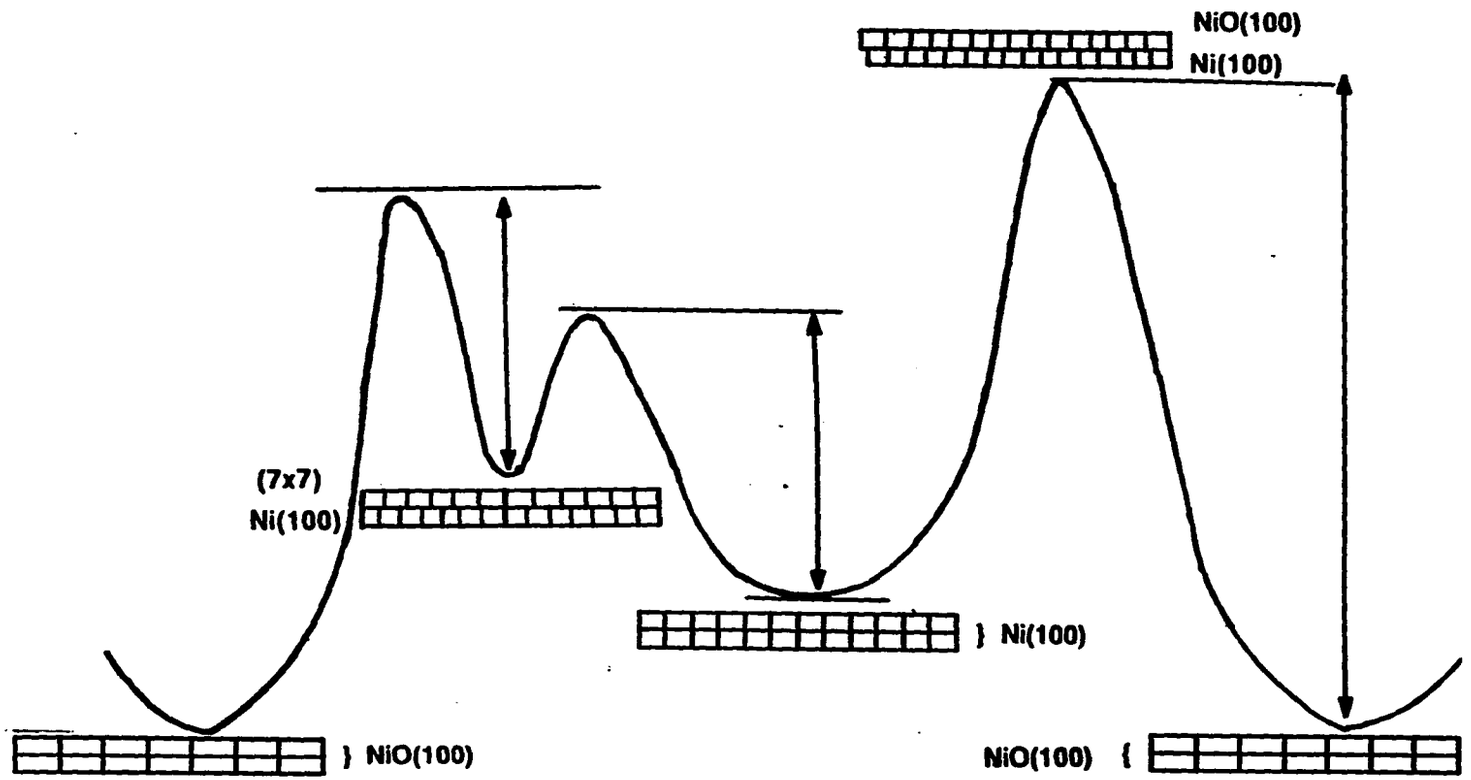

Figure 49. Depiction of energy diagram of the formation of NiO(100) and the (7x7) structures.

APPENDIX 1: DERIVATION OF THE SCATTERING FACTOR OF THE DISTORTED OVERLAYER UNIT CELL

Overlayer displacement modulation model:

The scattering factor, including the diffraction from the (7x7) unit of the distorted overlayer, is:

$$F(hk) = \sum_{j=1} f_j \exp -2\pi i(hx_j + ky_j + \frac{1+\cos\theta}{\lambda} z_j)$$

where θ = angle in^out; h and k are fractional-order Miller indices; x_j and y_j = coordinate relative to substrate, where x_j, y_j runs in steps of 7/6 from 7/6 to 6; or $x_j = 7/6\ \zeta$ where $\zeta = 1 \ldots 6$, $y_j = 7/6\ \gamma$, where $\gamma = 1 \ldots 6$. The atomic displacement in z-direction varies in a periodic way.

$$z_j = \alpha \cdot \cos\ (2\pi/7\ x_j)$$

where α = amplitude of displacement relative to a planar substrate configuration. Therefore

$$F = f \sum_{j=1}^{6} \sum_{i=1}^{6} \exp -i2\pi[\frac{7}{6}\xi_j h + \frac{7}{6}\gamma_i k + \frac{1+\cos\theta}{\gamma}\alpha \cdot \cos(\frac{2\pi}{6} z i_j)]$$

$$= [i + \exp(-i2\pi\frac{7}{6}k) + \exp(-i2\pi\frac{14}{6}k) + \ldots + \exp(-i2\pi\frac{35}{6}k)]$$

$$\sum_{j=1}^{6} \exp -i2\pi[\frac{7}{6}\xi_j h + \frac{1+\cos\theta}{\gamma}\ \alpha \cdot \cos(\frac{2\pi}{6}\ \xi_j)]$$

For $\alpha = 0$

F will be zero unless:

$$\frac{7}{6}\,h = m, \text{integer}$$

primary fractional diffraction spots are:

$$\frac{7}{6}k = n, \text{ integer}$$

then $F = 36\ f_0 = F_0$

For $\alpha \neq 0$

We have:

$$F = f \sum_{j=1}^{6} \exp -i2\pi\left[\frac{7}{6}\xi_j\, h + 0 + \frac{1+\cos\theta}{\gamma}\,\alpha\cdot\cos\left(\frac{2\pi}{6}\xi_j\right)\right]$$

$$+ \sum_{j=1}^{6} \exp\ -i2\pi\ \left[\frac{7}{6}\xi_j h + \frac{7}{6}k + \frac{1+\cos\theta}{\lambda}\,\alpha\cdot\cos\left(\frac{2\pi}{6}\xi_j\right)\right]$$

$$+ \sum_{j=1}^{6} \exp -i2\pi\left[\frac{7}{6}\,\xi_j h + \frac{14}{6}k + \frac{1+\cos\theta}{\lambda}\cdot\alpha\cdot\cos\left(\frac{2\pi}{6}\,\xi_j\right)\right]$$

$$\sum_{j=1}^{6} \exp -i2\pi\left[\frac{7}{6}\,\xi_j h + \frac{21}{6}k + \frac{1+\cos\theta}{\lambda}\cdot\alpha\cdot\cos\left(\frac{2\pi}{6}\,\xi_j\right)\right]$$

$$+ \sum_{j=1}^{6} \exp -i2\pi\left[\frac{7}{6}\,\xi_j h + \frac{28}{6}k + \frac{1+\cos\theta}{\lambda}\cdot\alpha\cdot\cos\left(\frac{2\pi}{6}\,\xi_j\right)\right]$$

$$+ \sum_{j=1}^{6} \exp -i2\pi\left[\frac{7}{6}\,\xi_j h + \frac{35}{6}k + \frac{1+\cos\theta}{\lambda}\cdot\alpha\cdot\cos\left(\frac{2\pi}{6}\,\xi_j\right)\right]$$

$$= f\left[1 + \exp\left(-i2\pi\frac{7}{6}m\right) + \exp\left(-i2\pi\frac{14}{6}m\right) + \exp\left(-i2\pi\frac{21}{6}m\right) + \exp\left(-i2\pi\frac{28}{6}m\right)\right.$$

$$+ \exp(-i2\pi\frac{35}{6}m)]\sum \exp -i2\pi[\frac{7}{6}\xi_j h + \frac{1+\cos\theta}{\lambda}\cdot\alpha\cdot\cos(\frac{2\pi}{6}\xi_j)]$$

$$\text{let } \frac{\beta}{2\pi} = \frac{1+\cos\theta}{\lambda}\alpha$$

expand:

$$\exp[-i\beta\cos\frac{2\pi}{6}\xi_j] = 1 - i\beta\cos(\frac{2\pi}{6}\xi_j) + \frac{1}{2}\beta^2\cos^2\frac{2\pi}{6}\xi_j + \ldots.$$

take the first-order term above, then:

$$\sum_{j=1}^{6}\exp[-i\frac{2\pi}{6}7\xi_j h](-i\beta\cos\frac{2\pi}{6}\xi_j)$$

$$= \sum_{j-1}^{6}\exp[-i\frac{2\pi}{6}7\xi_j h](-i\beta)\frac{\exp[\frac{-i2\pi}{6}\xi_j] + \exp[\frac{i2\pi}{6}\xi_j]}{2}$$

$$= -i\beta\sum_{j=1}^{6}\underbrace{\exp[-i2\pi\frac{\xi_j}{6}(7h+1)]}_{F_1^+} + \underbrace{\exp[-i2\pi\frac{\xi_j}{6}(7h-1)]}_{F_1^-}$$

let $F_1 = F_1^+ + F_1^-$

F_1 will be zero unless $\frac{\xi_j}{6}(7h \pm 1) = n$

or $$h = \frac{6n \mp 1}{7}$$

These are the second-order fractional spots.

Similarly, take the 2nd-order term in the expansion

$$\sum_{j=1}^{6} \exp[-i\,\frac{2\pi}{6}\,7\xi_j h]\;(\frac{1}{2}\,\beta^2)\,\cos^2(\frac{2\pi}{6}\,\xi_j)\;,$$

$$= \frac{\beta^2}{4}\sum_{j=1}^{6} \underbrace{\exp[-i\frac{2\pi}{6}\,7\xi_j h]}_{F_0} + \frac{\beta^2}{4}\sum_{j=1}^{6} \underbrace{\exp[-i\frac{2\pi}{6}\,\xi_j\,(7h+2)]}_{F_2^+} + \underbrace{\exp[-i\frac{2\pi}{6}\,\xi_j\,(7h-2)]}_{F_2^-}$$

$$\text{where } \cos^2\frac{2\pi}{6}\,\xi_j = \frac{1+\cos\frac{4\pi}{6}\,\xi_j}{2}$$

let $F_2 = F_2^+ + F_2^-$

F_2 will be zero unless

$$\frac{\xi_j}{6}\,(7h \pm 2) = n \text{ or } h = \frac{6n \mp 2}{7}$$

The scattering factor of the (7x7) unit cell is

$$F = 2F_0 + F_1 + F_2$$

locations of the primary, first-order, second-order spots are:

$$\text{primary:}\quad h = \frac{6}{7}m\;,\quad k = \frac{6}{7}n \quad m,n \text{ are integers.}$$

$$\text{1st-order}\quad h = \frac{6m\pm1}{7}\;,\quad k = \frac{6n\pm1}{7}$$

$$\text{2nd-order}\quad h = \frac{6m\pm2}{7}\;,\quad k = \frac{6n\pm2}{7}$$

Estimation of the intensity of fractional spots:

$$\text{since } \beta = \alpha \cdot \frac{(1+\cos\theta)}{\lambda} \cdot 2\pi$$

where α typically ~ 0.1 Å

$\cos\theta$ varies from 0 to 1

$$\therefore \text{ For } \lambda = \sqrt{\frac{150}{46ev}} = 1.81 \text{ Å}$$

(46 eV is the incident electron energy used for the fractional spots measurement)

$\therefore$ typically $\beta = 0.346 \sim 0.69$

if primary spot intensity α F_0^2

then first-order Intensity α β^2 F_0^2 = 12% 48% F_0^2

second-order Intensity α $\beta^4/16$ F_0^2 = 0.09% - 1.4% F_0^2

APPENDIX 2: DERIVATION OF THE KINEMATIC DIFFRACTION INTENSITY

The diffraction intensity in 2-dimension can be expressed as:

$$I(hk) = \left| \sum_{n_1=0}^{N_1-1} \sum_{n_2=0}^{N_2-1} f \cdot f_m(n_2) \cdot \exp\{2\pi i(n_1 h + n_2 k)\} \right|^2$$

where

$$f_m(n_2) = \frac{4}{\pi} \sum_{m=0}^{\infty} \frac{1}{2m+1} \sin \frac{2m+1}{M} \pi n_2$$

therefore

$$I(hk) = \left| \sum_{n_1=0}^{N_1-1} \exp(2\pi i n_1 h) \right|^2 \left| \sum_{n_2=0}^{N_2-1} f_m(n_2) \exp(2\pi i n_2 k) \right|^2$$

where

$$\sum_{n_1=0}^{N_i-1} \exp(2\pi i n_1 h) \Big|^2 = \left| \frac{1 - \exp(2\pi i N_1 h)}{1 - \exp(2\pi i h)} \right|^2$$

$$= \left| \frac{\exp[+\pi i N_1 h] \left(\exp[-\pi i N_1 h] - \exp[\pi i N_1 h]\right)}{\exp[\pi i h] \left(\exp[-\pi i h] - \exp[\pi i h]\right)} \right|^2$$

$$= \frac{\sin^2 \pi N_1 h}{\sin^2 \pi h}$$

Therefore

$$I(hk) = f^* \cdot f \frac{\sin^2 N_1 \pi h}{\sin^2 \pi h} \left| \sum_{n_2=0}^{N_2-1} f_m(n_2) \exp(2\pi i n_2 k) \right|^2$$

It is the factor

$$F = \sum_{n_2=0}^{N_2-1} f_m(n_2) \exp(2\pi i n_2 k)$$

that gives split of spots in the k-direction.

APPENDIX 3: DERIVATION OF THE KINEMATIC DIFFRACTION FACTOR IN ANTIPHASE WALL MODEL

The factor in Appendix 2 that gives split along k-direction in reciprocal space can be further simplified here:

$$F^* \cdot F = \left| \sum_{n_2=0}^{N_2-1} f_M(n_2) \exp(2\pi i n_2 k) \right|^2$$

$$= \left| \sum_{n_2=0}^{N_2-1} \frac{4}{\pi} \sum_{m=0}^{\infty} \frac{1}{2m+1} \sin\left(\frac{2m+1}{M} \pi n_2\right) \cdot \exp(2\pi i n_2 k) \right|^2$$

$$= \left| \frac{4}{\pi} \sum_{m=0}^{\infty} \frac{1}{2m+1} \sum_{n_2=0}^{N_2-1} \sin\left(\frac{2m+1}{M} \pi n_2\right) \exp(2\pi i n_2 k) \right|^2$$

$$\left| \sum_{m=0}^{\infty} \frac{1}{2m+1} \sum_{n=0}^{N-1} \frac{\exp\left(\frac{2m+1}{M} \pi n\right) i - \exp\frac{-2m+1}{M} \pi n) i}{2i} \exp(2\pi i n k) \right|^2$$

$$= \frac{4}{\pi^2} \left| \sum_{m=0}^{\infty} \frac{1}{2m+1} \sum_{n=0}^{N-1} \exp\left[\left(\frac{2m+1}{M} + 2k\right) \pi n i\right] - \exp\left[\left(2k - \frac{2m+1}{M}\right) \pi n i\right] \right|^2$$

$$= \frac{4}{\pi^2} \left| \sum_{m=0}^{\infty} \frac{1}{2m+1} \left(\frac{1 - \exp\left(\frac{2m+1}{M} + 2k\right) \pi i N}{1 - \exp\left(\frac{2m+1}{M} + 2k\right) \pi i} - \frac{1 - \exp\left(2k - \frac{2m+1}{M}\right) \pi i N}{1 - \exp\left(2k - \frac{2m+1}{M}\right) \pi i} \right) \right|^2$$

$$= \frac{4}{\pi^2} \left| \sum_{m=0}^{\infty} \frac{1}{2m+1} \frac{\exp(\frac{2m+1}{2M}+k)\pi i N \left(\exp[-i(\frac{2m+1}{2M}+k)\pi N] - \exp[i(\frac{2m+1}{2M}+k)\pi N]\right)}{\exp[i(\frac{2m+1}{2M}+k)\pi] \left(\exp[-i(\frac{2m+1}{2M}+k)\pi] - \exp[i\frac{2m+1}{2M}+k)\pi]\right)} \right.$$

$$\left. - \frac{\exp[i(k-\frac{2m+1}{2M})\pi N] \left(\exp[-i(k-\frac{2m+1}{2M})\pi N] - \exp[i(k-\frac{2m+1}{2M})\pi N]\right)}{\exp[i(k-\frac{2m+1}{2M})\pi] \left(\exp[-i(k-\frac{2m+1}{2M})\pi] - \exp[i(k-\frac{2m+1}{2M})\pi]\right)} \right|^2$$

$$= \frac{4}{\pi^2} \left| \sum_{m=0}^{\infty} \frac{1}{2m+1} \left[\exp i\pi(k+\frac{2m+1}{2M}) (N-1) \frac{\sin N\pi(k+\frac{2m+1}{2M})}{\sin \pi(k+\frac{2m+1}{2M})} - \right.\right.$$

$$\left.\left. \exp i\pi(k - \frac{2m+1}{2M})(N-1) \frac{\sin N\pi(k-\frac{2m+1}{2M})}{\sin \pi(k-\frac{2m+1}{2M})} \right]^2 \right.$$

ACKNOWLEDGEMENTS

I would like to thank my research advisor, Dr. Patricia Thiel, for her guidance and support during my graduate career. I appreciate her role in improving my English-speaking and -communication skills and her patience in reading and correcting this thesis.

My appreciation is extended to Dr. N.-J. Wu for working with me on the experiment and to Dr. M. C. Tringides for the numerous discussions on the data analysis of Chapter 2 in this thesis.

My sincere appreciation goes out to the past and present members of the Thiel group, who made the working place enjoyable and memorable. Just to name a few: Mike Columbia, who explains the meaning of a word better than any English teacher I have ever had, Dr. Diane Sanders and Barb Nielsen, who are always willing to help with things inside and outside the lab, and Oden Warren, whose interest in the oriental culture made homesickness less painful.

I appreciate the friendship of Ms. Debra Peterson and family, Ms. Margaret Stanley and Prof. Dennis Wendell, who made life, especially holidays in Ames, enjoyable.

Finally, I would like to thank my parents for their support and encouragement through my school years. I am deeply indebted to my husband Xiaolin Wu for his patience and understanding through the years. His insight of physics and knowledge on computer helped me greatly through the countless inspirational discussions we had over the years. I also thank my daughter Victoria Dee who brought so much joy and energy

drives me to work tirelessly. Without these this thesis would not be possible.

I also thank the chemistry department and Ames lab. for making the facilities available. This work was performed at Ames laboratory under contract no. W-7405-eng-82 with the U. S. Department of Energy. The United States governments has assigned the DOE Report number IS-T-1519 to this thesis.

REFERENCES

1. N. Cabrera and N. F. Mott, Rept. Progr. Phys. 12 (1949) 163.
2. K. Miyahara, J. Res. Inst. Catalysis (Hokkaido Univ.) 11 (1963) 1.
3. P. Pareja, A. Amariglio and H. Amariglio, J. Catalysis 36 (1975) 379.
4. G. A. Martin, N. Ceathalan, Ph. De Montgolfier and B. Imelik, J. Chim. Phys. 70 (1973) 1422.
5. G. A. Martin and Ph. De Montgolfier, J. Chim. Phys. 72 (1975) 405.
6. S. J. Teichner, in Catalysis; Progress in Research, Eds. F. Basolo and R. Burwell (Plenum, New York, 1973).
   A. P. Hagan, M. G. Lofthouse, F. S. Stone and M. A. Trevethan, Studies Surface Science Catalysis 3 (1979) 417.
7. C. Davisson and L. H. Germer, Phys. Rev. 30 (1927) 705.
8. A. U. MacRae, Surface Sci. 1 (1964) 319.
9. C. R. Brundle and J. Q. Broughton, "The Initial Interaction of Oxygen with Well-Defined Transition Metal Surfaces," in The Chemical Physics of Solid Surfaces and Heterogeneous Catalysis, Vol. 3, Eds. D. A. King and D. P. Woodruff (Elsevier, Amsterdam, to be published)
10. J. W. M. Frenken, J. F. van der Veen and G. Allan, Phys. Rev. Letters 51 (1983) 1876.
11. J. W. M. Frenken, R. G. Smeenk and J. F. van der Veen, Surface Sci. 135 (1983) 147.
12. P. F. A. Alkemade, S. Deckers, F. H. P. M. Habraken and W. F. Van

Der Weg, Surface Sci. 189/190 (1987) 161.

13. U. Starke, P. L. deAndres, D. K. Saldin, K. Heinz and J. B. Pendry, Phys. Rev. B 38 (1988) 12277.
14. S. Y. Tong and K. H. Lau, Phys. Rev. B 25 (1982) 7382.
15. J. Stöhr, R. Jaeger and T. Kendelewicz, Phys. Rev. Letters 49 (1982) 142.
16. G. Hanke, E. Lang, K. Heinz and K. Müller, Surface Sci. 91 (1980) 551.
17. H. H. Brongersma and J. B. Theeten, Surface Sci. 54 (1976) 519.
18. J. E. Demuth, N. J. DiNardo and G. S. Cargill III, Phys. Rev. Letters 50 (1983) 1373.
19. S. R. Chubb, P. M. Marcus, K. Heinz and K. Mueller, IBM Res. Report (1990).
20. D. E. Taylor and R. L. Park, Surface Sci. 125 (1983) L73.
21. C. R. Brundle, J. Vac. Sci. Technol. A3 (1985) 1468.
22. C. R. Brundle, R. J. Behm and J. A. Barker, J. Vac. Sci. Technol. A2 (1984) 1038.
23. P. H. Holloway and J. B. Hudson, Surface Sci. 43 (1974) 123.
24. D. F. Mitchell, P. B. Sewell and M. Cohen, Surface Sci. 61 (1976) 355.
25. R. G. Smeenk, R. M. Tromp, J. W. M. Frenken and F. W. Saris, Surface Sci. 112 (1981) 261.
26. P. R. Norton, R. L. Tapping and J. W. Goodale, Surface Sci. 65 (1977) 13.
27. T. M. Christensen, C. Raoul and J. M. Blakely, Appl. Surf.

Sci. 26 (1986) 408.

28. S. Evans, J. Pielaszek and J. M. Thomas, Surf. Sci. 56 (1976) 644.
29. H. Hopster and C. R. Brundle, LeVide 201 (1981) 285.
30. N. Wagner, O. Brummer and V. V. Khodasevich, Phys Status Solidi A 62 (1980) 275.
31. H. E. Farnsworth, Applied Phys. Lett. 2 (1963) 199.
32. F. T. Wagner and T. E. Moylan, J. Electrochem. Soc. 136 (1989) 2498.
33. R. S. Saiki, A. P. Kaduwela, J. Osterwalder, C. S. Fadley and C. R. Brundle, Phys. Rev. B 40 (1989) 1586.
34. G. Dalmai-Imelik, J. C. Bertolini and J. Rousseau, Surface Sci 63 (1977) 67.
35. R. Kaplan and G. A. Somorjai, Solid State Commun. 9 (1971) 505.
36. S.-L. Chang and P. A. Thiel, J. Chem. Phys. 88 (1988) 2071; also J. Vac. Sci. Technol. A6 (1988) 837.
37. S.-L. Chang, P. A. Thiel and J. W. Evans, Surface Sci. 205 (1988) 117.
38. S.-L. Chang, Ph.D thesis, Iowa State University, unpublished, 1988.
39. D. K. Sanders, Ph.D thesis, Iowa State University, unpublished, 1990.
40. P. A. Thiel and J. W. Anderegg, Rev. Sci. Instrum. 55 (1984) 1669. J. W. Anderegg and P. A. Thiel, J. Vac. Sci. Technol. A4 (1986) 1367.
41. H. Herz, H. Conrad and J. Kuppers, J. Phys. E 12 (1979) 369.
42. T. S. Rahman, D. L. Mills, J. E. Black, J. M. Szeftel, S. Lehwald and H. Ibach, Phys. Rev. B 30 (1984) 589.

43. R. A. Robie, P. M. Bethke and K. M. Beardsley, "Selected X-ray Crystallographic Data, Molar Volumes, and Densities of Minerals and Related Substrates," Geological Survey Bulletin 1248 (U.S. Government Printing Office, Washington, 1967).

44. P. W. Tasker, J. Phys. C 12 (1979) 4977.

45. I. Stranski, Z. Phys. Chem. 136 (1928) 259.

46. P. Holloway, Univ. of Florida, Private Comm. Köln, 1989.

47. J. W. May and L. H. Germer, Surface Sci. 11 (1968) 443.

48. P. W. Palmberg and T. N. Rhodin, J. Chem. Phys. 19 (1968) 147.

49. C. W. Tucker, Jr., Appl. Phys. Letters 3 (1963) 98.
C. W. Tucker, Jr., J. Appl. Phys. 35 (1964) 1897.
C. W. Tucker, Jr., Surface Sci. 2 (1964) 516.

50. N. Taylor, Surface Sci. 4 (1966) 161.

51. E. Bauer, Surface Sci. 7 (1967)351.

52. F. Jona, F. Lever and J. B. Gunn, Surface Sci. 9 (1968) 463.

53. G. Ertl and J. Küpper, Low Energy Electrons and Surface Chemistry (Weinheim, FRG, 1985).

54. P. W. Palmberg and W. T. Peria, Surface Sci. 6 (1967) 57.

55. Kunio Fujiwara, J. Phys. Soc. of Japan. 12 (1957) 7.

56. E. Kopatzki and R. J. Behm, Submitted to Surface Sci. August 1990.

57. E. Ritter and R. J. Behm, in the Springer Series in the Surface Science 11: "The Structure of Surfaces II" eds. J. F. Van der Veen and M. A. Van Hove (Springer-Verlag, Berlin, 1988.

58. F. P. Fehlner and N. F. Mott, Oxidation of Metals 2 (1970) 59.

59. H. H. Madden, J. Vac. Sci. Technol. 18 (1981) 677.

60. S. Mukherjee, V. Kumar and K. H. Bennemann, Surface Sci. 167 (1986) L210.

61. W. Altmann, K. Desinger, M. Donath, V. Dose, A. Goldmann and H. Scheidt, Surface Sci. 151 (1985) L185.

62. J. E. Demuth, D. W. Jepsen and P. M. Marcus, Phys. Rev. Lett. 31 (1973) 54.

P. M. Marcus, J. E. Demuth and D. W. Jepsen, Surface Sci. 53 (1975) 501.

M. Van Hove and S. Y. Tong, J. Vac. Sci. Technol. 12 (1975) 230.

63. M. DeCrescenzi, F. Antonangeli, C. Bellini and R. Rosei, Phys. Rev. Lett. 50 (1983) 1949.

64. S. Andersson, Solid State Commun. 20 (1976) 229.

65. S. Lehwald, J. Szeftel, H. Ibach, T. S. Rahman, D. L. Mills and J. E. Black, Phys. Rev. Lett. 51 (1983) 268.

66. T. S. Rahman, J. E. Black and D. L. Mills, Phys. Rev. Lett. 46 (1981) 1469.

67. T. H. Upton and W. A. Goddard, III, ISISS 1979, Surface Science: Recent Progress and Perspectives (CRC Press, Boca Raton, Florida, 1980).

68. S. Mroz and A. Mroz, Surface Science 109 (1981) 444.

69. M. A. Van Hove and S. Y. Tong, Springer Series in Chemical Physics 2 Surface Crystallography by LEED (Springer-Verlag, New York, 1979).

70. C. Kittel, Introduction to Solid State Physics, Sixth Ed. (John Wiley & Sons, Inc., New York, 1986).

71. R. F. Wallis, B. C. Clark, R. Herman and D. C. Gazis, Phys. Rev. 180 (1969) 716.

72. R. E. Allen and F. W. De Wette, Phys. Rev. 188 (1969) 1320.

73. R. L. Dennis, M. B. Webb, J. Vac. Sci. Technol. 10 (1973) 192.

74. D. Tabor, J. M. Wilson and T. J. Bastow, Surface Science 26 (1971) 471.

75. A. U. MacRae, Surface Science 2 (1964) 522.

76. E. R. Jones, J. T. Mckinney and M. B. Webb, Phys. Rev. 151 (1966) 476.

77. R. F. Wallis, B. C. Clark and R. Herman, in: The Structure and Chemistry of Solid Surfaces Ed. G. A. Somorjai(Wiley, New York, 1969) p. 17-1.

78. D. Brennan, D. O. Hayward and B. M. W. Trapnell, proc. Roy. Soc. (London) Ser. A 256 (1960) 81.

79. Ken-Ichi Tanaka and K. Tamaru, J. Catalysis 2 (1963) 366.